Alma Mater Studiorum · University Bologna Cesena Campus

DEPARTMENT OF ELECTRICAL ENERGY AND INFORMATION
ENGINEERING
-GUGLIELMO MARCONI-

MASTER'S DEGREE PROGRAM IN
ELECTRONICS AND TELECOMMUNICATIONS ENGINEERING FOR
ENERGY

Modelling and Simulation of a Nonlinear IPMSM in MATLAB/Simulink

THESIS IN ELECTRONICS

SUPERVISOR:
Prof. Alberto Bellini
Co-supervisors:
Prof. Claudio Bianchini
Giada Sala

SUBMITTED BY: Andrea Ambrosini

ACADEMIC YEAR 2024/2025

Index

1	Abstract							
2	Introduction							
	2.1	Electr	ic Motors	9				
	2.2		lations of Electromechanical Energy Conversion	10				
		2.2.1	Electric and Magnetic Field	10				
		2.2.2	Lorentz Force	11				
		2.2.3	Ampere's Law	12				
		2.2.4	Faraday-Neumann-Lenz's Law	13				
		2.2.5	Magnetic Circuits	14				
		2.2.6	Torque, Moment of Inertia, and Mechanical Power	15				
	2.3	Struct	ture of an AC motor	15				
		2.3.1	Stator	16				
		2.3.2	Rotor	17				
		2.3.3	Windings	17				
		2.3.4	Enclosure	19				
	2.4	Main	Components of an Electric Powertrain	20				
		2.4.1	Selection of AC motor	21				
		2.4.2	Biggest Concerns about Battery Pack	23				
		2.4.3	Type of DC/DC and DC/AC converters	24				
3	Per	manen	nt Magnet Synchronous Motors	27				
	3.1		sure and working principle	27				
	3.2		r Control	28				
		3.2.1	Field Oriented Control	29				
	3.3	Torqu	e and voltage equations	31				
		3.3.1	Simplified case	31				
		3.3.2	Anisotropic case	34				
	3.4	Contr	ol Strategies	34				
		3.4.1	Maximum Torque per Ampere	35				
		3.4.2	Field Weakening	35				
		3.4.3	Maximum Torque per Voltage	36				
	3.5	Opera	ating Limits	36				

		3.5.1	Operating Limits for Isotropic Rotors							
		3.5.2	Operating Limits for Anisotropic Rotors	38						
	3.6	Non Io	deal Phenomena	42						
		3.6.1	Core magnetic saturation	42						
		3.6.2	Core Losses	44						
4	Field Oriented Control System									
	4.1	System	n Block Diagram	47						
	4.2	Contro	oller Fundamentals	47						
		4.2.1	Motor Plant Transfer Function	48						
		4.2.2	PI Controller Transfer F unction	48						
		4.2.3	Open Loop System Analysis	49						
5	Fini	ite Ele	ment Analysis and Frozen Permeability	5 3						
	5.1	Finite	Element Analysis	53						
	5.2	Frozen	Permeability Method	53						
		5.2.1	Inductance Computation	54						
		5.2.2	Permanent Magnet Magnetic Flux	55						
6	Simulink Non Linear Motor Model 5									
	6.1	Custo	m Motor Model	58						
		6.1.1	Custom IPMSM Model	59						
		6.1.2	Tri-phase Subsystem	61						
		6.1.3	Current Measurement	63						
		6.1.4	Inductance Computation	64						
		6.1.5	BEMF and Flux Computation	66						
		6.1.6	Iron Losses Computation	67						
		6.1.7	Torque Generation	68						
	6.2	Curre	nt Control Loop	68						
		6.2.1	PI Controllers	69						
		6.2.2	BEMF Feed-Forward Compensation	71						
	6.3	Speed	Control Loop	72						
		6.3.1	PID Controller	73						
		6.3.2		73						
	6.4	Vehicl	e Dynamics	74						
		6.4.1	Gearbox Modelling	74						
		6.4.2	Vehicle Body Dynamics	75						
		6.4.3	Braking System	76						
7	Exp	erime	ntal Results and Comparative Analysis	7 9						
	7.1		imental Setup	79						
		7.1.1	Gearbox Artifact	79						
	7.2	Comp	arative Analysis with Constant Parameters Model	80						
		7.2.1	Voltage and Current Evaluation	80						

		7.2.2	Torque and Speed Performance Evaluation	84					
		7.2.3	Power Efficiency Performance Evaluation	84					
	7.3	Compa	arative Analysis with Variable Parameters Model	85					
		7.3.1	Voltage and Current Evaluation	87					
		7.3.2	Torque and Speed Performance Evaluation	87					
		7.3.3	Power and Efficiency Performance Evaluation	91					
8	Conclusions and Future Work								
	8.1	Summ	ary of Contributions	95					
		8.1.1	Low-Power Applications	95					
		8.1.2	High-Performance Applications	95					
	8.2	Model	Advantages and Implementation	96					
	8.3	Future	Research Directions	96					
9	Acknowledgments								
$\mathbf{B}^{\mathbf{i}}$	Bibliography								

To my grandmother Loredana, whose kindness has always been an example to me.

Chapter 1

Abstract

Questa tesi presenta lo sviluppo e la validazione di un modello Simulink per la simulazione di un motore sincrono a magneti permanenti interni (IPMSM), progettato per rappresentare in modo accurato il comportamento del sistema anche in presenza delle non linearità che si manifestano durante il normale funzionamento.

Il modello considera le principali caratteristiche elettromagnetiche del motore, includendo gli effetti di saturazione e di interazione tra le correnti di asse diretto e in quadratura. A tal fine è stato implementato un controllo ad orientamento di campo (FOC, Field Oriented Control), che consente una regolazione efficace della coppia e del flusso e permette di analizzare la risposta dinamica del sistema in differenti condizioni operative.

Per tenere conto della variazione dei parametri elettrici al variare delle correnti di statore, sono state utilizzate multiple lookup tables che descrivono l'andamento delle induttanze L_d e L_q e del flusso magnetico generato dai magneti permanenti λ_{PM} in funzione delle correnti I_d e I_q .

La validazione, condotta tramite un confronto con i modelli standard PMSM di Simulink, ha dimostrato un'eccellente accuratezza nella stima della coppia elettromagnetica e del comportamento elettromeccanico globale. Inoltre, l'integrazione di lookup tables per le perdite aggiuntive ha consentito di ottenere risultati più realistici, senza compromettere l'efficienza computazionale.

Il modello proposto rappresenta un valido strumento per lo studio, la simulazione e l'ottimizzazione di azionamenti a motore sincrono a magneti permanenti interni, con un compromesso tra accuratezza e complessità computazionale.

Chapter 2

Introduction

The growing challenge of climate change has intensified interest in electric vehicles as a sustainable alternative to conventional internal combustion engine vehicles. Offering high efficiency and energy density, and zero tailpipe emissions, electric motors present a promising solution for reducing environmental impact [1].

In the following section, we will examine the fundamental aspects of electric motors, including their working principles, classification methods, and key components.

2.1 Electric Motors

Electric motors are generally divided into two main categories: DC and AC motors.

AC motors can be classified in:

- **Induction motors**: the rotor current is induced by the stator magnetic field.
- Synchronous motors: the rotor rotates at the same speed as the stator magnetic field.

DC motors can be classified in:

- Brushed motors: they use brushes to reverse the current direction.
- Brushless motors: they use an electronic commutator for current reversal.
- Series, shunt and compound motors: they are classified depending on how the field winding is connected to the armature.

This work will focus on AC motors in particular on synchronous motors.

To understand the operation of electric motors, it is necessary to first establish the electromagnetic forces involved.

2.2 Foundations of Electromechanical Energy Conversion

In the following section, some principles of electromechanical energy conversion are briefly discussed to provide a solid foundation for the subsequent analyses.

Through the Coulomb Force and Lorentz Force it is possible to define respectively the electric field and the magnetic density flux.

2.2.1 Electric and Magnetic Field

Electric Field

Formulated in 1785 by Charles-Augustin de Coulomb, the Coulomb force states that considering 2 charges q_1 and q_2 separated by a distance r, the force acting on them is given by:

$$|\vec{F}| = k_e \frac{q_1 \ q_2}{r^2} \tag{2.1}$$

where $k_e = \frac{1}{4\pi\mathcal{E}_0}$ with \mathcal{E}_0 the permittivity of free space. The electric field is then defined as the force acting on a test charge q_0 :

$$\vec{E} = \frac{\vec{F}}{q_0} \tag{2.2}$$

By considering the section Σ of a conductor and ΔQ the number of charges that pass through it in a time interval Δt , it is possible to define the electric current as:

$$i = \lim_{\Delta t \to 0} \frac{\Delta Q}{\Delta t} = \frac{dQ}{dt} \tag{2.3}$$

Even tough current is carried by the movement of electrons, the orientation of the current density vector correspond to the one of the electric field, so it is defined as:

$$\vec{J} = \rho \ \vec{v}_d \tag{2.4}$$

Magnetic Field

Every electric motor requires a rotating magnetic field to operate effectively. This rotating field can be generated through various techniques, such as a three-phase AC supply in induction motors or the use of permanent magnets in synchronous motors. The presence of a well-defined magnetic field is crucial for the interaction between the motor's current-carrying conductors and the magnetic flux, which produces the torque necessary for rotation.

The magnetic field can be quantitatively described using the concept of the Lorentz force. A charged particle moving in a magnetic field experiences a force perpendicular both to the velocity of the particle and the direction of the magnetic field. Mathematically, the magnetic flux density \vec{B} can be expressed as [2]:

$$\vec{B} = \frac{\vec{F}}{q \, v \, \sin(\theta)} \tag{2.5}$$

where \vec{F} is the force acting on a particle with charge q, moving with velocity v, and θ is the angle between the velocity vector and the magnetic field.

It is important to note that \vec{B} represents the magnetic flux density, rather than the magnetic field strength. These two quantities are related through the material's magnetic permeability μ , as:

$$\vec{B} = \mu \, \vec{H} = \mu_0 (1 + \chi_m) \, \vec{H} \tag{2.6}$$

where \vec{H} is the magnetic field strength, μ_0 is the magnetic permeability of free space, and χ_m is the magnetic susceptibility of the material. The permeability μ characterizes the material's response to the applied magnetic field, determining how effectively it can support the formation of magnetic flux.

Just as electric current represents the flow of charge in a conductor, magnetic flux represents the flow of magnetic field lines through a surface. For an ideal core, it can be expressed as

$$\Phi = \oint \vec{B} \cdot d\vec{A} \tag{2.7}$$

Since a magnetic flux often passes through N turns in a coil wrapped around an iron core, it is convenient to define the total flux passing through the coil, called flux linkage, simply as:

$$\lambda = N \Phi \tag{2.8}$$

2.2.2 Lorentz Force

Almost all electric motors rely the Lorentz force to generate rotation.

Formulated by Hendrik Lorentz in 1895, the Lorentz force states that a particle with charge q, moving with velocity \vec{v} in an electric field \vec{E} and a magnetic flux density \vec{B} , experiences a force given by:

$$\vec{F} = q(\vec{E} + \vec{v} \times \vec{B}) \tag{2.9}$$

Considering no electric field applied, let θ denote the angle between the velocity of a charged particle and the magnetic field, then, the magnetic flux density is given by

$$B = \frac{F}{v\sin(\theta)} \tag{2.10}$$

To find the force generated in an electric motor, it is necessary to consider not a single charge but a conductor. In particular, for a conductor of length \vec{l} , carrying a current I, exposed to a uniform magnetic flux density \vec{B} , it is subjected to a force expressed as [3]:

$$\vec{F} = I(\vec{l} \times \vec{B}) \tag{2.11}$$

From this equation is easy to understand that for an electric motor is ideal to maximize both the current and the magnetic flux density. One way to increase \vec{B} is by either raising the current in the coil or increase the number of turns. To quantify the ability to increase the magnetic flux density is convenient to use the magneto-motive force (m.m.f.) defined as: $m.m.f = \mathcal{F} = NI$ [Ampere - turns]

2.2.3 Ampere's Law

As discussed in the previous sections, electric motors fundamentally rely on magnetic fields to generate torque. This leads to the need for efficient methods to produce and control magnetic fields. Ampère's Law provides a theoretical basis for this, relating the magnetic field generated around a conductor to the current flowing through it. With Maxwell's correction, the law also accounts for the magnetic field induced by a time-varying electric field [4].

Ampère's Law can be expressed in its integral form as:

$$\oint_{\Gamma} \vec{H} \cdot d\vec{l} = I_{enc} + \frac{\partial}{\partial t} \int_{S} \vec{D} \cdot d\vec{S} = \int_{S} \vec{J} \cdot \vec{S} + \frac{\partial}{\partial t} \int_{S} \vec{D} \cdot d\vec{S}$$
 (2.12)

where:

- $\vec{H} = \vec{B}/\mu$ is the magnetic field intensity, representing the strength and direction of the magnetic field in the medium.
- μ is the magnetic permeability of the material, which determines how easily the material can be magnetized.
- $\vec{D} = \varepsilon \vec{E}$ is the electric displacement field, accounting for the effect of the material on the electric field.
- $\varepsilon = \varepsilon_0 \varepsilon_r$ is the electric permittivity of the material, combining the permittivity of free space \mathcal{E}_l and the relative permittivity \mathcal{E}_{∇} of the medium.
- \vec{J} is the current density vector, representing the amount of current flowing per unit area.
- \vec{S} is the surface bounded by the closed path Γ

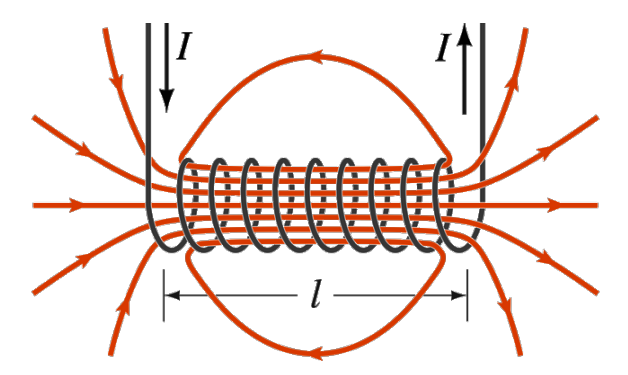


Figure 2.2.1: Application of Ampere's law in a solenoid. The current flowing through it generates a magnetic field whose direction is given by the right-hand rule.

• $d\vec{l}$ is an infinitesimal vector element of the path Γ ,

In most practical cases involving electric machines, the displacement current term is negligible, except when analysing electromagnetic waves [4]. Under this assumption, Ampère's Law reduces to:

$$\oint_{\Gamma} \vec{H} \cdot d\vec{l} = I_{\text{enc}} \tag{2.13}$$

Thanks to that it is possible for example to produce a rotating magnetic field by supply a set of three-phase currents, each phase shifted by 120° , to a tri-phase winding.

2.2.4 Faraday-Neumann-Lenz's Law

Discovered by Michael Faraday in 1831, the Faraday-Neumann-Lenz's law, describes how a changing magnetic field induces an electromotive force [4]. In particular, Lenz's law defines the polarity of this induced EMF: it will always oppose the change in magnetic flux that produced it. This opposing nature is why it is commonly termed back electromotive force. In its integral form is expressed as:

$$\oint_{\Gamma} \vec{E} \cdot d\vec{l} = -\frac{d}{dt} \int_{S} \vec{B} \cdot d\vec{S}$$
(2.14)

A more compact formulation is:

$$\mathcal{E} = -\frac{d\Phi}{dt} \tag{2.15}$$

This law is indispensable for the operation of induction motors. In these machines, the rotor is not connected to an external power source; instead,

the rotating magnetic field from the stator induces a voltage in the rotor via Faraday's Law. This induced voltage then drives the current that creates the rotor's magnetic field, enabling torque production.

Furthermore, back EMF acts as a natural current regulator. The magnitude of the back EMF is proportional to the motor's angular velocity $(\mathcal{E} \propto \omega)$. According to the motor voltage equation:

$$I = \frac{V_{\text{supply}} - \mathcal{E}}{R} \tag{2.16}$$

As the motor's speed increases, \mathcal{E} increases, thereby automatically limiting the current draw and torque output.

Without this critical feedback mechanism, the Lorentz force would cause continuous acceleration, and with no opposing back EMF to limit current, the motor would theoretically accelerate toward infinite velocity. In practice, it would draw excessive current and be destroyed by overheating or mechanical failure long before reaching such speeds.

2.2.5 Magnetic Circuits

The design and analysis of electromagnetic devices like transformers, motors, and generators are greatly simplified by the concept of a magnetic circuit [2]. In this analogy, the magnetomotive force \mathcal{F} plays the role of voltage. Just as a voltage drives an electric current through a conductor, an m.m.f. drives a magnetic flux Φ through a magnetic core.

Similarly, the concept of reluctance \mathcal{R} in Hopkinson's law is analogous to resistance in Ohm's law. The relationship can therefore be expressed as:

$$\mathcal{F} = \mathcal{R} \Phi \tag{2.17}$$

It is important to remember that the magnetic circuit model is an approximation that relies on several key assumptions [2]:

- Perfect Flux Confinement: The model assumes all magnetic flux is confined within the high-permeability magnetic core, with no leakage into the surrounding air. In reality, the reluctance of air, while high, is not infinite. Consequently, a small portion of the flux, known as leakage flux, will always take a path outside the core, slightly reducing the effective flux in the desired part of the circuit. text
- Constant Permeability: The model typically assumes the permeability μ of the core material is constant, meaning the relationship between magnetic field strength (H) and flux density (B) is linear. However, ferromagnetic materials exhibit non-linearity and saturation. As the m.m.f. increases, the material eventually saturates and its permeability drops dramatically, as will be further discussed in subsequent chapters.

• Uniform Flux Distribution: It is assumed that the flux is distributed uniformly across the cross-section of the core. In practice, this may not hold true at corners or in complex geometries due to fringing effects.

2.2.6 Torque, Moment of Inertia, and Mechanical Power

In the study of electric motors, linear velocity is seldom used due to the inherently rotational nature of motor motion. Instead, it is more common to refer to quantities such as torque and moment of inertia.

Torque is defined as the product of the force applied to a body and the perpendicular distance between the line of action of the force and the axis of rotation [2]. By considering the position vector \vec{r} pointing from the axis of rotation to the point of application of a force \vec{F} , the torque τ can be expressed as:

$$\tau = \vec{r} \times \vec{F} = Fr\sin(\theta) \tag{2.18}$$

The SI unit of torque is the newton-metre $[N \cdot m]$.

Analogous to linear motion, where force is the product of mass and linear acceleration (F = ma), an equivalent relationship exists in rotational motion between torque and angular acceleration:

$$\tau = J\alpha \tag{2.19}$$

Here, J denotes the moment of inertia, measured in $kg \cdot m^2$, and α is the angular acceleration, measured in rad/s^2 . Angular acceleration is defined as the time derivative of angular velocity ω , expressed in rad/s.

In linear motion, work is defined as the product of the applied force and the displacement of the object. Similarly, in rotational motion, the work done is equal to the torque applied to rotate a body through an angular displacement θ :

$$W = \int \tau \, d\theta \tag{2.20}$$

Finally, mechanical power in rotational systems is defined as the time derivative of work. Hence, power can be expressed as:

$$P = \tau \omega \tag{2.21}$$

2.3 Structure of an AC motor

Now that the electromagnetic forces involved in an electric motor, it is necessary to understand its main components. The main parts of a three phase AC motor are: rotor, stator, winding and enclosure [5].

2.3.1 Stator

The stator, as the name suggests, is the stationary part of the motor. It consists of a laminated iron core designed to reduce eddy current losses, and within this core, slots are created to accommodate the stator windings. These windings are distributed and placed at equal intervals around the circumference of the stator in order to establish a balanced three-phase system. When an alternating current is supplied to the windings, a rotating magnetic field is generated, which will interact with the rotor to produce motion.

Classification Based on Magnetic Flux Path

The path of the magnetic flux defines the type of magnetic circuit within the machine and leads to a primary classification based on the direction of the main magnetic flux relative to the axis of rotation.

- Radial Flux Machines (RFM): it is the most common and traditional configuration. The magnetic flux path is radial; it flows perpendicular to the axis of rotation, moving radially outward or inward across the air gap. In this structure, the stator windings are typically housed in slots on the inner surface of a cylindrical core, with the rotor fitted inside. RFMs are widely adopted due to their mechanical robustness, manufacturing simplicity, and proven reliability [6].
- Axial Flux Machines (AFM): In this design, the magnetic flux path is axial; it flows parallel to the axis of rotation. This necessitates a design where the rotor and stator are parallel discs facing each other, leading to a characteristic disc-shaped geometry with a short axial length and large diameter. This configuration offers a significantly larger active air gap surface area for a given volume compared to radial flux machines. The result is a much higher torque and power density, making AFMs compact and lightweight, while also exhibiting high efficiency, particularly at low speeds [6].
- Transverse Flux Machines (TFM): Here, the magnetic flux path is three-dimensional, flowing perpendicular to the rotor motion within the plane of the air gap. TFMs can achieve extremely high torque density at very low speeds, theoretically the highest among the three types. Moreover, the decoupling of the winding path from the magnetic flux path enables greater flexibility in maximizing copper and iron utilization. However, the unconventional structure introduces challenges: even minor pole misalignments can cause detent torque, acoustic noise, and significant construction difficulties [7, 8].

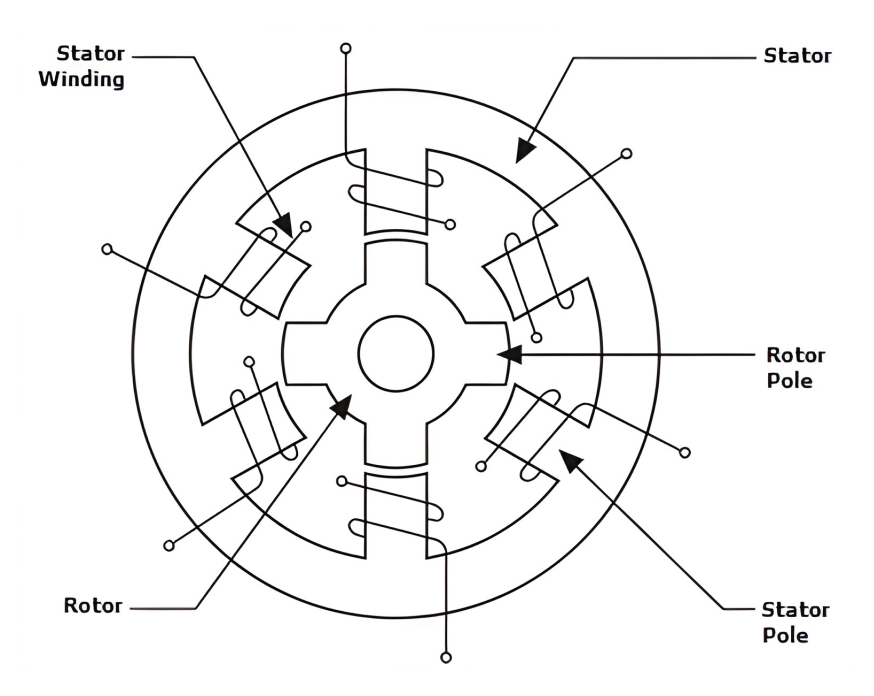


Figure 2.3.1: Example of the basic structure of a switched reluctance motor.

2.3.2 Rotor

It is the rotating part of the motor, here winding or permanent magnets can be found.

The rotor is mounted on a central shaft, allowing it to convert electromagnetic energy into mechanical rotation. Its movement is enabled by the continuous interaction with the magnetic field generated by the stator, producing torque that drives the shaft [9]. In motors with wound rotors, current flows through the windings to create an electromagnet, while in permanent magnet rotors, the built-in magnetic field interacts directly with the stator's field. This rotation ultimately delivers the mechanical power necessary to drive external loads such as fans, pumps, or wheels [9].

2.3.3 Windings

In electric motors, windings are used as electromagnets to generate the magnetic field required for operation. These windings consist of coils of conductive wire, typically copper, wound around a core. When current flows through them, they create a magnetic flux that interacts with either a permanent magnet or another set of windings to produce torque. Depending on the type of motor, the windings may be designed to carry either alternating or direct current [9].

According to coil arrangement, two main categories of windings can be

distinguished: concentrated and distributed winding. The first refers to a technique where only a single coil is wound around one tooth. Since this type of winding is mainly use for DC motors, not much focus will be put on it in this work [10]. On the other hand, when the coils are spread across multiple teeth, the winding is referred as distributed winding. This structure is preferred for high efficiency application since it produced a smoother sinusoidal EMF compared to the concentrated structure that produce a more trapezoidal wave [10]. For distributed winding, several parameters are of particular interest [11]:

- Number of slots in the stator N, where the coils will be placed.
- Number of **phases** m, used to generate the rotating magnetic field.
- Polar pairs p_p , i.e., the number of magnetic circuit in the motor, which links the electrical angle θ_e to the mechanical angle θ_m through the relation $\theta_e = p_p, \theta_m$.
- Pole pitch τ , defined as the distance, in terms of slots, between two successive poles (north–south), expressed as $\tau = \frac{N}{2 p_p}$.
- Coil pitch, is the distance between 2 sides of a coils. If it is equal to the pole pitch then the winding is a full pitch winding, otherwise is a fractional or a chorded winging.

Based on the number of winding layers, they can be classified into single or double layer winding [11, 10].

- In a **single-layer winding**, each slot accommodates only one coil side.
- In a double-layer winding, each slot contains two coil sides belonging to different coils. This configuration allows twice as many coils to be used compared to the single-layer design. Additionally, higher-order harmonics can be reduced by slightly extending or shortening the coil pitch. This process makes it possible to achieve a fractional pitch.

Depending on how the coils are interconnected, the winding can be either lap or wave [12]:

• Lap winding: in a lap winding, the end of one coil is connected to the beginning of the next coil located under the same pair of poles. This creates a parallel path structure where the winding resembles a spiral or lap. This kind of connection reduce the reactance between coils, improve current distribution, producing more consistent torque and power. It is advised when multiple conductor are placed per slots.

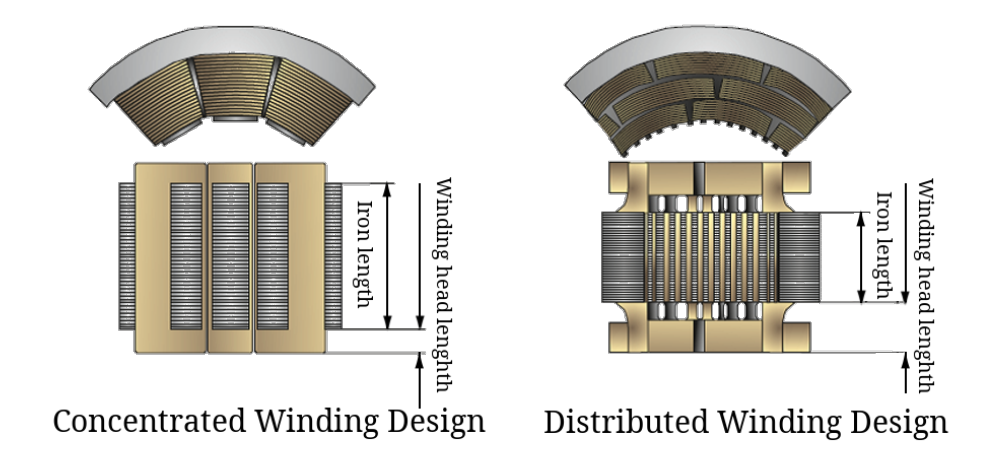


Figure 2.3.2: Comparison between concentrated and distributed winding.

 Wave winding: In a wave winding, the coils are connected in series, progressing sequentially around the armature circumference and linking conductors under successive poles. This creates a more compact design, suitable when only a few conductors are used per slot. However, fractional-pitch configurations are not feasible with this type of winding.

2.3.4 Enclosure

To isolate and protect the main components of the motor, the enclosure functions as a physical barrier that shields the internal parts from the external environment. It prevents the ingress of dust, moisture, and other contaminants, while also providing a degree of mechanical protection against accidental contact or impact. Furthermore, the enclosure plays a role in safety, ensuring that users are not exposed to live or moving components during operation.

Depending on the application and operating conditions, different types of motor enclosures are available, each designed to balance cooling requirements, environmental protection, and cost-effectiveness. Common enclosure designs include open drip-proof (ODP), totally enclosed fan-cooled (TEFC), and explosion-proof housings, each offering specific advantages suited to particular industrial environments [5, 9].

2.4 Main Components of an Electric Powertrain

When discussing an electric powertrain, it is essential to understand its main components [13, 14]:

- **Electric motor**: Converts electrical energy into mechanical energy, providing the torque required to propel the vehicle. Its design and control strongly influence the vehicle's performance and energy efficiency.
- Battery pack: Serves as the main energy storage unit, supplying the electrical energy required for traction and auxiliary systems. Its capacity, energy density, and thermal management directly impact vehicle range, performance, and safety.
- DC/AC converter (inverter): Transforms the DC from the battery into AC for the motor. In addition to enabling forward and reverse operation, the inverter regulates torque and speed by adjusting frequency and voltage. Advanced inverters also allow energy recovery during regenerative braking.
- Battery management system (BMS): Controls the charge and discharge of the battery pack, ensuring optimal performance and safety under varying operating conditions.
- Electric vehicle control unit (EVCU): Acts as the central controller, managing power flow, torque requests, and communication between subsystems. It ensures optimal coordination of energy use and safe operation.
- Transmission with single gear ratio: Unlike internal combustion engines, most electric vehicles use a simplified transmission with a fixed gear ratio. This reduces mechanical complexity while still delivering sufficient torque across the operating range of the motor.
- **DC-DC converters**: These devices are used to step down the high voltage from the battery to the lower voltages required by auxiliary systems (e.g., lighting, infotainment, sensors), and to boost the battery voltage supplied to the inverter.
- On-board charger: Provides the interface between the vehicle and the electric grid. It converts AC input power into DC to recharge the battery pack.
- Thermal management system: Regulates the temperature of multiple components of the powertrain, preventing overheating while maintaining performance and longevity.

Some considerations on the most important parts of the electric powerrain will be discussed below.

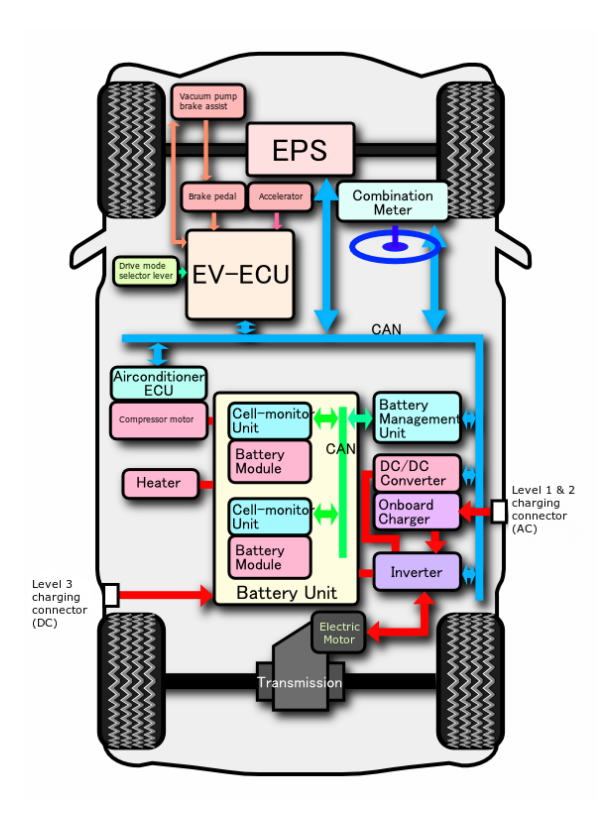


Figure 2.4.1: Powertrain of Mitsubishi iMiEV

2.4.1 Selection of AC motor

Even though DC motor could be used in electric vehicles, their lower efficiency, power density and either higher complexity or higher maintenance make them not an attractive choice. On the other hand, AC motors offer high reliability and robustness, low maintenance while having higher power density and efficiency. For this reason, DC motors will not be considered further in this section [15]. When choosing an AC motor, the selection generally falls into one of the following three main categories:

- Induction motors
- Permanent magnet synchronous motors
- Switched reluctance motors

Choosing the appropriate type of motor can be challenging, as it largely depends on the specific requirements of the intended application. Each type

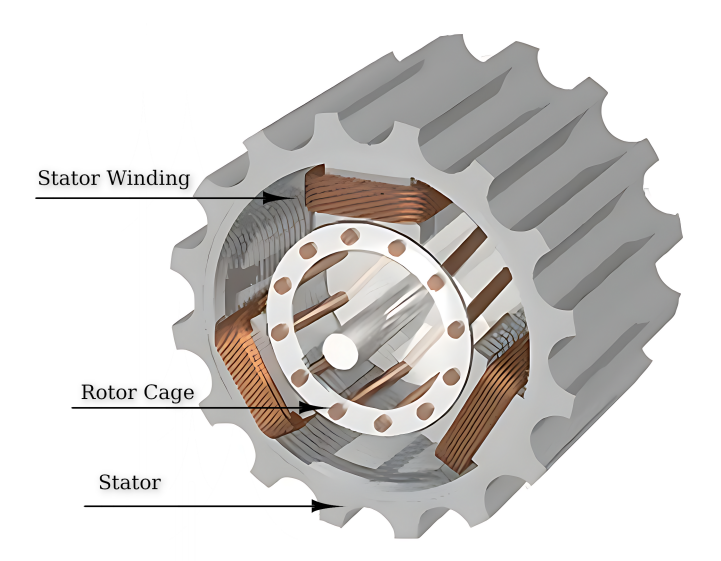


Figure 2.4.2: Structure of an induction motor with squirrel cage rotor.

has its own advantages and limitations, which will be briefly discussed in the following sections.

Induction motors

They rely on the principle of electromagnetic induction, where thanks to the presence of a rotor cage, which effectively behaves as another three phase winding [16]. They are by far the most widely used type of AC motor, accounting for the majority of applications in both industrial and domestic settings. Their popularity comes from their simple structure, the absence of brushes or commutators, and the maturity of the technology, which makes them cost-effective, highly reliable, and relatively easy to maintain. Thanks to these characteristics, induction motors are often considered the most robust and dependable option [17].

Despite these advantages, induction motors also present some notable drawbacks. One of the main issues is their reduced efficiency when operating at higher speeds, as losses in the rotor and stator tend to increase, leading to energy consumption and heat generation. Another significant limitation is their relatively low power factor, which leads to inefficient utilization of electrical power [17, 15].

Permanent Magnet Synchronous Motors

Permanent Magnet Synchronous Motors (PMSMs) are widely used by the majority of EV manufacturers due to their high power density, excellent effi-

ciency, and reduced heat losses compared to conventional induction motors. The use of permanent magnets in the rotor eliminates the need for external excitation current, thereby minimizing copper losses in the rotor, ease the cooling process and improving overall performance [3, 1]

In addition to their efficiency benefits, PMSMs provide better outstanding dynamic response and precise speed control thanks to their synchronous operation [3].

However, these advantages come with notable drawbacks. The primary limitation of PMSMs is their higher cost, mainly due to the use of rare-earth permanent magnets (such as neodymium-iron-boron or samarium-cobalt). Another concern is the risk of demagnetization: excessive heat or strong armature reaction currents can weaken or permanently damage the rotor magnets, leading to reduced performance or motor failure. This makes thermal management and proper current control strategies critical in PMSM design and operation. Additionally, PMSMs have a relatively narrow constant power region, which can be extended through field weakening. This requires additional I_d current, increasing losses and temperature, and further elevating the risk of demagnetization [3, 17].

Switched Reluctance Motors

Switched Reluctance Motors (SRMs) are increasingly popular in various applications due to their cost-effectiveness, high power density, and good efficiency. Their simple construction, which typically involves a rotor with salient poles and a stator with concentrated windings, contributes to lower manufacturing and maintenance costs compared to more complex motor types [1, 15, 17].

However, to achieve high power density, SRMs require a high air gap induction, which can lead to significant acoustic noise during operation. Moreover, SRMs inherently exhibit high torque ripple, especially at low speeds, which can cause vibration and affect performance in precision applications. Controlling SRMs is also more complex than controlling traditional induction motors, as it requires sophisticated current and torque control strategies to manage their nonlinear characteristics effectively [15]. For these reasons, SRMs are not commonly used in EV applications [1], but are considered a strong candidate for electric bikes and scooters [18].

2.4.2 Biggest Concerns about Battery Pack

When evaluating the overall system efficiency, and in particular the tankto-wheel power conversion, it is essential to account for the performance of the main components:

$$P_{out} = P_{Battery} \eta_{DC/DC} \eta_{Inverter} \eta_{Motor} \eta_{Transmission}$$
 (2.22)

In this equation, the battery constitutes the primary technological bottleneck. This limitation mainly comes from its relatively low energy density when compared to conventional fuels such as petrol, which store far greater amounts of energy per unit of mass [13, 19]. As a result, achieving the required energy capacity necessitates large battery packs, which substantially increase the overall weight, cost, and volume of the vehicle.

Beyond these physical constraints, batteries also face technological challenges related to their long-term reliability. Over time, cells suffer from degradation, leading to a gradual reduction in energy storage capacity and power output. Some degradation mechanisms include growth of solid electrolyte interface (SEI), lithium plating, lithium ion loss or uneven distribution within electrodes, electrode volume change due to intercalation and gas formation from side reactions. This degradation impacts both the driving range and the economic lifespan of the system, potentially requiring costly replacements. In addition, lithium-based chemistries present safety risks. External factors (e.g., crash or penetration) or internal ones (e.g., lithium dendrite growth) can trigger short circuits or redox reactions at the electrodes, potentially resulting in thermal runaway and severe accidents.

In contrast, the other components in the efficiency chain contribute far less to overall losses. For instance, modern DC/DC converters and inverters have achieved very high efficiencies, approaching nearly 100% under nominal operating conditions. Electric motors similarly exhibit high efficiency levels across a wide operating range [13], and mechanical transmissions, though not lossless, introduce only minor additional reductions. Consequently, while optimization of these subsystems remains important, the battery continues to dominate as the critical factor in determining both the efficiency and practicality of the overall system.

2.4.3 Type of DC/DC and DC/AC converters

DC/DC converters are needed in the system, mainly to create compatible voltage level that will be feed to the inverter.

In electric drive systems, regenerative braking is a common feature of modern motors. This capability enables the motor to act as a generator during braking, feeding energy back into the system. To capture and store this regenerated energy in the battery, bidirectional DC-DC converters are required. These converters not only step up or step down voltage as needed but also allow current to flow in both directions, enabling seamless energy recovery and storage [18, 20].

For safety and reliability, DC-DC converters are often designed with electrical isolation between the input and output. Isolation is typically achieved using a transformer, which separates the high-voltage side from the low-voltage side. This isolation helps protect sensitive components and users from potential electrical faults, while also reducing electromagnetic interfer-

ence between system stages [18].

The choice of switching devices in DC-DC converters depends on the required power level and switching frequency. At low to medium power levels and high switching frequencies, MOSFETs (Metal-Oxide-Semiconductor Field-Effect Transistors) are generally preferred due to their fast switching capability and high efficiency. For higher power applications or lower switching frequencies, IGBTs (Insulated-Gate Bipolar Transistors) are favoured because of their ability to handle larger currents and voltages with lower conduction losses [18].

Their conversion efficiency may vary but it is usually quite high, more then 90% [18, 20].

The inverter plays another crucial role in the powertrain, acting as the interface between the DC electrical system and the electric motor. Its primary function is to convert the continuous voltage supplied by the DC/DC converter into a three-phase alternating current.

There are mainly two categories of inverters used in automotive applications: two-level inverters and multilevel inverters.

- Two-level inverters: In this configuration, the output voltage can only alternate between two discrete values, corresponding to the positive and negative levels of the DC bus. This simplicity makes them easier to design, cost-effective, and more compact. However, because the voltage waveform is far from a pure sinusoid, significant harmonic distortion is introduced. To reduce these harmonics and their associated losses or electromagnetic interference, bulky filters are often required, which adds weight and volume to the system [20].
- Multilevel inverters: To overcome the drawbacks of the two-level approach, multilevel inverter topologies were developed. These generate multiple voltage steps that approximate a sinusoidal waveform much more closely. The result is lower total harmonic distortion and reduced stress on the motor windings, leading to smoother operation, higher efficiency, and potentially less need for large filtering components. On the other hand, these benefits come at the expense of increased system complexity. Multilevel inverters require a higher number of power semiconductor switches and, in many cases, additional isolated DC sources or capacitors [20].

Like DC/DC converters, modern inverters achieve very high efficiency, with some designs approaching nearly 100% under optimal conditions [20].

Chapter 3

Permanent Magnet Synchronous Motors

In this chapter, focus will be put on PMSMs, describing their main characteristics, key aspects of operation, and common challenges. Particular attention will be placed on the anisotropic PMSM, as it represents the type of motor employed in this work.

3.1 Structure and working principle

Induction motors exploit the principle of electromagnetic induction to create torque, meaning they do not require permanent magnets inside the rotor. In fact, the rotating magnetic field generated by the stator in the airgap induces currents in the rotor conductors, and these induced currents in turn generate their own magnetic field that interacts with the stator field to produce torque. Because the rotor field is induced rather than directly excited, a relative speed difference is necessary between the stator's rotating magnetic field (synchronous speed, N_s) and the actual mechanical speed of the rotor (N). This difference, known as slip, ensures that induction can take place and therefore torque is produced [16]. Slip is formally defined as:

$$s = \frac{N_s - N}{N} = \frac{\omega_r}{\omega_s} \tag{3.1}$$

$$N_s = \frac{60 f}{p_p} \tag{3.2}$$

Where ω_r and ω_s are the angular frequency of the rotor and stator currents, while p_p is the number of pole pairs. A non-zero slip is therefore inherent to the operation of induction motors, which is why they are commonly referred to as asynchronous machines. In steady-state operation, the slip is usually

small (a few percent), but it increases under high load conditions to allow more torque production [3, 1].

In contrast, permanent magnet synchronous motors (PMSMs) rely on permanent magnets embedded in or attached to the rotor to establish a constant magnetic field. High-performance materials such as Samarium-Cobalt, known for their high flux density and coercivity, are traditionally used. More recently, Neodymium-Iron-Boron magnets have gained widespread adoption due to their lower cost [16, 21].

The rotor magnetic field locks into synchronism with the stator's rotating field, which means the rotor speed N is exactly equal to the synchronous speed N_s , and therefore the slip is zero in steady state. This synchronous operation provides high efficiency, better torque density, and precise speed control compared to induction motors, but at the cost of requiring expensive rare-earth materials for the magnets [3, 21].

Depending on the placement of the magnets within the rotor structure, PMSMs can be further categorized into [16]:

- Interior PM synchronous motors (IPMSM): the magnets are buried inside the rotor, providing higher saliency, better torque-perampere ratio, and significant reluctance torque [16]
- Surface-mounted PM synchronous motors (SPMSM): these can be further divided into projecting and inset types. In the first type the magnets are mounted directly on the rotor surface, leading to simple construction, low cost but no reluctance torque and low robustness. In the inset type, the magnet are partly embedded, combining characteristics of both surface and interior designs.

To obtain smooth and efficient torque generation in electric machines, it is essential to ensure that both the back electromotive force (BEMF) and the current excitation waveforms are sinusoidal. Achieving a sinusoidal BEMF typically requires that the stator windings be distributed in a sinusoidal pattern around the stator. In addition, feeding the machine with sinusoidal current excitations ensures that the interaction between the magnetic fields of the rotor and stator produces a smooth, continuous torque. Deviations from sinusoidal waveforms, whether in the BEMF or current, can result in torque ripple, increased acoustic noise, and reduced efficiency [22].

3.2 Vector Control

For simplicity, an isotropic motor is considered; the anisotropic case will be addressed in a subsequent section. During the operation of an PMSM, it is desirable to obtain the maximum torque with the minimum stator current. The stator magnetomotive force vector \vec{I}_s can be decomposed into two orthogonal components: one in the same direction of the rotor flux (direct axis

or d-axis), while the other perpendicular to it (quadrature axis or q-axis). Since the motor already contains a permanent magnet, no additional flux can be generated. Therefore, the d-axis current does not contribute to torque production. The torque is produced solely by the q-axis component. For this reason, to maximize the production of torque the stator mmf must be perpendicular to the rotor flux. To achieve that, the instantaneous position of the rotor flux must be sensed while carefully controlling the instantaneous position to the stator mmf. This means that both the amplitude and the phase of the stator currents must be controlled. This type of control is called Vector Control [16]. This can be achieved using either Direct Torque Control (DTC), which operates in the stator reference frame, or Field-Oriented Control (FOC), which operates in the rotor reference frame [16]. Both strategies are widely adopted in industrial applications, and neither has emerged as universally superior [23]. In this work, the focus will be placed on the FOC technique.

3.2.1 Field Oriented Control

Even though conventional Proportional-Integral (PI) controllers can be effectively applied in direct current systems to minimize steady-state error, their performance becomes significantly limited when used in alternating current applications. This limitation arises because AC motors inherently require dynamic tracking of sinusoidal signals, while PI controllers are fundamentally designed to regulate constant reference values. As a result, when employed in AC motor control, conventional PI controllers are unable to achieve zero steady-state error. Instead, they exhibit a persistent error caused by their delayed tracking response, which comes from the fact that their proportional gain cannot be infinitely large. In practice, this means that the controller cannot perfectly follow the oscillatory nature of the AC reference, leading to an inevitable offset in performance.

To overcome this drawback, an approach is to employ a rotating reference frame (also known as the synchronous reference frame). By transforming the AC quantities into a rotating coordinate system, the sinusoidal signals are effectively converted into constant values in steady state. Under this transformation, the control problem is simplified to that of regulating direct current like quantities, thereby enabling the PI controller to eliminate the steady-state error [24].

$\alpha - \beta$ and d-q reference system

In order to obtain a rotating reference frame that is synchronous with the rotating magnetic field of the rotor, two mathematical transformations are applied: the Clarke transformation and the Park transformation.

The Clarke transformation projects a three-phase system (a, b, c) onto

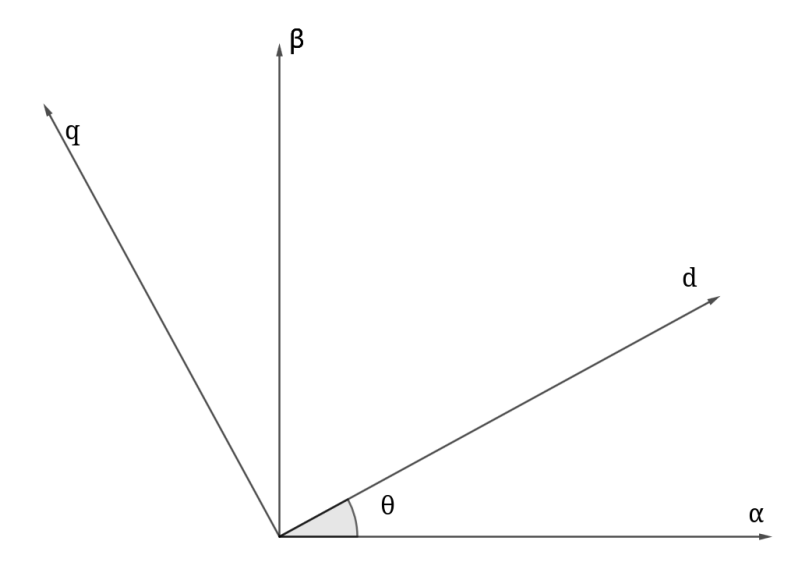


Figure 3.2.1: Phasor diagram of $\alpha-\beta$ and d-q reference system

a two-axis orthogonal reference frame, typically denoted as (α, β) plane. This transformation reduces the dimensionality of the system by eliminating redundancy, since the three-phase quantities are linearly dependent. The resulting $\alpha - \beta$ components represent a two-phase equivalent of the original three-phase signals in a stationary, non-rotating coordinate system. The mathematical transformation is given by:

$$\begin{bmatrix} i_{s\alpha} \\ i_{s\beta} \end{bmatrix} = K \begin{bmatrix} 1 & -\frac{1}{2} & -\frac{1}{2} \\ 0 & \frac{3}{2} & -\frac{3}{2} \end{bmatrix} \begin{bmatrix} i_{su} \\ i_{sv} \\ i_{sw} \end{bmatrix}$$
(3.3)

where the scaling factor K can be chosen as $K = \frac{2}{3}$ for constant amplitude or $K = \sqrt{\frac{2}{3}}$ for constant power and energy.

By applying the Park transformation it is possible to obtain from a stationary coordinate system $(\alpha - \beta)$ a synchronously rotating frame aligned with the rotor flux (d, q). The mathematical transformation in this case is given by:

$$\begin{bmatrix} i_{sd} \\ i_{sq} \end{bmatrix} = \begin{bmatrix} \cos \theta & \sin \theta \\ -\sin \theta & \cos \theta \end{bmatrix} \begin{bmatrix} i_{s\alpha} \\ i_{s\beta} \end{bmatrix}$$
(3.4)

where θ is the angle between the axis d and the reference system $\alpha - \beta$. In this rotating reference frame, alternating currents and voltages appear as DC quantities under steady-state conditions, which significantly simplifies

the analysis and control of AC machines. In the case of electric motors the d-axis is aligned with the rotor magnetic pole while the q-axis is shifted from 90°, this is why it is called quadrature axis [24].

3.3 Torque and voltage equations

3.3.1 Simplified case

To control the speed and torque of the electric motor, it is first essential to derive the electromagnetic torque equation. To do so, some simplifying assumptions are introduced:

- the motor has an isotropic structure,
- magnetic circuit saturation is neglected.

Under these assumptions, the stator voltage equations for the three phases a, b, and c can be expressed as:

$$u_a(t) = R i_a(t) + \frac{d\lambda_a(t)}{dt}$$

$$u_b(t) = R i_b(t) + \frac{d\lambda_b(t)}{dt}$$

$$u_c(t) = R i_c(t) + \frac{d\lambda_c(t)}{dt}$$
(3.5)

where i_a, i_b, i_c are the phase currents while $\lambda_a, \lambda_b, \lambda_c$ are the corresponding magnetic flux linkages. If saturation is neglected, magnetic flux linkages can be written as:

$$\lambda_{a}(t) = \lambda_{a,pm}(t) + \lambda_{a,i}(t)$$

$$\lambda_{b}(t) = \lambda_{b,pm}(t) + \lambda_{b,i}(t)$$

$$\lambda_{c}(t) = \lambda_{c,pm}(t) + \lambda_{c,i}(t)$$
(3.6)

where $\lambda_{a,pm}$ is the magnetic flux linkage generated by the permanent magnet while $\lambda_a, i(t)$ represents the flux linkage due to the phase-a current.

It is convenient to define the electrical angle θ_e as the angle between the phase-a magnetic axis and the d-axis of the rotor, which aligns with the magnetic field produced by the permanent magnets. The relationship between electrical and mechanical quantities is governed by the number of pole pairs p_p , which represents the number of magnetic periods per mechanical revolution. This scaling applies uniformly to both angular positions and velocities:

$$\theta_e = p_p \theta_m \omega_e = p_p \omega_m$$
 (3.7)

where ω_e and ω_m are the electrical and mechanical angular velocities, respectively.

Under no-load conditions (i.e., with zero stator current), the flux linkages induced in the stator windings by the permanent magnets are purely sinusoidal and spatially shifted by 120°. These are given by:

$$\lambda_{a,pm} = \Lambda_{pm} \cos(\theta_e)$$

$$\lambda_{b,pm} = \Lambda_{pm} \cos\left(\theta_e - \frac{2\pi}{3}\right)$$

$$\lambda_{c,pm} = \Lambda_{pm} \cos\left(\theta_e + \frac{2\pi}{3}\right)$$
(3.8)

Here, Λ_{pm} denotes the peak flux linkage due to the permanent magnets, which is a constant parameter determined by the magnet strength and winding configuration for a given machine. This fundamental parameter can be experimentally determined or expressed through several equivalent relationships:

$$\Lambda_{pm} = \frac{K_e}{p_p} = \frac{E_{peak}}{\omega_e} \tag{3.9}$$

where E_{peak} denotes the peak phase BEMF and K_e is the BEMF constant which is also equal to the torque constant K_t [25].

In compact form:¹

$$\vec{\lambda}_{pm}^s = \Lambda_{pm} \ e^{j\theta_e} \tag{3.10}$$

Where s denotes the stationary $\alpha-\beta$ reference frame. If the α -axis is aligned with the phase a axis, then $\vec{\lambda}_{mg}^s$ is aligned with the stator reference frame. This explains why, in Chapter 3.2.1, the $\alpha-\beta$ reference system was described as stationary.

Assuming the motor isotropic, the total magnetic flux linkages can be expressed as:

$$\lambda_{a} = L_{a}i_{a} + L_{Mab}i_{b} + L_{Mac}i_{c} + \lambda_{a,pm} = L_{ss}i_{a} - |L_{Mss}|(i_{b} + i_{c}) + \lambda_{a,pm}$$

$$\lambda_{b} = L_{b}i_{b} + L_{Mab}i_{b} + L_{Mbc}i_{c} + \lambda_{b,pm} = L_{ss}i_{b} - |L_{Mss}|(i_{a} + i_{c}) + \lambda_{b,pm}$$

$$\lambda_{c} = L_{c}i_{c} + L_{Mbc}i_{b} + L_{Mac}i_{a} + \lambda_{c,pm} = L_{ss}i_{c} - |L_{Mss}|(i_{a} + i_{b}) + \lambda_{c,pm}$$
(3.11)

where:

$$L_a = L_b = L_c = L_{ss} L_{Mab} = L_{Mac} = L_{Mbc} = -|L_{Mss}|$$
(3.12)

¹From this point forward, explicit time dependence will be omitted for notational simplicity.

since in PMSM the sum of the phase currents is zero:

$$\lambda_{a} = L i_{a} + \lambda_{a,pm}$$

$$\lambda_{b} = L i_{b} + \lambda_{b,pm}$$

$$\lambda_{c} = L i_{c} + \lambda_{c,pm}$$
(3.13)

where $L = L_{ss} + |L_{Mss}|$ is the synchronous inductance. Rewriting the stator voltage equations in terms of the space vector, we obtain:

$$\vec{u} = R \,\vec{i}^s + L \frac{d\vec{i}^s}{dt} + \vec{e}^s = R \,\vec{i}^s + L \frac{d\vec{i}^s}{dt} + j \,\omega_{em} \,\vec{\lambda}_{pm}^s$$

$$(3.14)$$

where \vec{e} is the space vector of the back electromotive forces induced by the rotor's permanent magnets. The BEMFs can be expressed in their expanded form as:

$$e_a = E_{peak} \sin(\theta_{el}) = E_{peak} \cos(\theta_{el} + \frac{\pi}{2})$$

$$e_b = E_{peak} \cos(\theta_{el} + \frac{\pi}{2} + \frac{2\pi}{3})$$

$$e_c = E_{peak} \cos(\theta_{el} + \frac{\pi}{2} - \frac{2\pi}{3})$$

$$(3.15)$$

The instantaneous power absorbed by the motor is given by the equation:

$$p(t) = u_a i_a + u_b i_b + u_c i_c =$$

$$= R(i_a^2 + i_c^2 + i_c^2) + L \frac{1}{2} \frac{d}{dt} (i_a^2 + i_c^2 + i_c^2) + e_a i_a + e_b i_b + e_c i_c$$
(3.16)

where:

- $p_R = R(i_a^2 + i_b^2 + i_c^2)$, is the power dissipated as heat due to Joule effect.
- $p_L = L \frac{1}{2} \frac{d}{dt} (i_a^2 + i_b^2 + i_c^2)$, is the power related to the variations in the magnetic energy stored in the stator windings.
- $p_{EM} = e_a i_a + e_b i_b + e_c i_c$, is the electrical power converted into mechanical power.

A simplification can be obtained by using rotating reference system (q-d), in particular:

$$\vec{u} = R \, \vec{i}^r + L \frac{d\vec{i}^r}{dt} + j\omega_e \, L \vec{i}^r + j\omega_e \Lambda_{pm}$$
(3.17)

By separating the real and imaginary parts, the voltage equations become:

$$u_d = Ri_d + L\frac{di_d}{dt} - \omega_e Li_q$$

$$u_q = Ri_q + L\frac{di_q}{dt} + \omega_e Li_d + \omega_e \Lambda_{pm}$$
(3.18)

In this case the instantaneous power absorbed by the motor is given by the equation:

$$p(t) = \frac{3}{2}(u_d i_d + u_q i_q) =$$

$$= R\left(i_d^2 + i_q^2\right) + L\left(i_d \frac{di_d}{dt} + i_q \frac{di_q}{dt}\right) + \omega_e \Lambda_{pm} i_q$$
(3.19)

Where the last term, $\omega_e \Lambda_{pm} i_q$ represents the electrical power that is converted into mechanical power. From this, the torque can be expressed as:

$$m = \frac{3}{2} p_p \Lambda_{pm} i_q \tag{3.20}$$

This shows that the torque is generated only by the q-axis current component, as described in chapter 3.2.

3.3.2 Anisotropic case

Not all PMSM are isotropic: some motors exploit the magnetic anisotropy to produce additional reluctance torque. This means that some assumption about mutual and self inductances are not valid any more. The equations presented in (3.18), must be modified as:

$$u_{d} = Ri_{d} + L_{d} \frac{di_{d}}{dt} - \omega_{e} L_{q} i_{q}$$

$$u_{q} = Ri_{q} + L_{q} \frac{di_{q}}{dt} + \omega_{e} L_{d} i_{d} + \omega_{e} \Lambda_{pm}$$
(3.21)

where L_d is the direct synchronous inductance while L_q is the quadrature synchronous inductance. In this case, the torque expression becomes [26]:

$$m = \frac{3}{2} p_p [\Lambda_{pm} i_q + i_d i_q (L_d - L_q)]$$
(3.22)

where the term $i_d i_q (L_d - L_q)$ is the reluctance torque.

3.4 Control Strategies

Based on the operating limits, different control strategies can be applied to a PMSM. Of particular interest are the Maximum Torque per Ampere (MTPA), Maximum Torque per Voltage (MTPV), and Field Weakening (FW) strategies.

3.4.1 Maximum Torque per Ampere

The MTPA (Maximum Torque per Ampere) strategy aims to maximize the torque produced for a given current amplitude. To analyse this, it is convenient to express the d-q axis currents, I_d and I_q , as components of a single current space vector \vec{I} defined as [27]:

$$\vec{I} = Ie^{j\gamma} \tag{3.23}$$

From this, the following relations hold:

$$I_q = I\sin(\gamma), \quad I_d = I\cos(\gamma)$$
 (3.24)

Using these expressions, the torque equation (3.22) can be rewritten as:

$$T = \frac{3}{2} p_p \left[I \sin(\gamma) \Lambda_{pm} + I^2 \cos(\gamma) \sin(\gamma) (L_d - L_q) \right]$$
(3.25)

Since the goal is to maximize the torque for a fixed current amplitude I, it is necessary to compute the condition:

$$\frac{\partial (T/I)}{\partial \gamma} = \Lambda_{pm} \cos(\gamma) + I(L_d - L_q) \left(\sin^2(\gamma) - \cos^2(\gamma) \right) = 0$$
 (3.26)

This expression assumes that both the inductances and the permanent magnet flux linkage are constant. However, this simplification neglects the non-linear effects discussed in previous sections—particularly magnetic saturation and cross-saturation. As described in Chapter 3.6.1, these effects cause the inductances L_d and L_q to vary with the current components I_d and I_q . Moreover, since both currents generate magnetic fields that interact with the permanent magnet field, the effective value of Λ_{pm} also changes. This behaviour, related to the hysteresis phenomena discussed in Chapter 3.6.2, must be taken into account for accurate modelling.

To include these nonlinearities, the torque optimization condition can be modified as [27]:

$$\Lambda_{pm}(I,\gamma)\sin(\gamma) + I \left[\frac{\partial L_d(I,\gamma)}{\partial \gamma} - \frac{\partial L_q(I,\gamma)}{\partial \gamma} \right] \left(\sin^2(\gamma) - \cos^2(\gamma) \right) = 0 \quad (3.27)$$

It is important to note that the MTPA control strategy can only be applied when the motor speed Ω_m is below the base speed Ω_B , at which the nominal torque can still be produced. Above this speed, other strategies such as Field Weakening or MTPV must be employed.

3.4.2 Field Weakening

When the motor speed exceeds the base speed Ω_B , the Field Weakening (FW) strategy can be employed to further increase the motor speed, albeit

at the expense of reduced torque production. The name "Field Weakening" originates from the fact that a negative I_d current is applied, generating a magnetic field that opposes the flux produced by the permanent magnets. This reduction of the net flux allows the back-EMF to remain within the voltage limits of the inverter, enabling operation at speeds beyond the nominal range.

3.4.3 Maximum Torque per Voltage

The Maximum Torque per Voltage (MTPV) strategy is applicable to certain types of motors, particularly those with low short-circuit currents. In this strategy, the control objective is to maximize the torque output while respecting the voltage constraints imposed by the inverter. MTPV becomes especially important at high speeds, where the voltage limit prevents the application of the nominal current and conventional MTPA control is no longer feasible.

3.5 Operating Limits

This section analyses the operational constraints of Permanent Magnet Synchronous Motors imposed by the inverter's current and voltage ratings. The motor is assumed to be in steady-state operation, meaning stator currents and voltages are sinusoidal with constant amplitude and frequency, and the mechanical angular velocity, Ω_m , is constant. The analysis is conducted in the rotor-oriented synchronous reference frame (dq-frame).

3.5.1 Operating Limits for Isotropic Rotors

The primary constraints are derived from the inverter's maximum available DC-link voltage and the motor's thermal limits.

Current Limit

The stator current is limited by the inverter's current rating and the motor's thermal capacity to prevent excessive Joule losses. This defines a circular limit in the dq-plane:

$$I_d^2 + I_q^2 \le I_N^2 \tag{3.28}$$

where I_N is the nominal RMS current magnitude.

Voltage Limit

The stator voltage is limited by the available DC-link voltage. Using the steady-state voltage equations (3.21) and neglecting the small stator resis-

tance voltage drop, the constraint $U_d^2 + U_q^2 \le U_N^2$ becomes:

$$(\Omega_m L I_q)^2 + (\Omega_m L I_d + \Omega_m \Lambda_{pm})^2 \le U_N^2$$
(3.29)

Dividing through by $(\Omega_m L)^2$ yields the voltage limit in the current plane:

$$\left(I_d + \frac{\Lambda_{pm}}{L}\right)^2 + I_q^2 \le \left(\frac{U_N}{\Omega_m L}\right)^2 \tag{3.30}$$

This represents a circle whose centre and radius are speed-dependent.

For isotropic rotors $(L_d = L_q = L)$, the constraints (3.28) and (3.30) are both circles in the I_d – I_q plane.

- The **current limit** is a circle centred at the origin (0,0) with radius I_N .
- The voltage limit is a circle centred at $(I_{Cd}, I_{Cq}) = (-\Lambda_{pm}/L, 0)$ with a radius $U_N/(\Omega_m L)$ that decreases with speed.

The center of the voltage-limit circle corresponds to the short-circuit current obtained when the motor is spun with its terminals short-circuited. The electromagnetic torque, $m = \frac{3}{2}p_p\Lambda_{pm}I_q$, is proportional to I_q , making loci of constant torque horizontal lines.

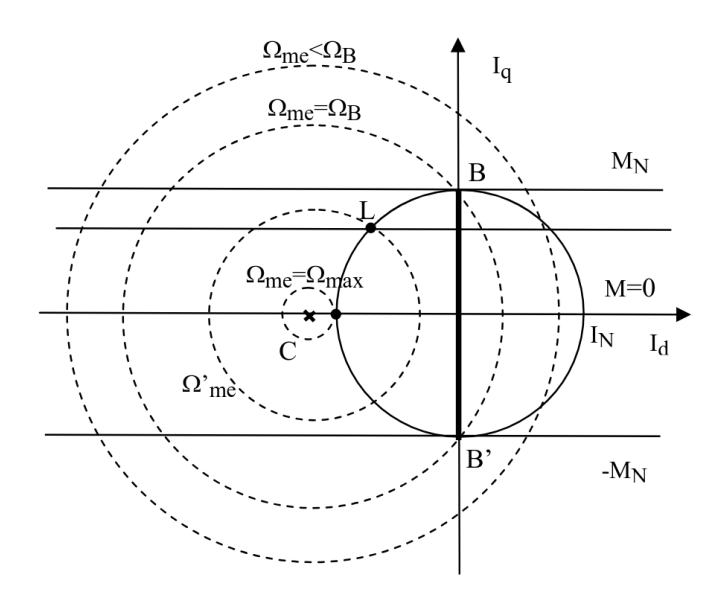


Figure 3.5.1: Operating limits in the I_d – I_q plane for an isotropic rotor. The current-limit circle is fixed. The voltage-limit circles shrink and shift with speed. The MTPA trajectory is along $I_d = 0$. The dashed horizontal lines represent constant torque [26].

The feasible operating points at any speed are those inside both the current-limit circle and the voltage-limit circle. Two characteristic scenarios emerge based on the relative position of the voltage-limit centre.

Voltage-Limit Center Outside Current Circle (High Short-Circuit Current)

This occurs when $\left|\frac{\Lambda_{pm}}{L}\right| > I_N$, i.e., the short-circuit current magnitude is larger than the nominal current.

• Below Base Speed ($\Omega_m \leq \Omega_B$): The voltage limit is not restrictive. The maximum torque is achieved at point B in Fig. 3.5.1, where $I_d = 0$ and $I_q = I_N$. This is the Maximum Torque Per Ampere (MTPA) strategy for isotropic machines. The base speed Ω_B is the speed at which the voltage-limit circle first intersects the current-limit circle at point B. Substituting $I_d = 0$, $I_q = I_N$ into (3.30) gives:

$$\Omega_B = \frac{U_N}{\sqrt{(\Lambda_{pm})^2 + (LI_N)^2}} \tag{3.31}$$

• Above Base Speed $(\Omega_m > \Omega_B)$: The voltage limit becomes the dominant constraint. The maximum achievable torque for a given speed is found at the intersection of the current and voltage-limit circles (e.g., point L in Fig. 3.5.1). As speed increases, this intersection point moves towards $I_d = -I_N$, $I_q = 0$. This trajectory is called Field Weakening(FW). The theoretical maximum speed is found by setting $I_d = -I_N$, $I_q = 0$ in (3.30):

$$\Omega_{\text{max}} = \frac{U_N}{\Lambda_{pm} - LI_N} \tag{3.32}$$

Voltage-Limit Center Inside Current Circle (Low Short-Circuit Current)

This occurs when $|\Lambda_{pm}/L| < I_N$.

The operation below base speed is identical to the previous case. The key difference arises above base speed $(\Omega_m > \Omega_B)$. Since the voltage-limit centre is inside the current circle, the two curves always intersect. As for the previous case, for $\Omega_B < \Omega_m < \Omega_P$ the motor works following the FW strategy. When speed increases, the maximum torque point is no longer on the current-limit circle but on the voltage-limit circle itself. It now operates following the MTPV strategy, operating along segments like PP' in Fig. 3.5.2. In this case, there is no finite maximum speed defined by the intersection of the two constraints; the torque asymptotically approaches zero as speed increases.

3.5.2 Operating Limits for Anisotropic Rotors

Interior Permanent Magnet Synchronous Motors (IPMSMs) are characterized by an anisotropic rotor structure, resulting in different synchronous

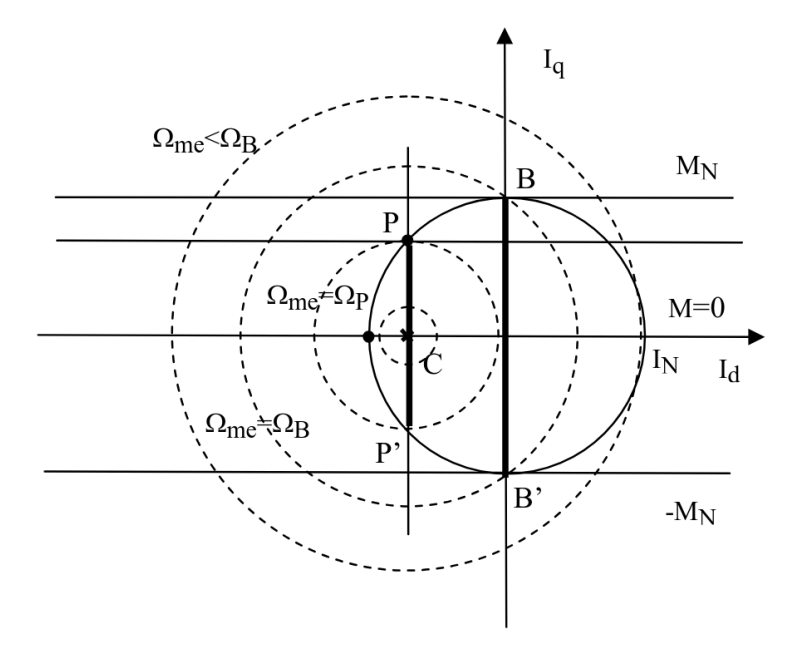


Figure 3.5.2: Operating limits for an isotropic rotor with low short-circuit current. The centre of the voltage-limit circles lies within the current-limit circle. The segment PP' represents the MTPV trajectory [26].

inductances along the direct and quadrature axes $(L_d \neq L_q)$. This magnetic saliency fundamentally alters the geometry of the operational constraints in the $I_d - I_q$ plane compared to the isotropic case.

Voltage Limit Ellipse

Substituting the anisotropic voltage equations into the voltage constraint yields:

$$\left(I_d + \frac{\Lambda_{pm}}{L_d}\right)^2 + \left(\frac{L_q}{L_d}I_q\right)^2 \le \left(\frac{U_N}{\Omega_m L_d}\right)^2$$
(3.33)

This equation describes an ellipse in the I_d - I_q plane, centred at $(I_{Cd}, I_{Cq}) = (-\frac{\Lambda_{pm}}{L_d}, 0)$.

Constant Torque Hyperbolas

The torque equation for an anisotropic motor is:

$$m = \frac{3}{2} p_p \left[\Lambda_{pm} I_q + (L_d - L_q) I_d I_q \right]$$
 (3.34)

Solving for I_q gives the equation for constant-torque contours:

$$I_{q} = \frac{2m}{3p_{p}\left[\Lambda_{pm} + (L_{d} - L_{q})I_{d}\right]} = \frac{K}{\frac{\Lambda_{pm}}{L_{d} - L_{q}} + I_{d}}$$
(3.35)

where K is a constant for a given torque. This represents a family of hyperbolas with a vertical asymptote at $I_d = -\frac{\Lambda_{pm}}{(L_d - L_q)}$ and a horizontal asymptote at $I_q = 0$.

Maximum Torque Per Ampere Trajectory

For a given current magnitude $\sqrt{I_d^2 + I_q^2}$, the maximum torque is found where a constant-torque hyperbola is tangent to a current-limit circle. This MTPA trajectory can be derived using different methods, one of them is simply imposing the orthogonality between the torque-hyperbola and the desired segment. In particular it is fundamental to obtain the two angular coefficient and impose that the product is equal to -1. The angular coefficient of the hyperbola is given by:

$$m_{hyp} = \frac{\partial I_q}{\partial I_d} = \frac{I_q(L_q - L_d)}{\Lambda_{pm} + (L_d - L_q)I_d}$$
(3.36)

while the angular coefficient of the segment is $m_{seg} = \frac{I_q}{I_d}$. Since due curves are tangent in a point when the product of their angular coefficient is equal to -1, one can write:

$$m_{seg}m_{hyp} = \frac{I_q(L_q - L_d)}{\Lambda_{pm} + (L_q - L_d)I_d} \frac{I_q}{I_d} = \frac{I_q^2(L_q - L_d)}{I_d[\Lambda_{pm} + I_d(L_d - L_q)]} = -1 \implies \frac{I_q^2(L_q - L_d) + I_d[\Lambda_{pm} + I_d(L_d - L_q)}{I_d[\Lambda_{pm} + I_d(L_d - L_q)]} = 0 \implies I_q = \pm \sqrt{\frac{I_d[\Lambda_{pm} + I_d(L_d - L_q)]}{L_q - L_d}}$$
(3.37)

where the sign \pm depends it the desired torque is positive or negative. If the speed is below Ω_B , the nominal torque is always available and it is possible to obtain the MTPA.

The operational strategy is analogous to the isotropic case but follows these new geometrical contours. Below base speed Ω_B , the motor operates on the MTPA trajectory to produce the required torque. Above base speed, operation changes depending on where the voltage-limit centre lies.

Voltage-Limit Center Outside Current Circle

As already stated in the previous section, below base speed the analysis is identical to the one proposed for the isotropic case, so the working point is obtained following the MTPA trajectory. Similarly to the isotropic scenario, if the speed is greater then the base speed, the voltage limit becomes the

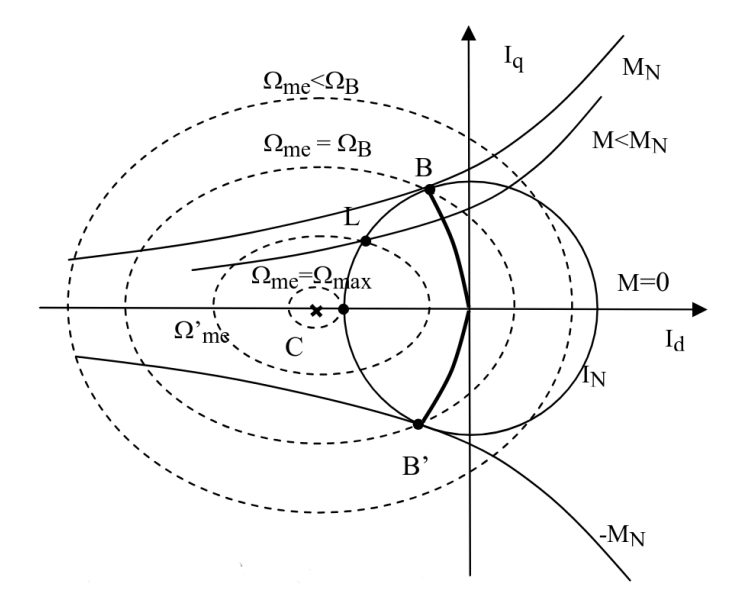


Figure 3.5.3: Operating limits for an anisotropic rotor. The voltage limit is an ellipse, constant-torque contours are hyperbolas, and the MTPA trajectory is a curve inside the current-limit circle [26].

most demanding constrain, forcing the motor to work below the nominal torque, following FW trajectory. Again, the working point is simply given by the intersection of the current-limit circumference and the voltage-limit ellipse. Since the voltage-limit centre lies outside the current circle, there's a maximum speed Ω_{max} , given by imposing $I_d = 0, I_q = I_N$ in equation (3.33):

$$\Omega_{max} = \frac{U_N}{\Lambda_{pm} - L_d I_N} \tag{3.38}$$

Voltage-Limit Center Inside Current Circle

If an wide operating region is required, it is advisable to use motor with a low short circuit current, since, as for the isotropic scenario, there will be not a defined maximum speed. As for the isotropic rotor, the motor will produce the nominal torque until $\Omega_m < \Omega_B$. When that limit is crossed, the motor will be able to increase its velocity by reducing the produced torque thanks to FW strategy. Lastly if the speed surpass Ω_P , the working point is given by the intersection of the voltage limit ellipsis and the torque parabolas. In this scenario the motor work under the MTPV lotus, which corresponds to the curve PP' in figure 3.5.4. To obtain the MTPV trajectory is convenient

to equal the hyperbola and ellipsis angular coefficients:

$$I_{q \ ellipsis} = \pm \sqrt{\left(\frac{U_N}{\Omega_m L_d}\right)^2 - \left(I_d + \frac{\Lambda_{pm}}{L_d}\right)^2}$$

$$m_{ellipsis} = \frac{\partial I_{q \ ellipsis}}{\partial I_d} = \pm \left(\frac{L_d}{I_q L_q}\right)^2 \left(I_d + \frac{\Lambda_{mg}}{L_d}\right)$$

$$m_{hyp} = \frac{\partial I_q}{\partial I_d} = \frac{I_q (L_q - L_d)}{\Lambda_{pm} + (L_d - L_q)I_d}$$

$$I_q = \pm \frac{L_d}{L_q} \sqrt{\frac{-\left(I_d + \frac{\Lambda_{pm}}{L_d}\right) [\Lambda_{pm} + (L_d - L_q)I_d]}{L_q - L_d}}$$
(3.39)

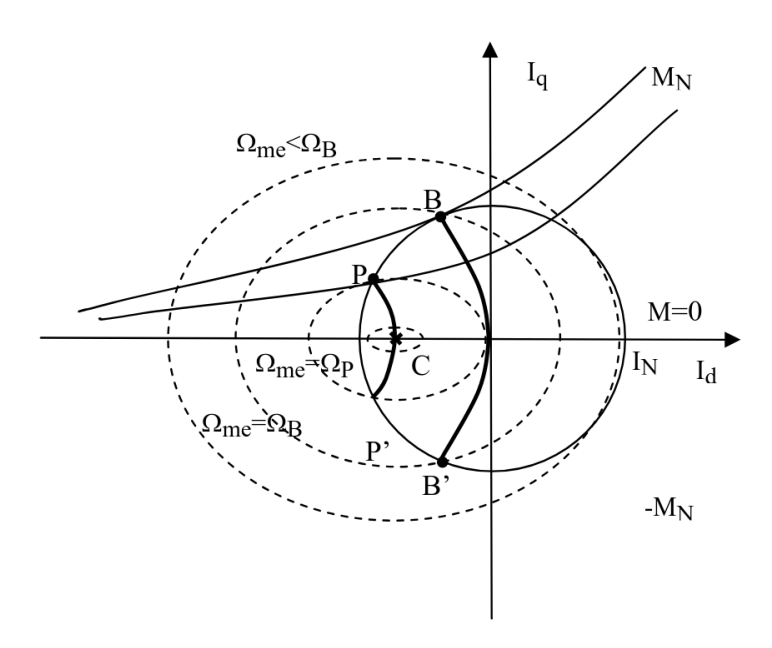


Figure 3.5.4: Operating limits for an anisotropic rotor with low short-circuit current. The curve PP' represent the MTPV trajectory [26].

3.6 Non Ideal Phenomena

3.6.1 Core magnetic saturation

The relationship between magnetic flux density (B) and magnetic flux (H) can be considered linear until a certain threshold is not exceeded. After that saturation effect has to be taken into account. In this scenario the relationship H - B is not linear any more. In normal condition (i.e., unsaturated core) the permeability of the iron core can be considered constant

and it obviously corresponds to the slope of the curve. As the magnetic flux increases, the slope tends to flat out, the permeability decreases and the working point starts to go towards the knee of the curve. After the knee the iron core becomes fully saturated: here increments of the magnetic flux produce little to no growth of the magnetic flux density and the magnetic permeability of the material tends to decrease more and more [2].

Considering the simplified case where no cross saturation effect take place, equations (3.18) become:

$$u_{d} = Ri_{d} + \frac{d\lambda_{d}(i_{d})}{di_{d}} \frac{di_{d}}{dt} - \omega_{e}\lambda_{q}(i_{q}) =$$

$$Ri_{d} + \tilde{L}_{d}(i_{d}) \frac{di_{d}}{dt} - \omega_{e}L_{q}(i_{q})i_{q}$$

$$u_{q} = Ri_{q} + \frac{d\lambda_{q}(i_{q})}{di_{q}} \frac{di_{q}}{dt} + \omega_{e}\lambda_{d}(i_{d}) =$$

$$Ri_{q} + \tilde{L}_{q}(i_{q}) \frac{di_{q}}{dt} + \omega_{e}L_{d}(i_{d})i_{d} + \omega_{e}\Lambda_{pm}$$

$$(3.40)$$

where $\tilde{L}_d(i_d)$ and $\tilde{L}_q(i_q)$ are called differential inductances. Due to the presence of the permanent magnet the flux on the d axis has also the component Λ_{pm} . For this reason the inductances L_d and L_q must be defined as:

$$L_d = \frac{\lambda_d(i_d) - \Lambda_{pm}}{i_d}$$

$$L_q = \frac{\lambda_q(i_q)}{i_q}$$
(3.41)

A more detailed analysis of a PMSM would include other undesired effects such as cross saturation. This phenomena can take place, when the magnetic linkage of a certain axis is affected by the current of the other axis. Due to this effect the latter equations become more complex, since now the fluxes on the d and q axis are both dependent to the currents $i_d - i_q$. In particular they can be expressed as:

$$\begin{split} u_{d} = &Ri_{d} + \frac{\partial \lambda_{d}(i_{d}, i_{q})}{\partial i_{d}} \frac{di_{d}}{dt} + \frac{\partial \lambda_{d}(i_{d}, i_{q})}{\partial i_{q}} \frac{di_{q}}{dt} - \omega_{e} \lambda_{q}(i_{d}, i_{q}) = \\ &Ri_{d} + \tilde{L}_{d}(i_{d}, i_{q}) \frac{di_{d}}{dt} + \tilde{M}_{dq}(i_{d}, i_{q}) \frac{di_{q}}{dt} - \omega_{e} L_{q}(i_{q})i_{q} \\ u_{q} = &Ri_{q} + \frac{\partial \lambda_{q}(i_{d}, i_{q})}{\partial i_{q}} \frac{di_{q}}{dt} + \frac{\partial \lambda_{q}(i_{d}, i_{q})}{\partial i_{d}} \frac{di_{d}}{dt} + \omega_{e} \lambda_{d}(i_{d}) = \\ &Ri_{q} + \tilde{L}_{q}(i_{d}, i_{q}) \frac{di_{q}}{dt} + \tilde{M}_{qd}(i_{d}, i_{q}) \frac{di_{d}}{dt} + \omega_{e} L_{d}(i_{d})i_{d}(t) + \omega_{e} \Lambda_{pm} \end{split}$$

$$(3.42)$$

where $\tilde{M}_{dq} = \tilde{M}_{qd}$ are the differential mutual inductances.

3.6.2 Core Losses

As established in the previous chapter, the ferromagnetic materials in the stator exhibit non-linear magnetic characteristics Since the stator is made up of ferromagnetic material, is of particular interest understand the losses that can arise from these non linear behaviour. The two primary components of these losses are hysteresis losses and eddy current losses, both of which will be detailed in the following sections.

Hysteresis Loss

Chapter 3.6.1 described the phenomenon of magnetic saturation. However, the behaviour of the material as the external magnetic field is removed warrants further explanation. One might assume that the magnetic flux density (B) would simply return to zero, but this is not the case.

Due to a property known as magnetic hysteresis, the flux density does not follow the same path back to zero when the magnetic field strength (H) is reduced. Instead, when H reaches zero, a residual magnetic flux density B_{res} remains, meaning the material behaves temporarily like a permanent magnet. To reduce this residual flux density to zero, a negative magnetic field strength, known as the coercive field H_c , must be applied. A symmetric phenomenon occurs when the material is magnetized in the negative direction, forming a closed loop known as the hysteresis loop.

During the operation of a PMSM, the alternating stator currents subject the stator core to a continuously reversing magnetic field. This forces the ferromagnetic material to cycle around its hysteresis loop continuously. The energy required to navigate this loop during each cycle is dissipated as heat, which is defined as the hysteresis loss. This loss is directly proportional to the area enclosed by the hysteresis loop [2].

Eddy Currents Loss

Eddy currents are a direct consequence of Faraday's Law of Induction (see Chapter 2.2.4). The time-varying magnetic field produced by the stator currents and the rotating rotor induces electromotive forces within the conductive ferromagnetic material of the stator core. According to Lenz's Law, these induced voltages drive circulating currents, known as "eddy currents," which flow in closed loops within the material.

A portion of the electrical energy supplied to the motor is dissipated as Joule heating due to the resistance of the core material. This represents a direct conversion of useful energy into waste heat, reducing the motor's overall efficiency.

The power dissipated by eddy currents is proportional to the square of the induced EMF. Since the induced EMF is itself proportional to the frequency of the magnetic flux, eddy current losses increase with the square of

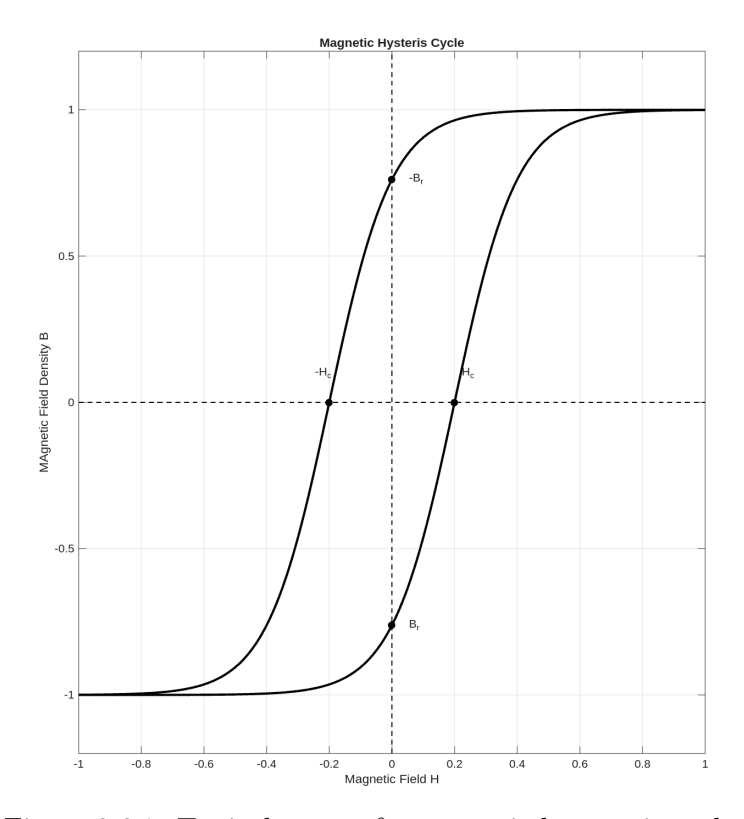


Figure 3.6.1: Typical curve of a magnetic hysteresis cycle,

the frequency of the magnetic field alternation. This makes them a particularly dominant loss mechanism at high speeds.

To mitigate this, the stator core is not constructed from a single solid piece of steel. Instead, it is composed of many thin laminations, electrically insulated from one another by a thin coating or oxide layer. This design drastically increases the electrical resistance along the path of the potential eddy currents, confining them to smaller, individual loops within each lamination and thereby reducing their magnitude and the associated energy loss [2].

Chapter 4

Field Oriented Control System

In the following chapter, focus will be put on understanding the principles of field oriented control. Given the basic concepts presented in chapter 3.2.1, it is now possible to dig deeper into the fundamental equations and parameters of interest.

4.1 System Block Diagram

As established in Chapter 3.2.1, the implementation of Field Oriented Control requires two fundamental coordinate transformations: the Clarke transformation, which projects a three-phase system onto a stationary two-axis orthogonal reference frame $(\alpha - \beta)$, and the Park transformation, which converts these stationary coordinates into a synchronous rotating reference frame (d-q) aligned with the rotor flux. These transformations enable decoupled control of torque and flux-producing current components, analogous to DC motor control.

Figure 4.1.1 illustrates a simplified FOC system architecture, highlighting the essential components including coordinate transformations, current controllers, and modulation stages.

4.2 Controller Fundamentals

Proportional Integral controllers are widely employed in control systems due to their simplicity and effectiveness in improving the overall system response. It is crucial to be able to choose properly the parameters of the PI controller in order to avoid introducing instability in the system. To do so is necessary to consider the PLANT transfer function.

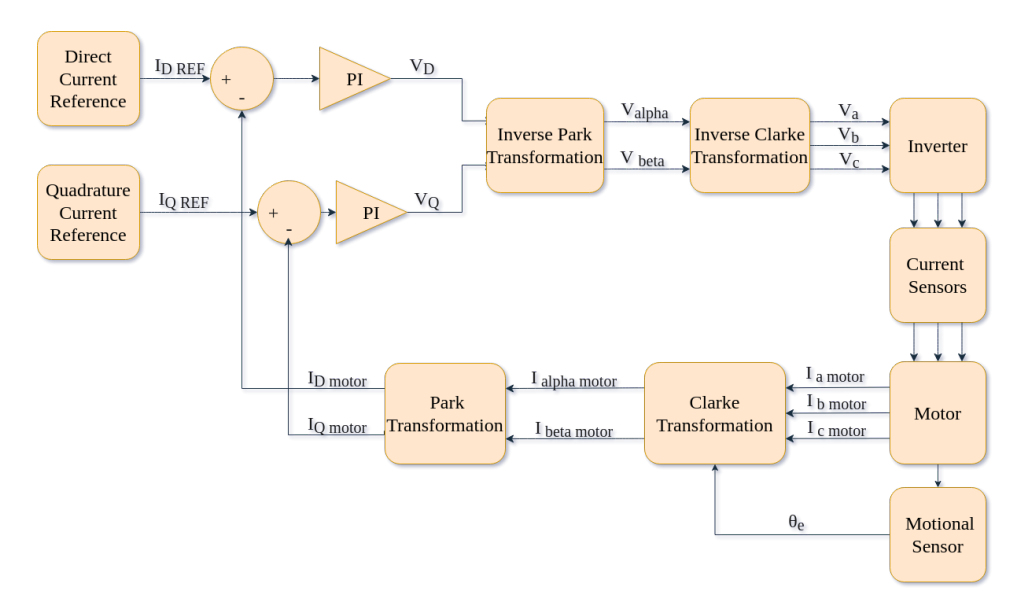


Figure 4.1.1: Schematic diagram of a field oriented control system.

4.2.1 Motor Plant Transfer Function

Recalling the voltage equations derived in Section 3.3 and applying Laplace transformation, the quadrature-axis voltage equation becomes:

$$U_q(s) = R_s I_q(s) + s L_q I_q(s) + \Omega L_d I_d(s) + \Omega \Lambda_{mq}$$

$$\tag{4.1}$$

Assuming initial that the BEMF will be later compensated, the system simplifies to a first-order transfer function:

$$G_{mot}(s) = \frac{I_q(s)}{U_q(s)} = \frac{1}{R_s + sL_q} = \frac{1}{R_s(1 + s\tau_e)}$$
 (4.2)

where $\tau_e = \frac{L_q}{R_s}$ represents the electrical time constant of the motor.

4.2.2 PI Controller Transfer F unction

The parallel-form PI controller transfer function is given by:

$$PI(s) = K_P + \frac{K_I}{s} = \frac{sK_P + K_I}{s} = K_I \frac{1 + s\tau_I}{s}$$
 (4.3)

where $\tau_I = \frac{K_P}{K_I}$ denotes the integral time constant, which determines the controller's zero location.

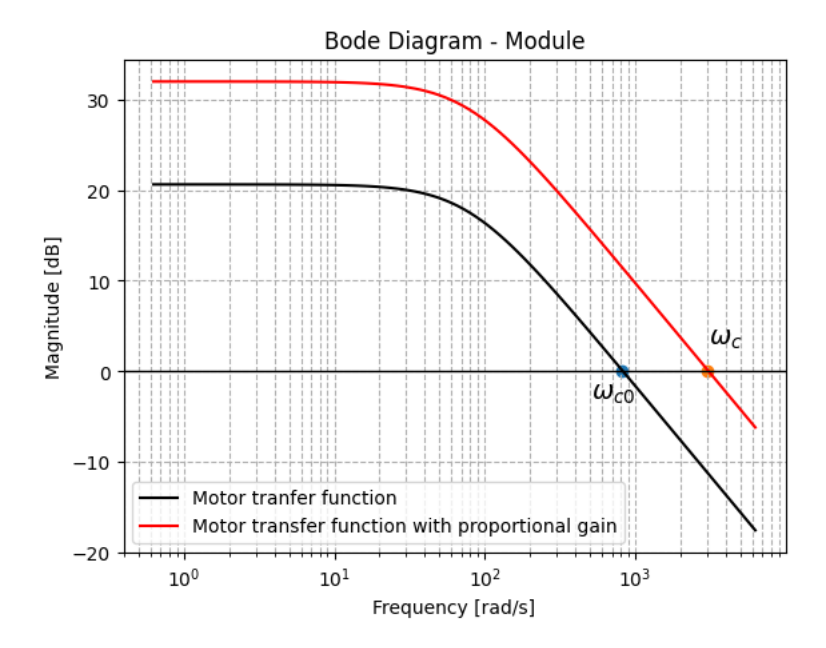


Figure 4.2.1: Bode diagram of motor transfer function with (red) and without (black) proportional correction.

4.2.3 Open Loop System Analysis

The combined open-loop transfer function of the plant and controller is:

$$G_{ol}(s) = G_{mot}(s)PI(s) = \frac{1}{R_s(1+s\tau_e)}K_I \frac{1+s\tau_I}{s} = \frac{K_I}{R_s} \frac{1+s\tau_I}{s(1+s\tau_e)}$$
(4.4)

This formulation provides the foundation for systematic controller design using frequency response methods, where appropriate selection of K_I and K_P ensures adequate stability margins and transient performance. Through a proper selection of K_I and K_P , it is possible to simplify the closed-loop system to a first order system.

The proportional gain K_P can be determined by specifying the desired crossover frequency ω_c . Since the transfer function has only one pole, so its slope (using log-log scale) is unitary, the value of K_P can be simply expressed as:

$$K_P = \frac{\omega_c}{\omega_{c0}} \tag{4.5}$$

Here, ω_{c0} can be determined by observing again that the slope of the Bode diagram after the motor pole is unitary. Using logarithmic properties, this yields:

$$\log \frac{1}{Rs} - \log 1 = \log \omega_{c0} - \log \frac{1}{\tau_e} \to \log \omega_{c0} = \log \frac{1}{R_s \tau_e} = \log \frac{1}{L_a} \quad (4.6)$$

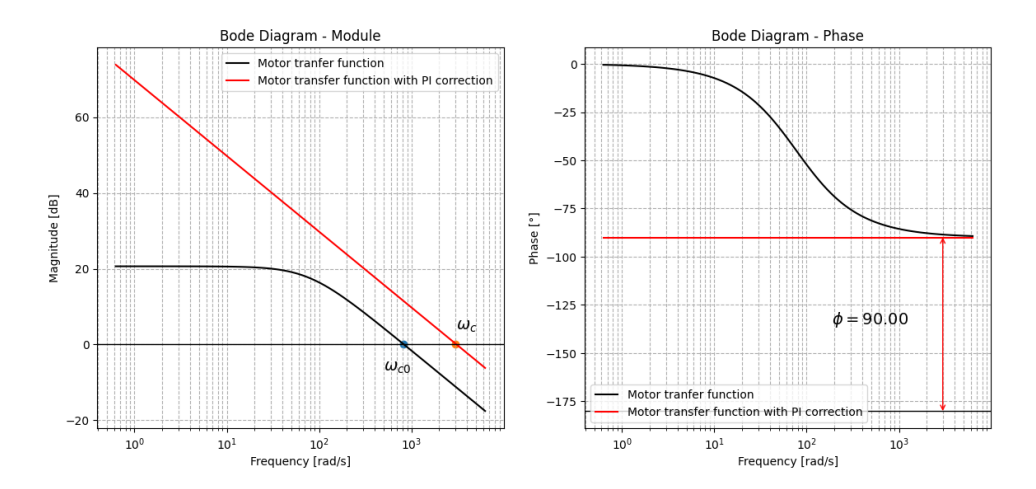


Figure 4.2.2: Bode diagram of the module and phase of the motor transfer function with the PI correction.

The impact of the proportional gain on the system response can be observed in the Bode diagram shown in Figure 4.2.1.

Since the frequency ω_c for which the open loop system will have unitary gain is fixed, the last parameter K_I can be chosen such that the motor pole and the PI controller zero cancel each other. This results in an effective first-order system with a phase margin of 90°, as illustrated in Figure 4.2.2.

The integral gain is then computed as:

$$K_I = \omega_c R_s$$

$$\tau_I = \frac{L}{R_s} \to \frac{K_P}{K_I} = \frac{L}{R_s} \to K_P = \frac{L}{R_s} \omega_c R_s = L\omega_c$$

$$\tag{4.7}$$

It important to note that even though positioning the PI zero in correspondence to ω_c would be ideal, since it would increase the static gain of the open loop system, reducing the steady state error, but this would lead to a reduce margin phase. In fact, in figure it is clear that in that case the phase margin would be 54°, making the system less stable.

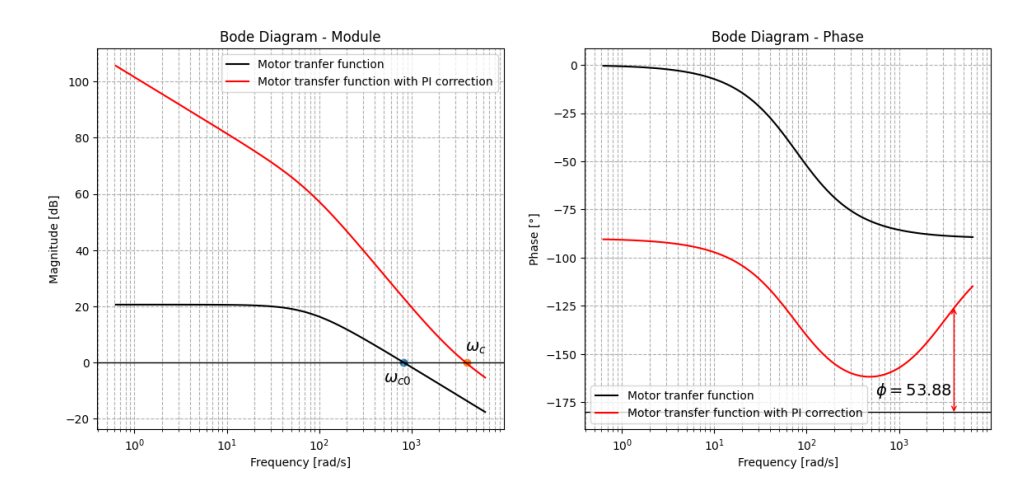


Figure 4.2.3: Bode diagram of open loop system with PI zero place in correspondence of ω_c .

Chapter 5

Finite Element Analysis and Frozen Permeability

5.1 Finite Element Analysis

Finite Element Analysis (FEA) is a numerical technique widely employed to solve complex engineering and physical problems that are difficult or impossible to address analytically. The fundamental concept behind FEA is the discretization of the physical domain into a finite number of smaller, simpler subdomains called elements. These elements are interconnected at specific points known as nodes. Within each element, the governing equations, typically partial differential equations derived from physical laws are approximated by simpler, piecewise functions [28].

By assembling the contributions of all elements, FEA transforms the continuous field problem into a discrete system of algebraic equations that can be efficiently solved using computational methods. This discretization process enables engineers and researchers to analyse structures, fields, and materials of arbitrary shape and complexity, including non-linear, anisotropic, or inhomogeneous materials.

In the context of electrical machines, FEA plays a critical role in accurately predicting electromagnetic quantities such as magnetic flux distribution, torque, losses, and inductances. It allows for the evaluation of non-linear magnetic behaviour due to saturation, as well as the effects of geometry and material properties. Therefore, FEA provides an indispensable tool for both design optimization and performance validation of electric machines and other electromagnetic devices.

5.2 Frozen Permeability Method

During the normal operation of a PMSM, the magnetic flux within the air gap and stator teeth is generated by two primary sources: the permanent magnets mounted on the rotor and the armature currents flowing through the stator windings. Accurately modelling the resulting electromagnetic fields requires a detailed understanding of the magnetic material's permeability, which varies non-linearly with the magnetic field intensity due to saturation effects.

To correctly determine the inductance values L_d and L_q , as well as the permanent magnet flux linkage λ_{PM} , it is necessary to consider the magnetic behaviour of the machine over a wide range of operating points. This includes various combinations of direct and quadrature axis current components, I_d and I_q . Traditional FEA can capture this behaviour, but it can be computationally expensive and may lead to inconsistent inductance values if the non-linearities are not carefully managed [27].

The Frozen Permeability method offers an effective approach to address these challenges. In this method, a non-linear magnetic analysis is first performed at a specific operating point to obtain the spatial distribution of magnetic permeability throughout the machine. Once this distribution is computed, the permeability values are "frozen", meaning they are kept constant for subsequent linear magnetic analyses. This simplification allows the effects of different excitation sources, such as the stator current and the permanent magnet, to be studied independently by setting their respective magnetomotive forces to zero in different simulations [27].

Using the FP method, it becomes possible to accurately extract the contributions of the d- and q-axis flux linkages and to compute L_d , L_q , and λ_{PM} under varying current conditions. This method ensures better consistency and physical relevance compared to classic FEA approaches, where non-linear interactions can cause large deviations in the calculated inductance values [27]. Consequently, the FP method is widely used in advanced electric machine modelling and control strategy development, particularly in the implementation of Maximum Torque per Ampere, Maximum Torque per Voltage, and field-weakening operations. [27].

5.2.1 Inductance Computation

The maps of the inductance values L_d and L_q were obtained using the Flux-Partial (FP) method. Figures 5.2.1 and 5.2.2 show the resulting distributions of L_d and L_q as functions of the stator currents I_d and I_q . These values were then used to populate the corresponding lookup tables (LUTs), enabling accurate modeling of the current required to generate the desired torque. Furthermore, the computed inductance values were essential for the correct estimation of the back electromotive forces (BEMFs) and for the calculation of the coefficients used in the PID controllers within the current control loop.

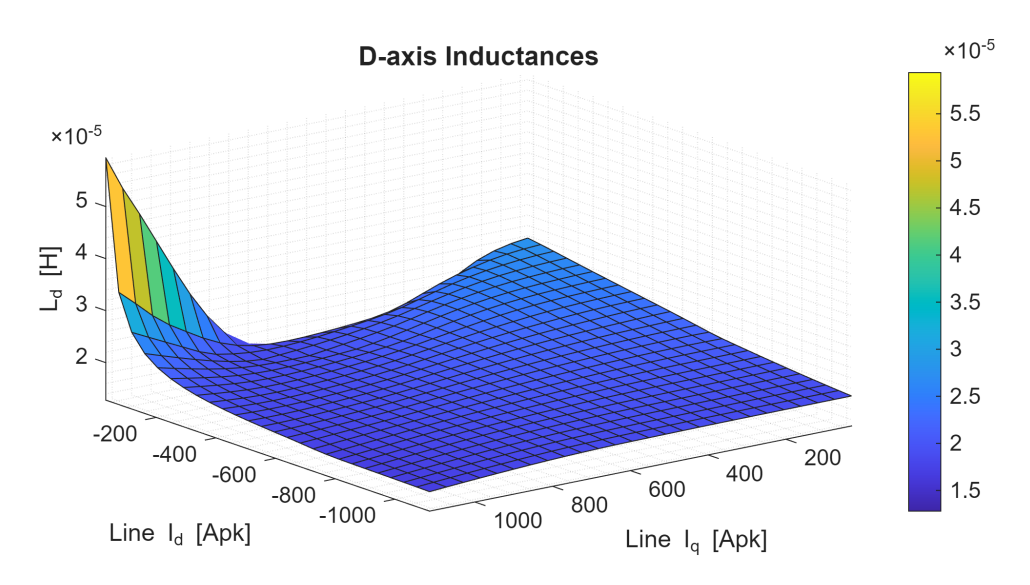


Figure 5.2.1: Map of the d-axis inductance L_d as a function of the currents I_d and I_q .

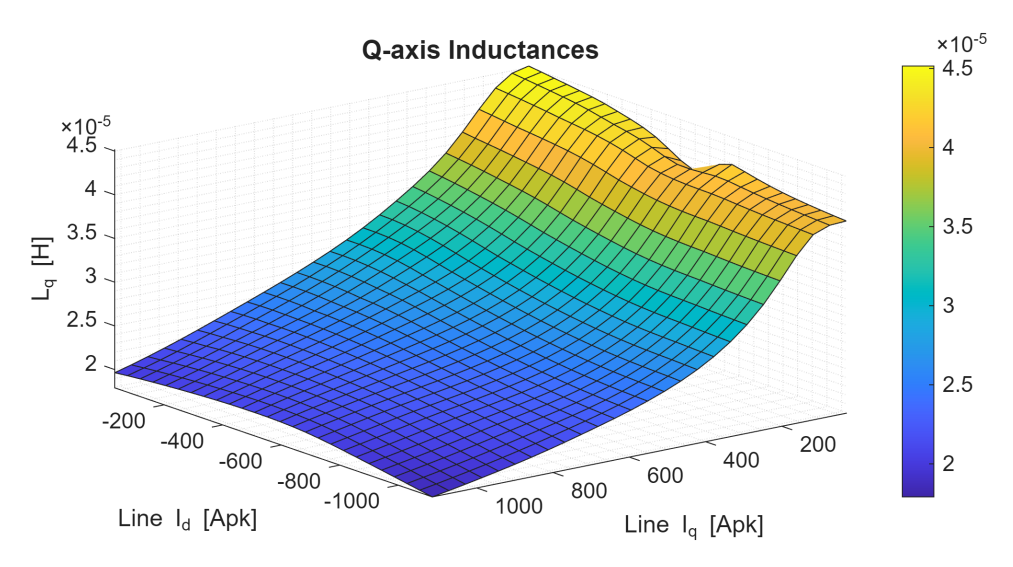


Figure 5.2.2: Map of the q-axis inductance L_q as a function of the currents I_d and I_q .

5.2.2 Permanent Magnetic Flux

Similarly to the inductance computation, the map of the permanent magnet flux linkage was obtained using the FP method, as shown in Figure 5.2.3. This map was used to populate the corresponding LUT, allowing the development of a realistic nonlinear model of the motor that accurately represents the variation of the magnetic flux with the stator currents.

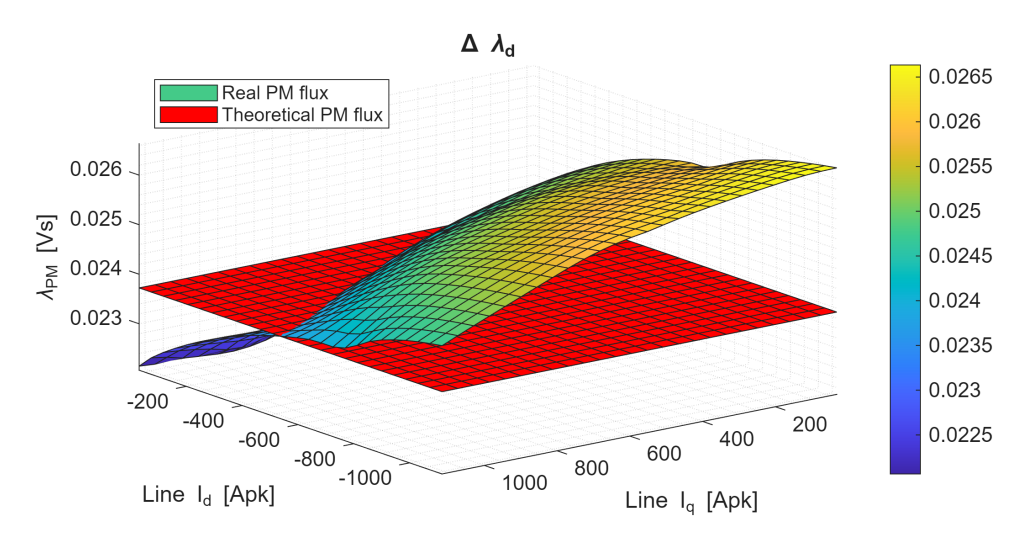


Figure 5.2.3: Map of the permanent magnet flux linkage as a function of the stator currents I_d and I_q .

Chapter 6

Simulink Non Linear Motor Model

Since the objective is to create a non-linear model of the motor, the simplifications introduced in Chapter 3.3.1 can no longer be applied. In particular, the inductances L_d and Lq can no longer be assumed constant with respect to the stator currents i_d and i_q . Their values vary significantly with current due to magnetic saturation and cross-coupling effects between the d and q axes.

Similarly, the magnetic flux generated by the permanent magnets along the d-axis cannot be considered constant. In real machines, the effective flux linkage produced by the magnets depends on the operating point of the motor, especially on the stator current components i_d and i_q , which influence the magnetic field distribution within the rotor and stator.

To accurately capture these non-linear dependencies, multiple look-up tables will be implemented. These tables will store data obtained through 2D-FEA using frozen permeability method relating current, flux linkage, and inductance, ensuring that the non-linearities of the motor are faithfully represented in the model.

Furthermore, iron losses must be included to achieve an accurate dynamic representation of the system. Figure 6.0.1 illustrates the principle scheme of the developed system. The system receives a reference speed ω_{ref} as input, which is fed to the speed control loop to generate the required current for driving the motor. These reference currents are then processed by the current control loop, which produces the corresponding voltage commands for the inverter. The resulting three-phase voltages are applied to the motor, generating an electromagnetic torque T_{em} that drives the vehicle at a mechanical speed ω_m .

Both the motor speed and phase currents are continuously monitored to close the control loops. Specifically, the speed loop compares the reference speed with the actual speed and adjusts the current commands accordingly,

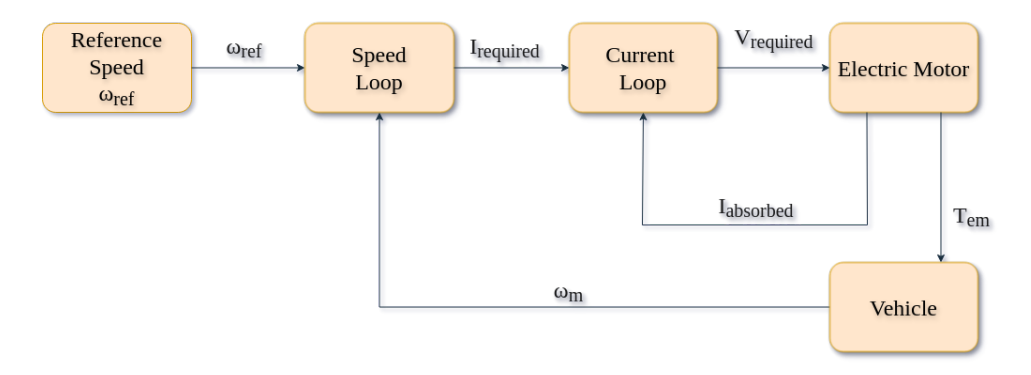


Figure 6.0.1: Principle scheme of the non linear model system.

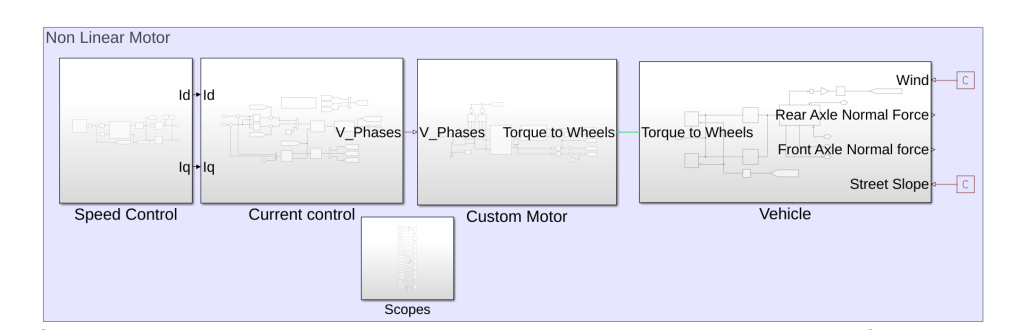


Figure 6.0.2: Complete simulink system.

while the current loop compares the reference currents with the measured currents and adjusts the applied voltages to minimize the error.

The overall structure of the complete system model is shown in Figure 6.0.2.

In the following chapter, each component of the Simulink model will be discussed in detail.

6.1 Custom Motor Model

The primary objective is to construct a Simulink model capable of receiving a three-phase voltage input and producing, as output, the electromagnetic torque generated by the motor. In the following sections, the procedure for generating the appropriate voltage signals to drive the motor will be described, together with the design of a control system capable of interacting with the non-linear model.

Figure 6.1.1 shows the overall motor model, which is composed of several interconnected subsystems.

From left to right, the system consists of three voltage-controlled voltage source generators, which, for simplicity, emulate the operation of an inverter.

The voltages used to drive these generators are provided by the current control loop, which will be discussed in a later section.

Next, two watt-meters are used to measure the power absorbed by the motor. Although the system operates with three phases, the two-watt-meter method (also known as the Aron method) allows accurate measurement of the absorbed power without the need for three separate watt-meters.

The generated voltages are then applied to the custom IPMSM model, which computes the corresponding electromechanical torque. The model provides two output ports: one delivering the generated torque, and the other providing a mechanical reference signal.

A rotational sensor is employed to measure the rotor angular velocity and position, quantities that are fundamental for the implementation of the control system. A custom block is also included to emulate a gearbox, whose operation will be explained in detail in a subsequent section.

A dot product block is used to compute the mechanical output power, given by the product of the torque at the wheels and the vehicle speed. Two gain blocks are used to convert the rotor's mechanical speed and angle into their electrical equivalents by multiplying these quantities by the number of pole pairs, p_p .

Finally, *Goto* blocks are included to simplify the interconnections with other subsystems.

Each of the aforementioned subsystems will now be analysed in detail.

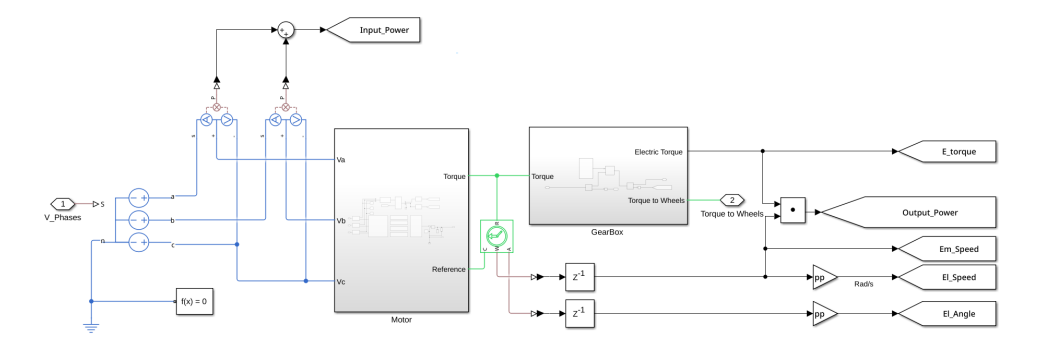


Figure 6.1.1: Simulink model of the IPMSM.

6.1.1 Custom IPMSM Model

To accurately model the IPMSM, several interconnected subsystems have been developed within the simulation environment, as can be seen in Figure 6.1.2.

From left to right in the model, three current sensors are employed to measure the phase currents absorbed by the motor. These measurements are used both for comparison with other motor models and for the computation of the i_d and i_g current components.

The Clarke Transform and Clarke-to-Park blocks are implemented to convert the three-phase stationary currents into the two-axis synchronous reference frame components, i_d and i_q . These transformed currents are subsequently used in the current control loop to generate the optimal three-phase voltage references.

A custom block, named *Tri-phase*, has been designed to accurately reproduce the electrical behaviour of the IPMSM. Specifically, an equivalent star-connected three-phase system is implemented, taking into account the BEMF, stator resistance, iron losses, and the voltages induced by both self and mutual inductances.

The *Inductance Process* block computes the instantaneous values of the d- and q-axis inductances, L_d and L_q , as well as the complete inductance matrix and its time derivative. This enables an accurate representation of the non-linear magnetic characteristics of the machine.

The *Iron Losses* block determines the equivalent resistance used within the *Tri-phase* subsystem to model iron losses consistently with the electromagnetic behaviour of the stator core.

The *BEMF Generator* block calculates the voltage waveform driving the three voltage sources that emulate the per-phase back-EMF. In parallel, it also computes the magnetic flux produced by the permanent magnets as a function of the stator currents i_d and i_q .

Finally, the *Torque Production* block provides both the electromechanical torque generated by the motor and a mechanical reference output signal used in the overall system dynamics.

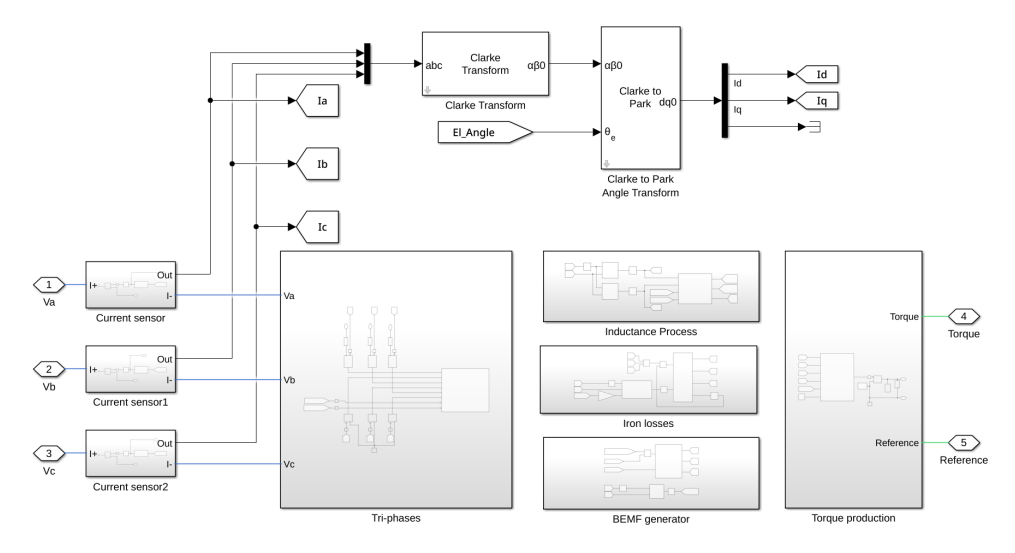


Figure 6.1.2: System used to model the custom IPMSM.

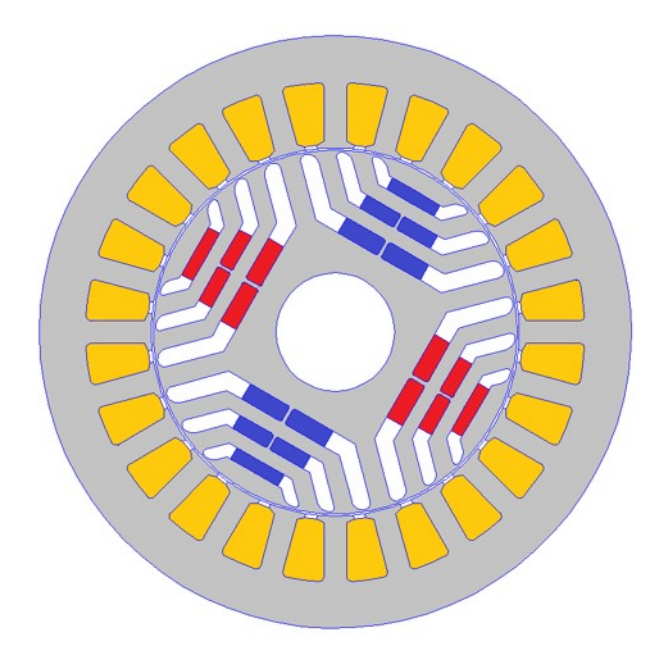


Figure 6.1.3: Reference motor used.

6.1.2 Tri-phase Subsystem

The model of the tri-phase subsystem must account for the various loss mechanisms that occur in an electric motor.

First, the Joule losses are represented by the *Line Resistance* component, which models the series resistance of each phase winding.

Next, to capture the *iron losses*, a dedicated three-dimensional lookup table is employed. This table provides the equivalent resistance as a function of the stator currents and the rotor speed, thereby accounting for the non-linear nature of these losses. Given the total iron losses P_{Fe} , and assuming sinusoidal phase currents, the equivalent resistance per phase can be expressed using Ohm's law as:

$$R_{Fe} = \frac{P_{Fe}}{3I_{\text{RMS}}^2} = \frac{P_{Fe}}{6I_{\text{Peak}}^2}$$
 (6.1)

To model the voltage drop associated with both self and mutual inductances, a custom Simscape block has been developed. Since the inductances are not constant, it is necessary to compute not only the time derivatives of the phase currents but also those of the inductance matrix. The developed block takes as input the complete inductance matrix of the motor and its time derivatives, and computes the instantaneous voltage according to:

$$V_{a} = L_{aa} \frac{di_{a}}{dt} + i_{a} \frac{dL_{aa}}{dt} + M_{ab} \frac{di_{b}}{dt} + i_{b} \frac{dM_{ab}}{dt} + M_{ac} \frac{di_{c}}{dt} + i_{c} \frac{dM_{ac}}{dt}$$
 (6.2)

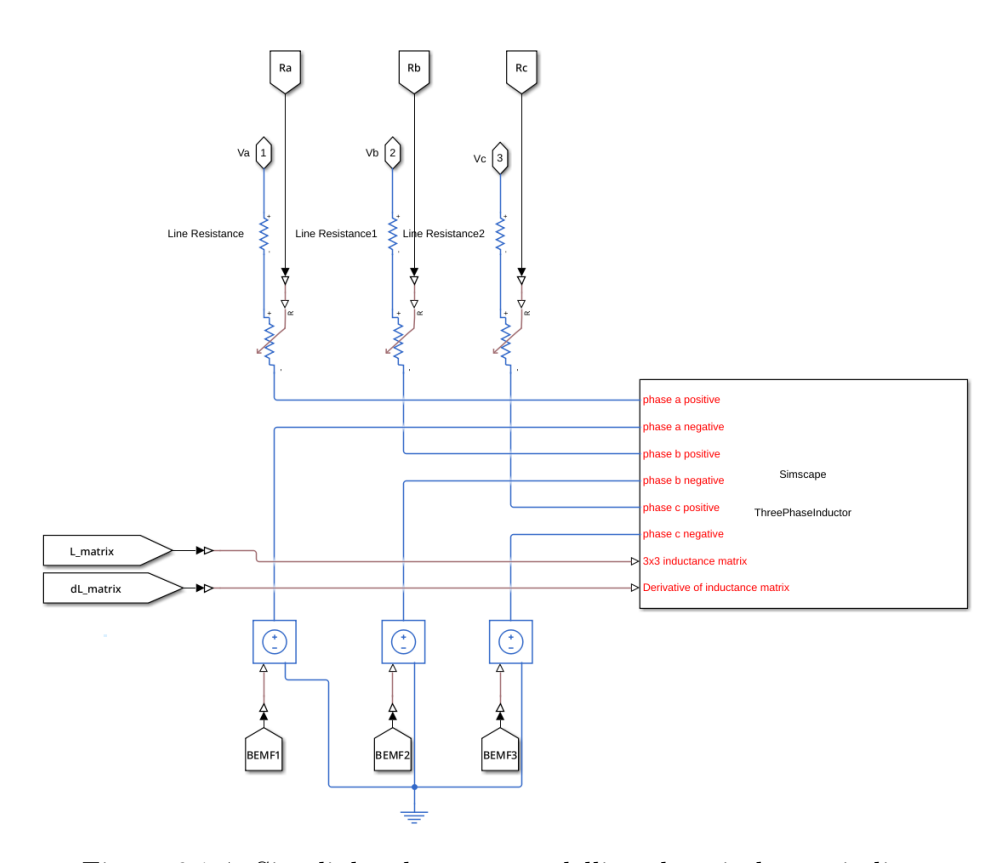


Figure 6.1.4: Simulink subsystem modelling the tri-phase windings.

This voltage is applied to each corresponding phase, thereby emulating the behaviour of a variable inductor.

Finally, three voltage-controlled voltage sources are included to model the back electromotive force, which arises from the variation of magnetic flux generated by the permanent magnets as the rotor moves. This element ensures that the energy conversion between the electrical and mechanical domains is correctly represented in the simulation. The driving voltage for each phase is provided by a dedicated subsystem, which will be analysed in the following section.

6.1.3 Current Measurement

Accurate measurement of the motor currents is essential for evaluating and controlling both the electrical and mechanical variables of the machine. In particular, the instantaneous absorbed currents i_d and i_q , together with the three-phase currents i_a , i_b , and i_c , provide critical information about the motor's electromagnetic state. These quantities are fundamental for the implementation of advanced control strategies such as Field-Oriented Control (FOC), which will be discussed in a subsequent section.

The three-phase stator currents i_a , i_b , and i_c are measured using current sensors connected in series with each motor phase. To prevent the occurrence of algebraic loops during simulation, a Delay block is inserted in each phase path. This measure ensures numerical stability within Simulink, as algebraic loops arise when the output of a block is directly fed back to its input without a time delay, causing ambiguity in determining signal values at each simulation step. The introduction of delay elements allows Simulink to compute each time step using well-defined data, ensuring a stable and physically consistent simulation. Consequently, multiple Delay blocks are used throughout the model for this purpose.

To minimize measurement noise and remove unwanted high-frequency components, the current signals are filtered through a low-pass filter. The filtered outputs are not used for further computations but are intended solely to provide smoother waveforms for visualization in the *Scope* blocks.

Once the three-phase currents are acquired, they are transformed into the two-phase stationary reference frame $(\alpha-\beta)$ using the Clarke transformation. This transformation reduces the three-phase system to an equivalent two-axis representation without any loss of information, thereby simplifying the subsequent analysis and control operations. Following this, the Park transformation is applied to convert the stationary reference frame into the rotating reference frame (d-q), which rotates synchronously with the rotor's magnetic field. This step aligns the reference frame with the rotor flux, greatly simplifying torque and flux control.

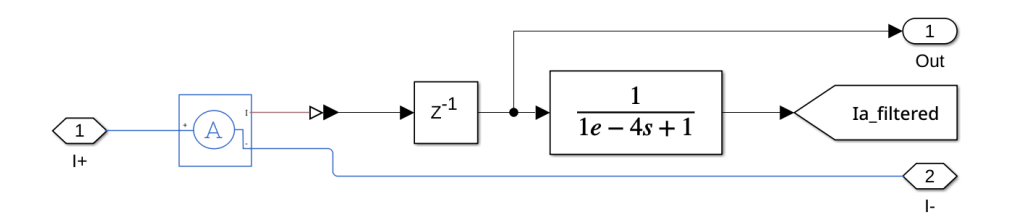


Figure 6.1.5: Simulink subsystem used to measure the phase currents.

6.1.4 Inductance Computation

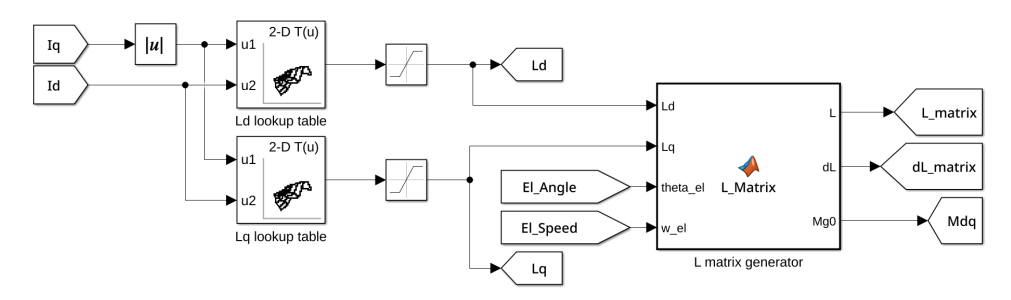


Figure 6.1.6: Simulink subsystem computing the inductance values L_d , L_q , and the inductance matrix L with its time derivative.

The inductance computation subsystem enables the evaluation of the direct and quadrature-axis inductances, L_d and L_q , as functions of the corresponding current components i_d and i_q absorbed by the motor. These inductances are stored in two independent lookup tables, allowing the model to capture the non-linear magnetic behaviour of the machine. Consequently, the variation of inductance with current is accurately represented, ensuring a realistic reproduction of the electromagnetic characteristics of the system.

In this model, the Simulink 2-D Lookup Table block receives i_d and i_q as inputs and returns the corresponding inductance value. A linear interpolation method is employed to guarantee a smooth variation of inductance with respect to the stator currents. An absolute value operator is added to prevent non-physical results during regenerative braking. During this operating mode, the i_q current becomes negative, and without taking the absolute value, the lookup table could return negative inductance values, which have no physical meaning. Furthermore, two saturation blocks are used to constrain the inductance values within predefined limits, preventing unrealistic behaviour when the stator currents exceed the expected operating range.

A dedicated *MATLAB Function* block is subsequently used to compute the inductance matrix and its time derivative. These quantities are provided to the custom Simscape block responsible for calculating the voltage drop across the stator windings.

First, two intermediate quantities, L_{g0} and L_{g2} , are evaluated. These represent, respectively, the synchronous inductance component and the component associated with rotor anisotropy, and are given by [29]:

$$L_{g0} = \frac{L_d + L_q}{3}$$

$$L_{g2} = \frac{L_d - L_q}{3}$$
(6.3)

The inductance matrix L is then expressed as:

$$L = \begin{bmatrix} L_{aa} & M_{ab} & M_{ac} \\ M_{ab} & L_{bb} & M_{bc} \\ M_{ac} & M_{bc} & L_{cc} \end{bmatrix},$$

where the self-inductances of each phase are defined as:

$$L_{aa} = L_{q0} + L_{q2}\cos(2\theta_{el}) \tag{6.4}$$

$$L_{bb} = L_{q0} + L_{q2}\cos(2(\theta_{el} - \frac{2\pi}{3})) \tag{6.5}$$

$$L_{cc} = L_{g0} + L_{g2} \cos\left(2(\theta_{el} + \frac{2\pi}{3})\right) \tag{6.6}$$

and the mutual inductances are given by:

$$M_{ab} = M_{g0} + L_{g2} \cos\left(2(\theta_{el} + \frac{2\pi}{3})\right) \tag{6.7}$$

$$M_{ac} = M_{g0} + L_{g2} \cos\left(2(\theta_{el} - \frac{2\pi}{3})\right) \tag{6.8}$$

$$M_{bc} = M_{a0} + L_{a2}\cos(2\theta_{el}) \tag{6.9}$$

where $M_{g0} = -\frac{L_{g0}}{2}$ represents the average mutual inductance component. Finally, the time derivative of the inductance matrix can be expressed as:

$$\dot{L} = -2\,\omega_{el}\,L_{g2} \begin{bmatrix} \sin(2\theta_{el}) & \sin(2(\theta_{el} + \frac{2\pi}{3})) & \sin(2(\theta_{el} - \frac{2\pi}{3})) \\ \sin(2(\theta_{el} + \frac{2\pi}{3})) & \sin(2(\theta_{el} - \frac{2\pi}{3})) & \sin(2\theta_{el}) \\ \sin(2(\theta_{el} - \frac{2\pi}{3})) & \sin(2\theta_{el}) & \sin(2(\theta_{el} + \frac{2\pi}{3})) \end{bmatrix}.$$

This formulation ensures that both the inductance matrix and its rate of change are dynamically linked to the electrical rotor position θ_{el} and speed ω_{el} , thus faithfully reproducing the electromagnetic coupling between the machine's phases.

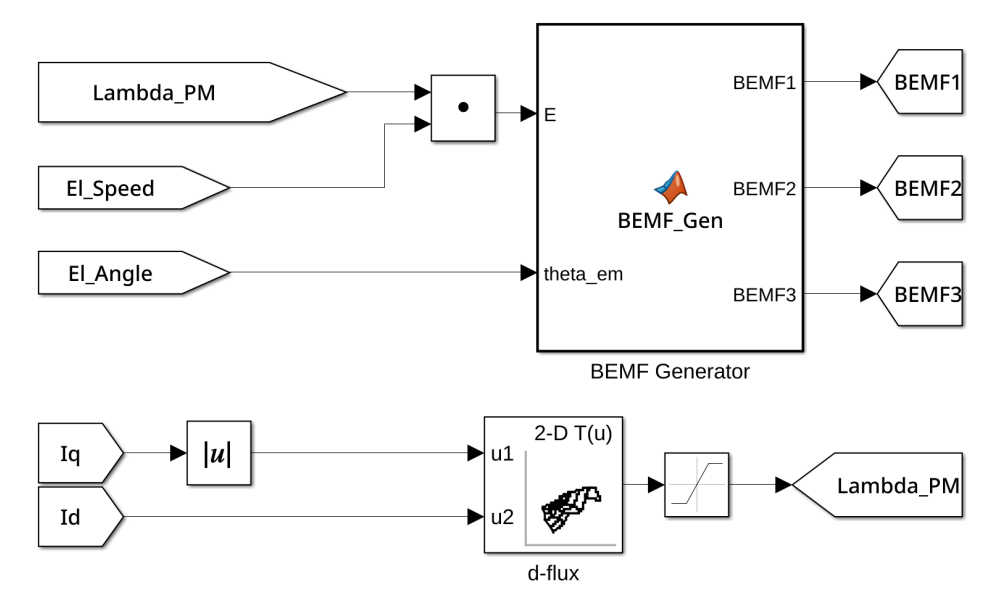


Figure 6.1.7: Simulink subsystem which computes the value of BEMF for each phase.

6.1.5 BEMF and Flux Computation

The back electromotive force represents the voltage induced in each stator winding by the rotating magnetic field generated by the permanent magnets of the rotor. An accurate estimation of the BEMF per phase is crucial for the correct operation of control field-oriented control and for ensuring realistic simulation results in dynamic motor models.

To correctly compute the BEMF, it is essential to determine the permanent magnet flux linkage for each operating condition. Since λ_{PM} varies as a function of the stator currents i_d and i_q , a two-dimensional lookup table was employed to map the relationship between the PM flux linkage and these current components, as can be seen in Figure 6.1.7. The lookup table was populated using results obtained from 2D FEA using frozen permeability method, ensuring high accuracy in the representation of the motor's magnetic characteristics.

Once the PM flux linkage values were obtained, a dedicated MATLAB function block was used to calculate the instantaneous BEMF values for the three motor phases. These were computed using the relationship expressed in (3.15). The resulting three-phase BEMF signals are subsequently applied to drive the corresponding voltage sources in the simulation model, thereby enabling realistic emulation of the motor's electromagnetic behaviour under various operating conditions.

6.1.6 Iron Losses Computation

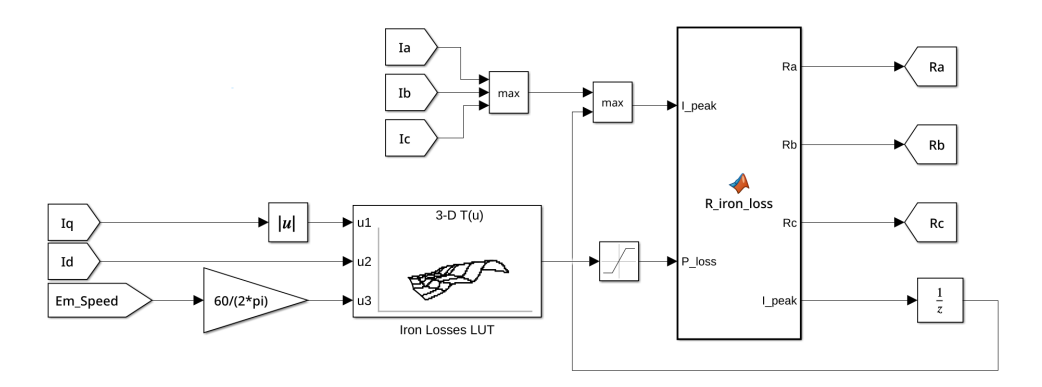


Figure 6.1.8: Simulink subsystem used to compute the equivalent series resistance for modelling iron losses.

Iron losses mainly originate from hysteresis and eddy current effects occurring within the stator core. These losses are inherently non-linear and depend on several factors, including the magnetic flux density, excitation frequency, and operating conditions of the machine. Due to their complex nature, direct analytical modelling of iron losses is generally impractical, particularly when targeting real-time simulation or control-oriented applications.

A practical alternative consists in representing the iron losses through an equivalent series resistance that captures the power dissipated in the magnetic material. In this model, a three-dimensional lookup table is implemented to define the equivalent resistance R_{Fe} as a function of the i_d and i_q current components, and the rotor speed ω_m , expressed in revolutions per minute (rpm). The gain block placed after the Em_Speed Goto block converts the rotor speed to the appropriate unit for this purpose.

Analogously to the other subsystems, *Abs* and *Saturation* blocks are introduced to ensure physically meaningful results. Since the phase currents are sinusoidal, it is necessary to determine either their peak or RMS value for accurate computation. To achieve this, two *Max* blocks and a *Delay* block are used to dynamically track the maximum current value flowing in each phase during operation.

By incorporating this equivalent resistance into the model, the subsystem accurately reproduces the additional voltage drop and power dissipation associated with magnetic losses in the stator core. This approach significantly enhances the fidelity of the electrical model, allowing for a more realistic simulation of the machine's electromagnetic behaviour.

6.1.7 Torque Generation

To generate the electromagnetic torque within the motor model, a dedicated MATLAB Function block has been implemented. This block computes the instantaneous torque using the analytical formulation given in (3.22). Unlike simplified models, where the direct and quadrature axis inductances (L_d and L_q), as well as the flux linkage produced by the permanent magnets (λ_{pm}), are considered constant, this implementation accounts for their non-linear dependence on the current components i_d and i_q . This allows for a more realistic representation of the torque production mechanism under varying operating conditions.

The torque signal computed by the *MATLAB* block is then converted into a mechanical input using an *Ideal Torque Source* block. Subsequently, the *Inertia* and *Rotational Damper* blocks are employed to model the mechanical dynamics of the motor. The *Inertia* block introduces the concept of rotational mass, enabling the computation of angular acceleration according to (2.19). While inertia primarily influences transient conditions such as acceleration and deceleration, damping has a continuous effect throughout the operation, opposing motion and dissipating energy.

In general, the relationship between torque and angular velocity due to damping can be expressed as [30]:

$$T = D(\omega_R - \omega_C) \tag{6.10}$$

where D is the damping coefficient with units of $[\frac{N*m*s}{rad}]$, ω_R is the rotational speed of the rotor, and ω_C is the reference mechanical speed. Since terminal C is connected to the mechanical reference, the equation simplifies to:

$$\omega_R = \frac{T}{D},\tag{6.11}$$

where T represents the applied torque.

6.2 Current Control Loop

To correctly generate the control signals required to drive the motor, a current control loop is essential. The main objective of this loop is to regulate the three-phase voltages such that the desired torque is produced, ensuring efficient operation of the motor under varying load and speed conditions.

To achieve this, a FOC strategy is adopted. A basic implementation of the FOC has already been presented in Chapter 4. However, when applied to a non-linear motor model, several modifications are required to adapt the control scheme to account for the motor's variable parameters.

It is evident that a simple PI controller with constant gains cannot be effectively used in this case, since the inductances L_d and L_q vary depending

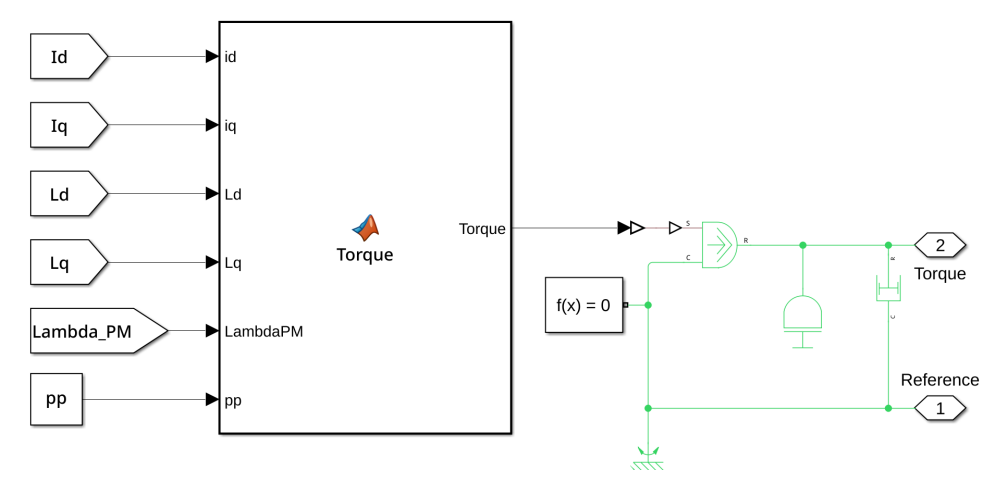


Figure 6.1.9: Simulink subsystem used to generate the electromagnetic torque.

on the operating point. Consequently, a variable PI controller must be employed, where the proportional and integral gains are dynamically adjusted to compensate for the non-linear variations in inductances and other motor parameters.

Furthermore, the voltages V_d and V_q are not solely dependent on their respective currents i_d and i_q . Due to the presence of mutual inductances, a cross-coupling effect occurs between the d- and q-axes, meaning that the voltage in one axis is influenced by the current in the other. This coupling complicates the control of the current loop.

To prevent excessive complexity, a decoupling mechanism is introduced. By using a combination of time-derivative, dot-product, and summing blocks, it is possible to compensate for the influence of the opposing axis current without altering the fundamental structure of the PI controllers. This approach effectively linearizes the system response and simplifies controller tuning

In addition to the mutual inductance effects, the BEMFs must also be considered for accurate current regulation. A dedicated subsystem computes the electromotive forces acting on the d and q-axes. The calculated BEMF terms are then either added (for the q-axis) or subtracted (for the d-axis) from the control signal to achieve proper compensation and ensure precise current tracking.

The overall current control model is shown in Figure 6.2.1.

6.2.1 PI Controllers

As previously discussed, a conventional PI controller with fixed parameters is insufficient for controlling a non-linear motor model. Instead, a variable

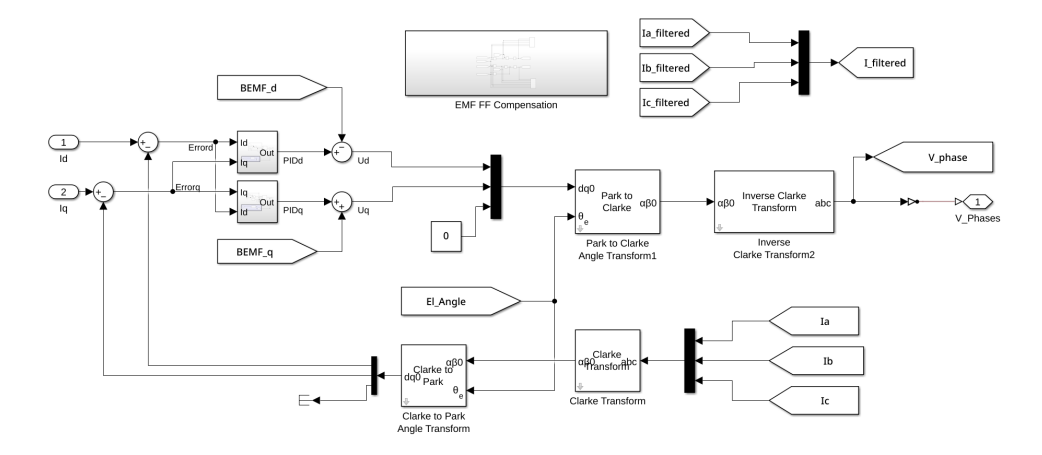


Figure 6.2.1: Overall Simulink model used to implement the current control loop.

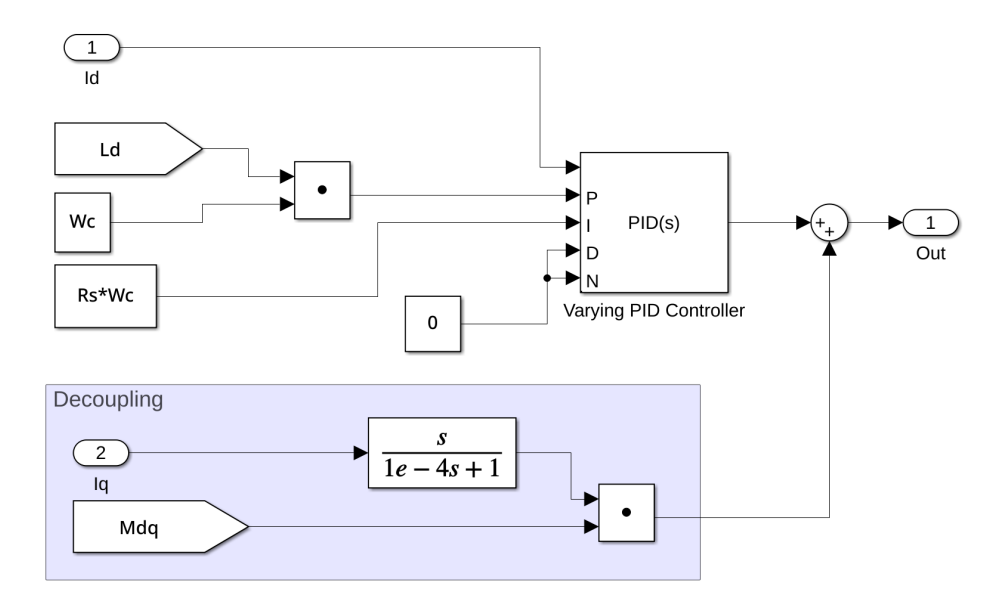


Figure 6.2.2: Implementation of the variable PI controller for the d-axis current loop.

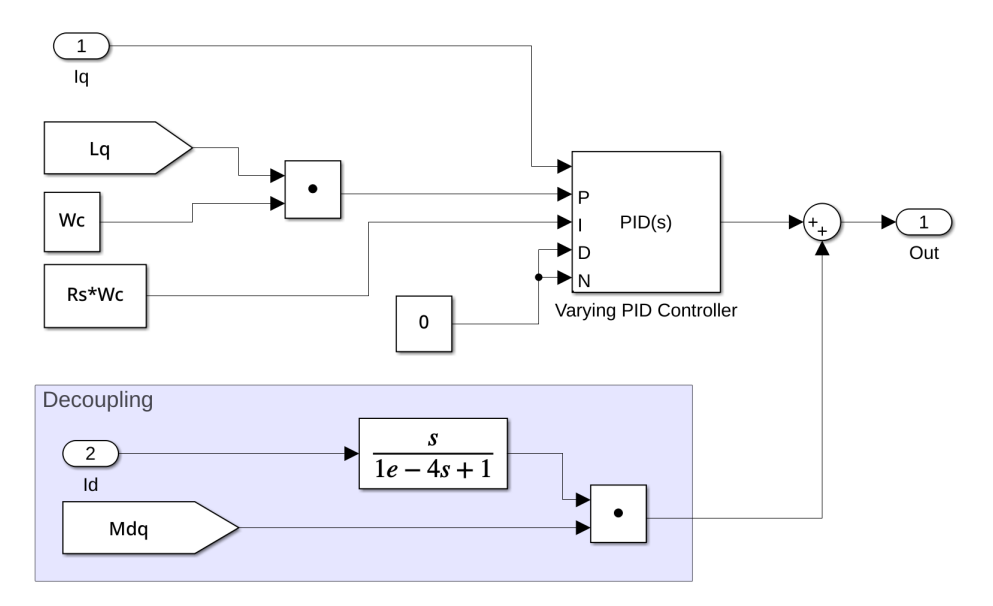


Figure 6.2.3: Implementation of the variable PI controller for the q-axis current loop.

PI controller is adopted, as illustrated in Figure 6.2.2. The controller parameters are adjusted in real time according to the instantaneous operating conditions, allowing the system to maintain stability and achieve the desired dynamic performance over the entire operating range.

In addition to the PI control stage, an auxiliary decoupling block is implemented to compensate for the effects of mutual inductances between the d- and q-axes. This decoupling is achieved by computing the time derivative of each current component and multiplying it by the corresponding mutual inductance term. However, the derivative operation is highly sensitive to measurement noise, which can introduce high-frequency oscillations. To mitigate this effect, a low-pass filter is applied to the derivative signal, ensuring that the decoupling remains effective without amplifying noise or compromising stability.

6.2.2 BEMF Feed-Forward Compensation

To mitigate the effects of the BEMF on control performance, a feed-forward compensation strategy is implemented. The subsystem shown in Figure 6.2.4 provides a practical realization of this approach.

As derived from the voltage equations in (3.21), the BEMF components can be expressed as functions of the rotor speed and the stator flux linkages. Since these quantities are already available within the control architecture, the feed-forward compensation term can be easily computed using basic arithmetic operations such as summations and dot products. This compensation signal is added to the voltage reference, effectively counteracting the voltage drop caused by the BEMF and improving the transient response of the current loop.

Similar to the PI controller structure, a decoupling computation is also included here. By using simple summation and product blocks, the cross-coupling between the d- and q-axes is minimized, allowing the control structure to closely resemble the simplified version presented in Chapter 4.

To preserve the physical realism of the system, a *Saturation* block limits the maximum allowable BEMF compensation value. This constraint prevents the controller from generating unrealistically high voltage commands that would be infeasible in an actual system.

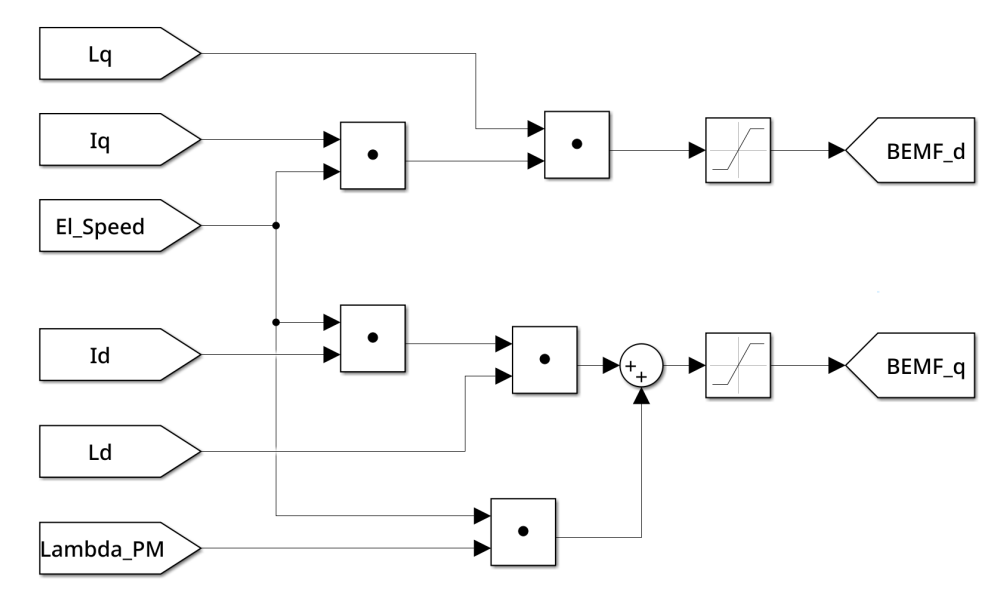


Figure 6.2.4: Simulink subsystem implementing the BEMF feed-forward compensation.

6.3 Speed Control Loop

The speed control loop is responsible for generating the reference currents required to achieve the desired motor speed. Specifically, the control system first determines the torque demand and then computes the corresponding current necessary to produce it.

In this model, showed in Figure 6.3.1, an Abs block has been introduced to accurately represent regenerative braking. Simply applying a negative torque value would result in unrealistic behaviour, as the lookup tables used in the model are defined only for positive i_q and negative i_d values. Without the absolute value operation, the lookup tables could return invalid inductance and flux values, leading to physically inconsistent results.

For this reason, Abs blocks are also incorporated into other subsystems, such as the iron losses computation, to ensure that all simulation results remain physically meaningful.

The reference speed signal is generated using a Wide-Open Throttle block, which produces a customizable time-varying impulse. This signal is then integrated to generate a speed ramp profile. A dedicated MATLAB Function block is used to model the combined effect of regenerative and mechanical braking. During braking, if the demanded torque exceeds the maximum achievable electromagnetic torque, the excess braking torque is provided by the mechanical braking system.

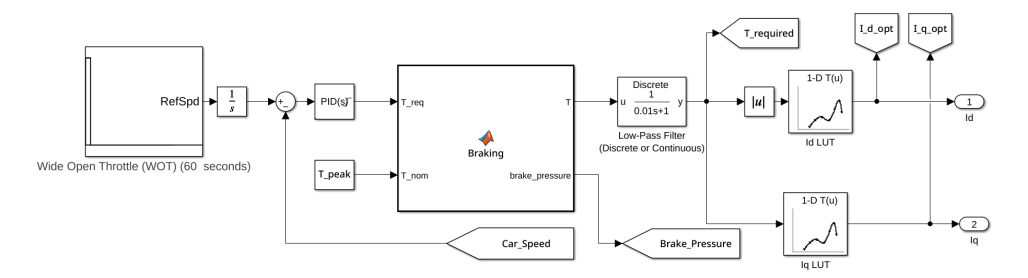


Figure 6.3.1: Simulink subsystem implementing the speed control loop.

6.3.1 PID Controller

To achieve the desired torque response, a PID controller is employed. The controller parameters were tuned through iterative simulations to ensure both system stability and adequate dynamic performance. By carefully adjusting the proportional and integral gains, the transient response and steady-state accuracy of the system were optimized. After several iterations, the following parameter values were found to provide satisfactory results:

$$P = 15, \quad I = 6, \quad D = 4.$$

These gains were consistently applied across all models to ensure uniform control performance and enable a fair comparison between different motor configurations.

6.3.2 MTPA Control Strategy

The incorporation of a gearbox, which will be discussed later on, permits electric motor operation within the nominal speed region, creating favourable conditions for Maximum Torque Per Ampere implementation.

As established in Section 3.4.1, the non-linear nature of motor parameters L_d , L_q , and Λ_{pm} precludes simple analytical solutions for MTPA. Instead, a lookup table approach provides a practical implementation method,

viable when the gearbox maintains operation below base speed within voltage and current limits.

The torque mapping procedure utilizes equation (3.22), computing torque values for comprehensive (I_d, I_q) pairs while accounting for parameter variations through interpolation of experimental data. For each torque setpoint, the optimal current vector minimizing $I_N = \sqrt{I_d^2 + I_q^2}$ is selected, ensuring MTPA operation across the working range.

6.4 Vehicle Dynamics

To develop a realistic vehicle model, it is essential to incorporate the complete dynamics of the vehicle driven by the electric motor, including transmission components and braking systems.

6.4.1 Gearbox Modelling

The transmission system plays a fundamental role in matching the electric motor's operating characteristics with the vehicle's performance requirements. When the motor is supplied with current I, it produces an electromagnetic torque T_{em} and rotates at an angular velocity ω_m . The gearbox transforms these quantities according to the following relationships [31]:

$$G_r = \frac{T_{wheel}}{T_{em}} = \frac{\omega_m}{\omega_{wheel}} = \frac{N_{motor}}{N_{wheel}}$$
(6.12)

where G_r is the gear ratio, T_{wheel} is the torque transmitted to the wheels, and ω_{wheel} is the wheel angular velocity. This relationship derives from the conservation of mechanical power, assuming negligible transmission losses:

$$P_{motor} = T_{em}\omega_m = T_{wheel}\omega_{wheel} = P_{wheel}$$
(6.13)

The selection of the gear ratio represents a fundamental design trade-off between torque multiplication and overall efficiency. During acceleration, higher gear ratios amplify the torque delivered to the wheels, thereby enhancing traction and improving the vehicle's responsiveness. Conversely, at higher vehicle speeds, lower gear ratios allow the motor to operate closer to its optimal efficiency range while maintaining the desired velocity.

In electric vehicles, this balance is typically achieved through either a single-speed reduction gear—offering simplicity, compactness, and high reliability—or a two-speed transmission, which provides improved performance and efficiency across a wider operating range.

In the developed model, the gear-shifting logic is implemented through a *MATLAB Function* block, as illustrated in Figure 6.4.2. The gear selection algorithm evaluates multiple parameters, including the required torque,

rotor speed, and vehicle velocity. Furthermore, the model retains the previously engaged gear ratio and the direction of the shift to ensure a smooth and continuous transition between gears, minimizing torque discontinuities during gear changes.

The resulting gear ratio is then provided as input to a *Variable Ratio Transmission* block, as can be seen in Figure 6.4.1, which effectively transfers torque and rotational speed between the motor and the vehicle while executing the gear shift. Finally, two *Ideal Torque Sensor* blocks are placed in the model to measure, respectively, the electromagnetic torque generated by the motor and the torque transmitted to the wheels.

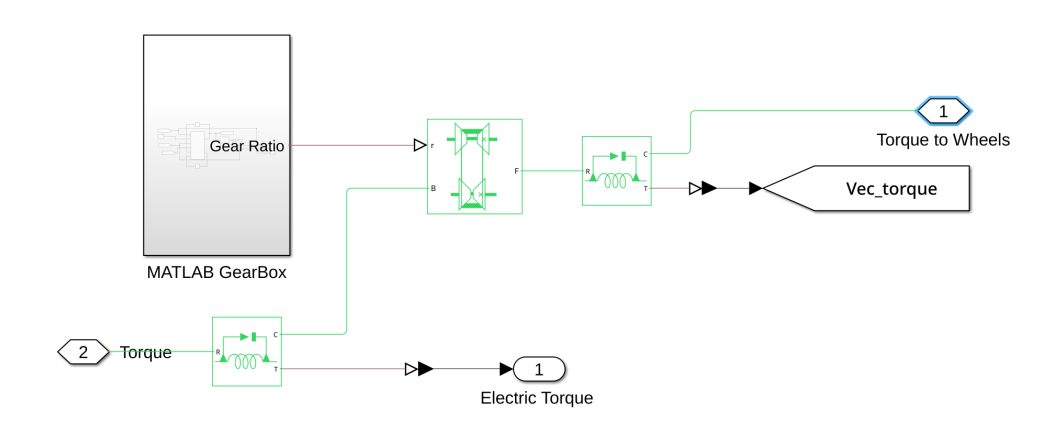


Figure 6.4.1: Simulink implementation of two speed transmission.

6.4.2 Vehicle Body Dynamics

The vehicle longitudinal dynamics are modelled using Simulink's "Vehicle Body" block, which implements the fundamental equations of motion. The block calculates vehicle acceleration based on the net force acting on the vehicle [32]:

$$m_{veh}\frac{dv_x}{dt} = F_{traction} - F_{aero} - F_{grade} \tag{6.14}$$

where:

- m_{veh} : vehicle mass
- v_x : longitudinal vehicle velocity
- $F_{traction} = \frac{T_{wheel}}{R_{wheel}}$: traction force
- $F_{aero} = \frac{1}{2}\rho C_d A(v_x + v_{wind}^2 sgn(v_x + v_{wind}))$: aerodynamic drag force

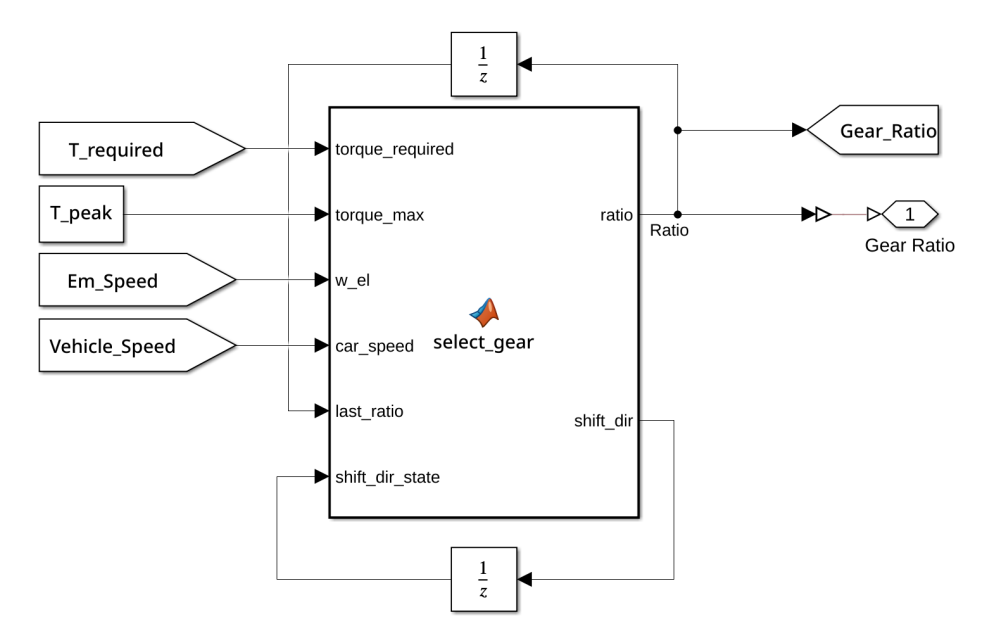


Figure 6.4.2: Focus on the matlab function block used to generate the control signal for the variable gear box block.

- $F_{qrade} = m_{veh}g\sin(\theta)$: grade resistance
- C_d : aerodynamic drag coefficient
- ρ : density of the air
- A: effective front vehicle cross-section area
- v_{wind} : wind speed
- θ : road incline angle

The block outputs vehicle velocity, which closes the control loop by providing feedback to the speed controller, which in turn generates current references for motor control. Two *Tire* blocks are added to properly model the vehicle behaviour. Lastly two *Disk Brake* blocks are used in order to simulate a mechanical braking system.

6.4.3 Braking System

The braking system employs a blended approach combining regenerative braking through the electric motor and mechanical friction braking. While the electric motor can provide substantial braking torque through negative current injection (regenerative braking), its capacity is limited by motor characteristics and battery state of charge.

The mechanical brake supplements the regenerative system according to:

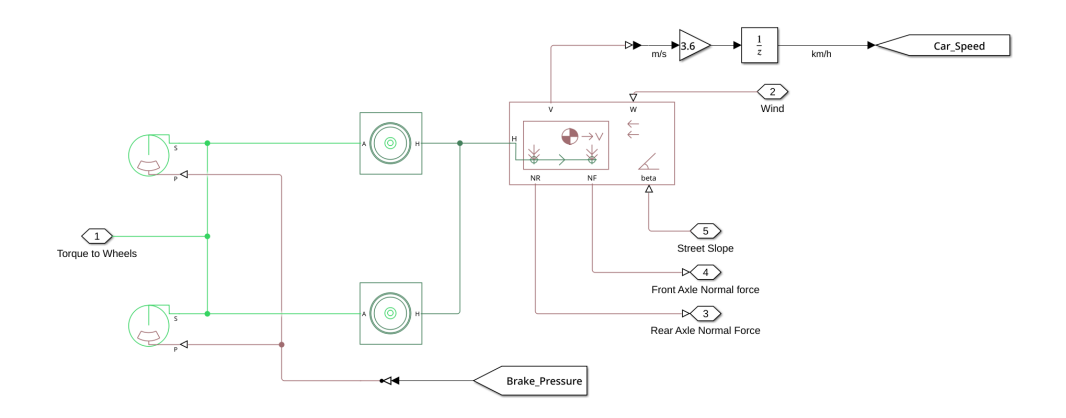


Figure 6.4.3: Simulink vehicle section with added disk brakes.

$$T_{brake,mech} = T_{brake,req} - T_{brake,regen} \tag{6.15}$$

where:

 $T_{brake,req}$: total required braking torque

 $T_{brake,regen}$: regenerative braking torque available from motor

 $T_{brake,mech}$: mechanical braking torque

Simulink's *Disk Brake* block implements this functionality, receiving as input the torque deficit between requested braking and regeneratively available braking. This approach maximizes energy recovery during deceleration while ensuring braking performance meets safety requirements.

Chapter 7

Experimental Results and Comparative Analysis

This chapter presents a comprehensive comparison of three distinct motor models: a nonlinear reference model, a PMSM model with constant parameters, and an enhanced PMSM model incorporating variable parameters. The analysis aims to evaluate the impact of parameter variation on model fidelity and performance prediction accuracy.

7.1 Experimental Setup

The LUTs utilized in this study are derived from an IPSM. However, the original motor parameters were not optimized for high-performance automotive applications. To ensure realistic simulation outcomes, the reference speed profile has been scaled to a maximum of $50 \ km/h$, maintaining physical consistency while accommodating the operational constraints of the available motor data. For the sake of simplicity the inverter has been substituted by a voltage source generator and both the wind speed and road angle have been set to zero. The main parameters used for the simulations are showed in the following table.

7.1.1 Gearbox Artifact

A multi-ratio gearbox was implemented to extend the operational speed range of the propulsion system. It is important to emphasize that proper gearbox implementation typically requires an integrated clutch mechanism for smooth torque transmission during gear shifts.

The standard Simulink library lacks a comprehensive clutch block capable of simulating gradual engagement and disengagement through external control signals. While it is technically feasible to develop a custom clutch model, the associated complexity would substantially increase the model's

Parameter	Value	Symbol
Pole Pairs	4	p_p
Slot Number	24	\overline{Q}
Stator Resistance $[m\Omega]$	1.8	R_s
Rated Torque [Nm]	12	T_n
Peak Torque [Nm]	15	T
Rated Current [A]	110	I_n
Maximum Current [A]	150	I_{max}
Rated Speed [rpm]	3500	ω_n
DC BUS Voltage [V]	48	V_{DC}

Table 7.1: Main parameters used for the simulations

computational demands without providing significant improvements to the core research objectives.

As an alternative approach, a continuously variable transmission model was employed to approximate clutch behaviour. However, this simplification introduces transient artifacts during gear ratio changes, including:

- Unphysical torque spikes exceeding realistic mechanical limits
- Transient efficiency variations that deviate from physical system behaviour
- Instantaneous speed transitions that violate conservation principles

Consequently, simulation results obtained during gear shift transients have been excluded from the comparative analysis to maintain the validity of performance evaluations.

7.2 Comparative Analysis with Constant Parameters Model

The first model used for comparison is the most simple for an anisotropic PMSM. In particular it consider the parameter Ld, Lq and λ_{PM} as constant and doesn't take into account the iron losses. In all models to obtain the required torque, a LUT has been used. Of course, since in this case the parameters are considered constant, the LUT of the two compared model are different from one another.

7.2.1 Voltage and Current Evaluation

This section presents a comparison of the voltages and currents obtained from the two models. As illustrated in Figure 7.2.2, the difference in phase

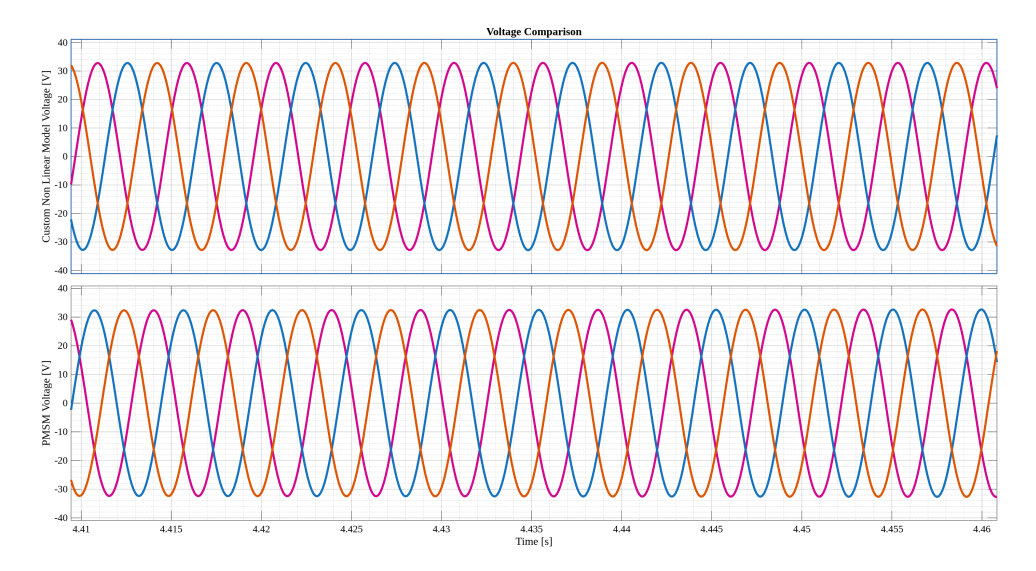


Figure 7.2.1: Maximum voltage obtained during operation. Top: custom nonlinear model phase voltages. Bottom: Simulink PMSM block phase voltages

voltage during steady-state operation, which corresponds to a rotor velocity of $2200 \ rpm$ and a vehicle speed of $50 \ km/h$, is modest, with a peak deviation of approximately $0.2 \ V$. This small discrepancy should not be evaluated in isolation, as the two models employ different lookup tables to generate the driving currents.

Due to the idealized nature of the reference model, its efficiency is expected to be higher than that of the custom model—an expectation that is confirmed in the following section. Nevertheless, no significant differences in the phase voltage values are observed, primarily because the phase currents are noticeably lower. When the comparison is extended to include both current and voltage values, the distinction between the two models becomes clearer.

In general, since the models use distinctly different current profiles to drive the motor (as shown in Figure 7.2.4 and Figure 7.2.3), the comparison should focus on metrics such as efficiency and absorbed power, or on the joint analysis of voltage and current values rather than considering voltage alone.

Finally, the maximum voltage reached during the simulation, shown in Figure 7.2.1, is approximately $0.2\ V$ higher in the custom model. This result is expected, as the custom model accounts for iron losses, which become significant at high speeds and high stator currents. These losses consume additional power, thereby reducing the terminal voltage. However, this difference should be interpreted with caution, acknowledging the intrinsic differences between the two models.

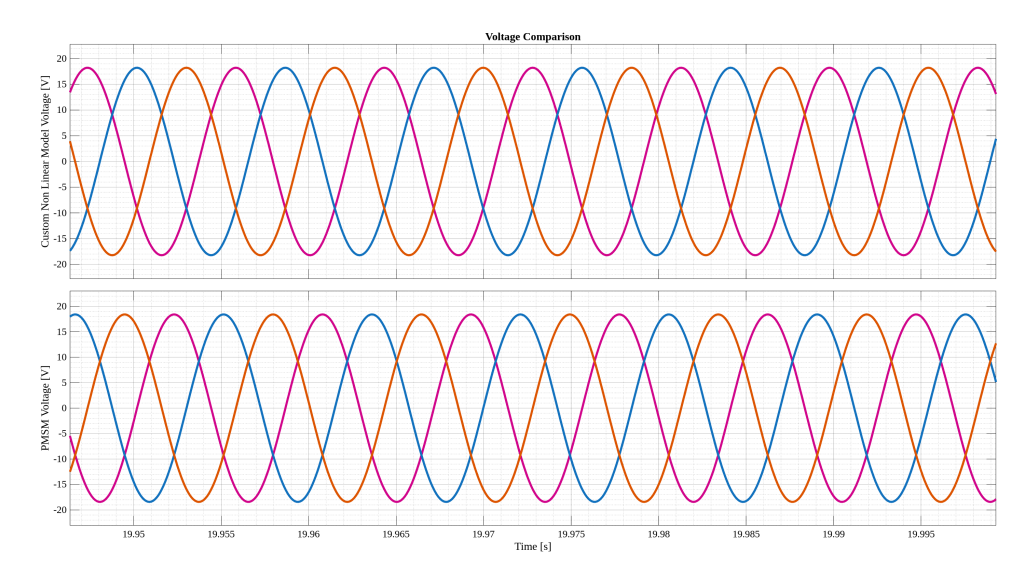


Figure 7.2.2: Steady-state voltage comparison at 50 km/h vehicle speed (2200 rpm motor speed). Top: custom nonlinear model phase voltages. Bottom: Simulink PMSM block phase voltages.

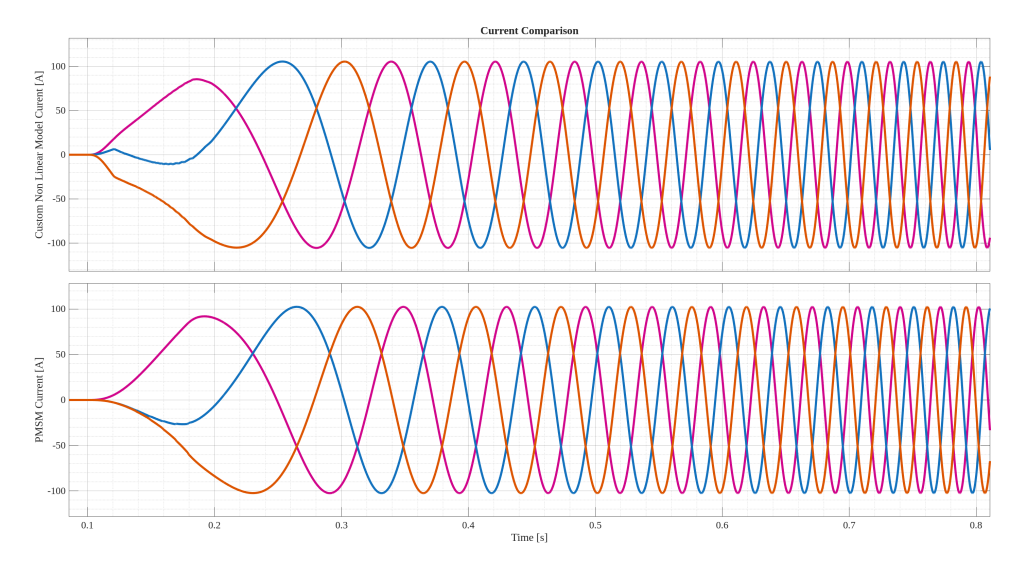


Figure 7.2.3: Initial transient current comparison. Top: custom nonlinear model phase currents. Bottom: Simulink PMSM block phase currents

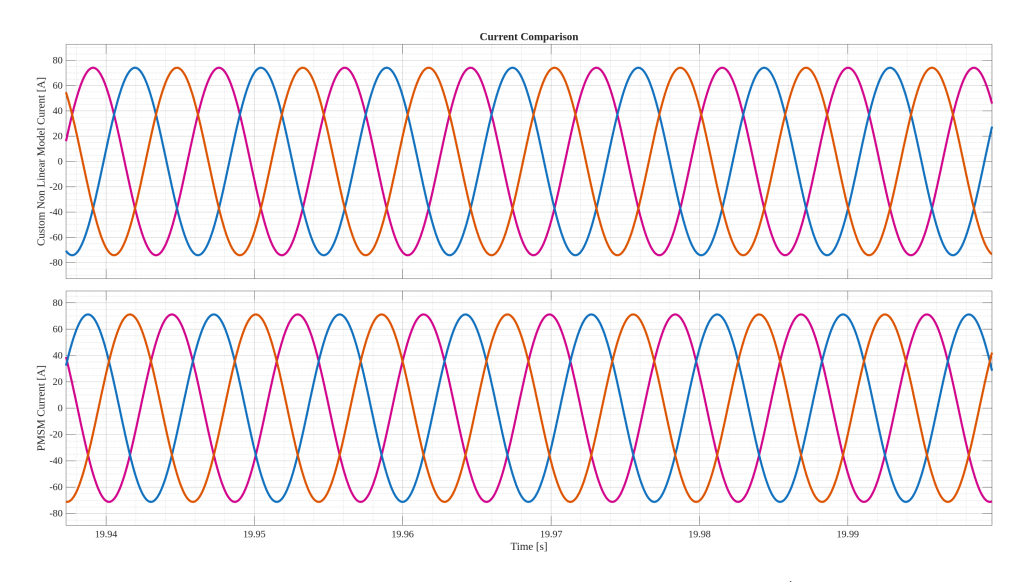


Figure 7.2.4: Steady-state current comparison at 50 km/h vehicle speed (2200 rpm motor speed). Top: custom nonlinear model phase currents. Bottom: Simulink PMSM block phase currents

Parameter	Ideal PMSM	Custom Model
Spurt Current [A]	102.97	105.46
Regime Current [A]	71.18	75.1
Maximum Voltage [V]	32.74	32.90
Regime Voltage [V]	18.42	18.23

Table 7.2: Comparison between the Simulink PMSM model and the custom model $\,$

7.2.2 Torque and Speed Performance Evaluation

Figure 7.2.5 illustrates the torque and speed response of both motor models. The results confirm that both the ideal and custom PMSMs produce highly similar electric torque and resulting vehicle speed profiles, validating the fundamental operational similarity of the models.

The figure also highlights an undesired ripple in the electric torque. This artifact is a result of employing a variable gearbox instead of a clutch, as previously discussed in subsection 7.1.1.

The operation of the variable gearbox is detailed in Figure 7.2.6. The plot shows the gear ratio being reduced from 8 to 4. This reduction causes a corresponding decrease in the electric motor's speed while simultaneously increasing the vehicle's speed, demonstrating the fundamental trade-off governed by the transmission system. Of course the slope of the vehicle speed after the gear ratio change decreases, since the torque to wheel is reduces and so does the acceleration .

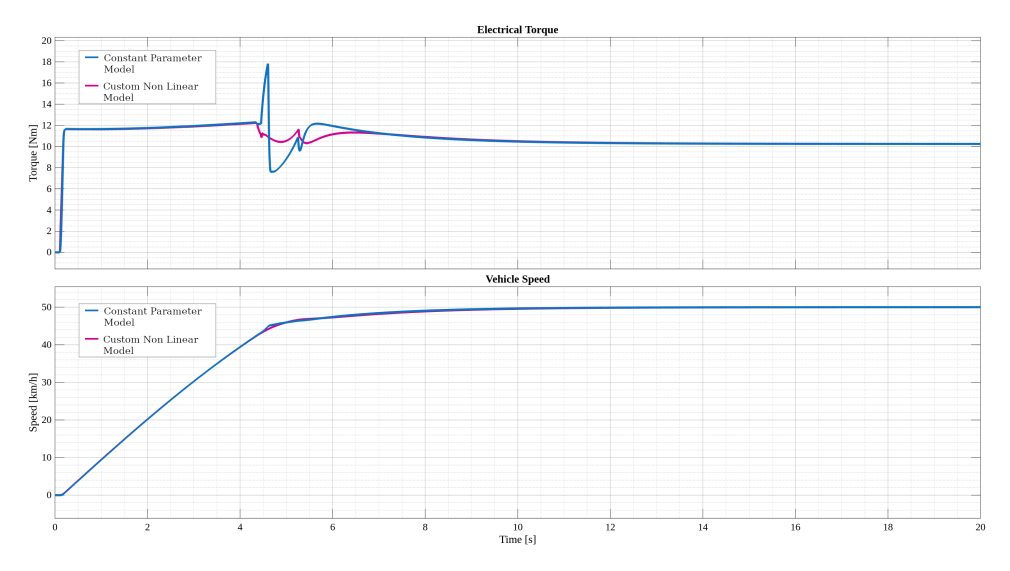


Figure 7.2.5: Comparison of electric torque generated [Nm] and vehicle speed [km/h] reached. Fuchsia: custom non linear model. Blue: Ideal PMSM model.

7.2.3 Power Efficiency Performance Evaluation

The efficiency performance of the ideal and custom PMSM models is evaluated in Figure 7.2.7 for steady-state operation and in Figure 7.2.8 for the initial transient. As anticipated, the ideal model demonstrates higher efficiency in both scenarios. This is a direct consequence of its simplified nature, which omits non-linear phenomena such as cross-saturation and iron losses.

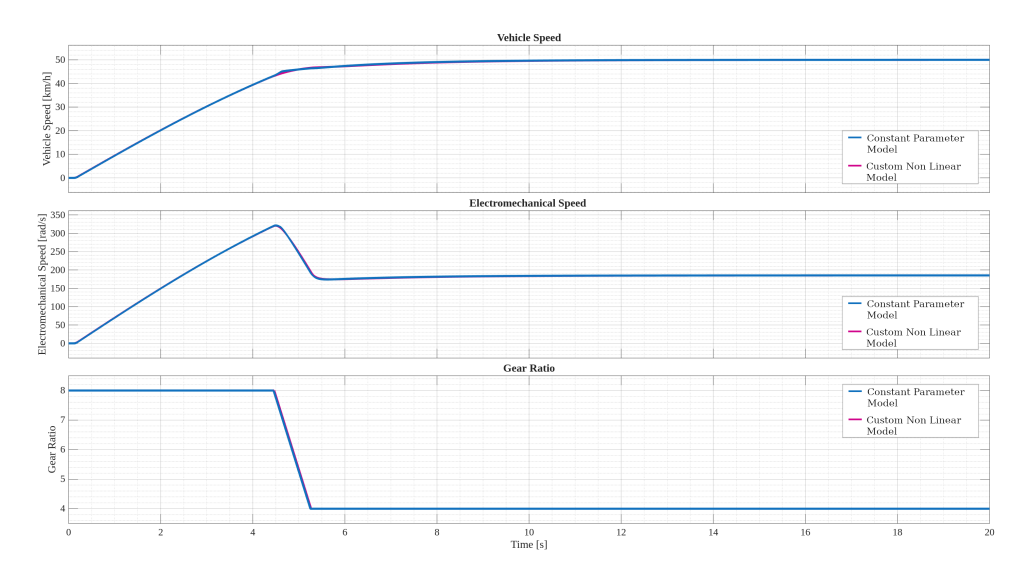


Figure 7.2.6: Comparison of vehicle speed [km/h], rotor speed [rad/s] and gear ratio. Fuchsia: custom non linear model. Blue: Ideal PMSM model.

The efficiency discrepancy between the two models is more pronounced during the initial transient, reaching a maximum discrepancy of 4.5 %. This can be attributed to rapid changes in stator currents, which excite the non-linear effects modelled in the custom machine. During steady-state operation, however, the stator currents vary minimally, allowing the parameters L_d , L_q , and $\lambda_{\rm PM}$ to be treated as constants. Consequently, the remaining efficiency difference in this regime is primarily due to the iron losses accounted for in the custom model, which reaches a value of 1.4 %.

In Figure 7.2.9 a power comparison is showed. As expected the custom model absorbs more power since it accounts for more losses compared to the ideal model. Approximately at $4.5\ s$ the artifacts due to the change of gear ratio. The variation in output power following this transition occurs because the motor is approaching steady-state operation. In this phase, the vehicle reaches its reference speed, the required torque decreases, and consequently both the absorbed and delivered power are reduced.

7.3 Comparative Analysis with Variable Parameters Model

The final comparative analysis utilizes the Simulink PMSM block enhanced with Look-Up Table functionality to model the variations in dq-axis inductances L_d , L_q and permanent magnet flux linkage λ_{pm} .

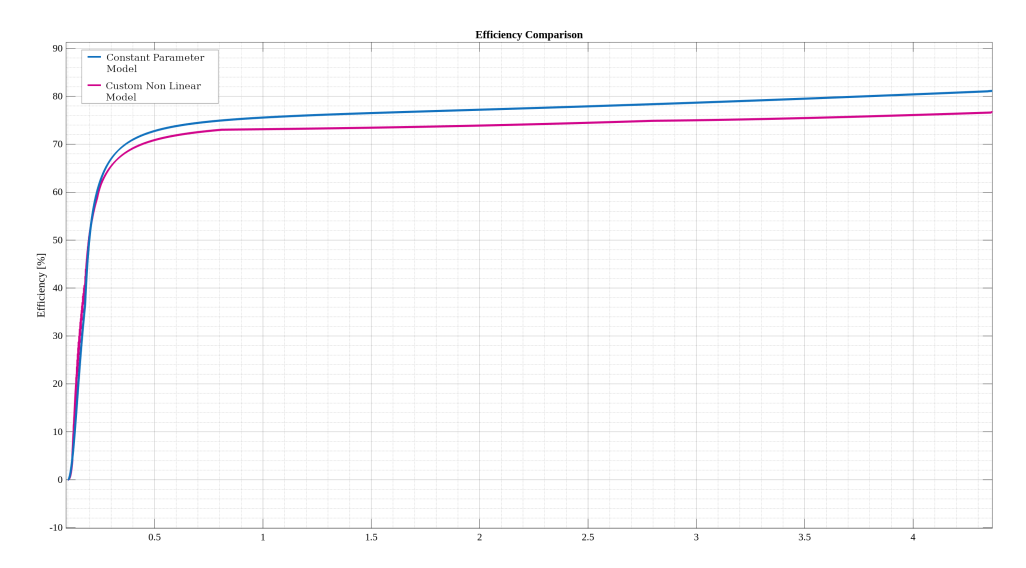


Figure 7.2.7: Efficiency comparison during initial transient. Fuchsia: custom non linear model. Blue: Ideal PMSM model.

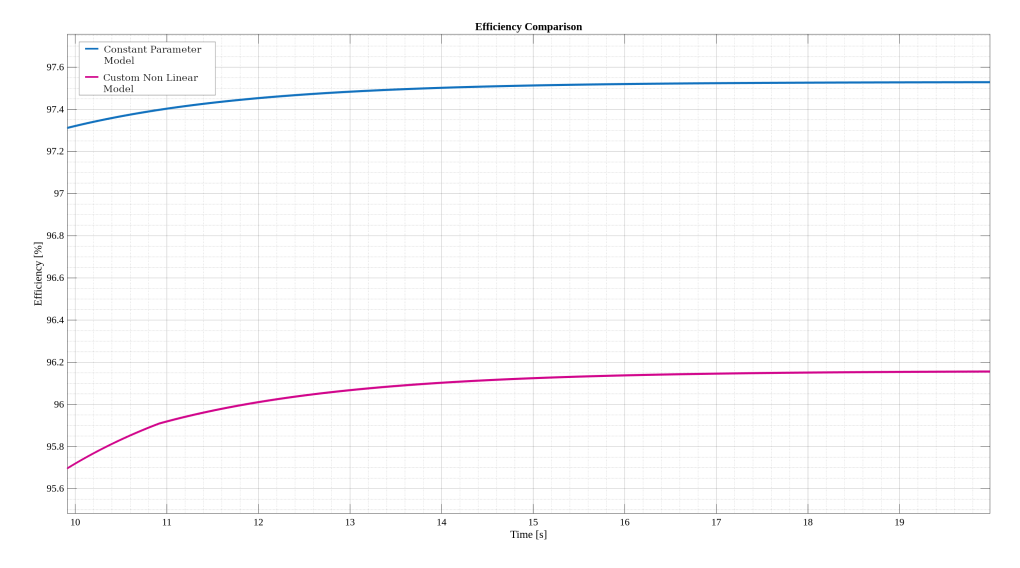


Figure 7.2.8: Efficiency comparison during steady state operation. Fuchsia: custom non linear model. Blue: Ideal PMSM model.

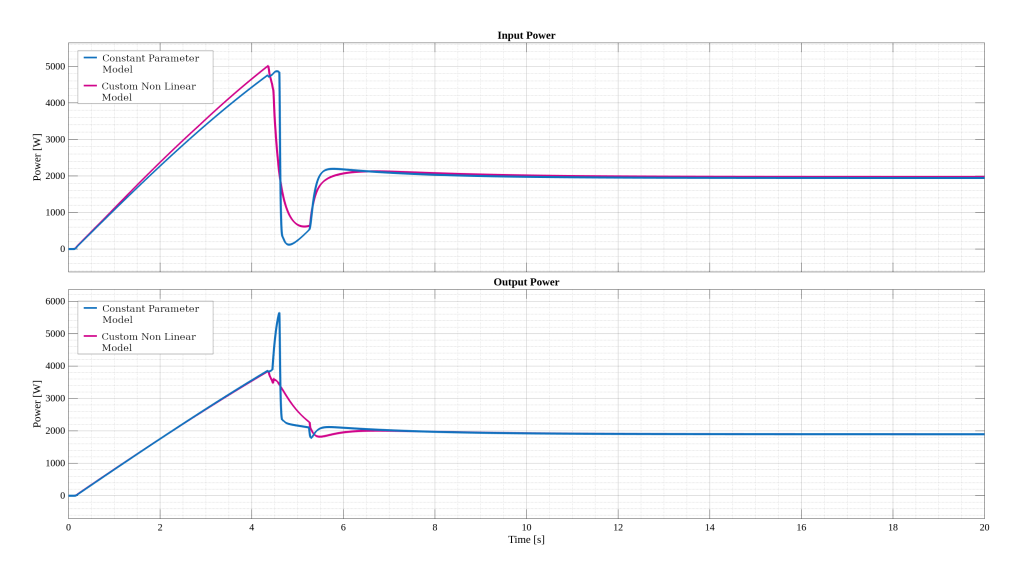


Figure 7.2.9: Input and output power comparison. Fuchsia: custom non linear model. Blue: Ideal PMSM model.

7.3.1 Voltage and Current Evaluation

Figure 7.3.2 illustrates the phase voltage waveforms at a steady-state rotor speed of 2200~rpm, corresponding to a vehicle velocity of $50~\mathrm{km/h}$. The modest voltage discrepancy of approximately 0.5~V between the two models reflects the low iron losses present at this velocity. These losses are limited because the steady-state operating regime demands lower driving currents compared to acceleration spurts.

However, analysis of the complete acceleration transient reveals more pronounced deviations. During high-torque spurt conditions, where motor speed and armature currents reach elevated levels, the voltage discrepancy increases to approximately $1.5\ V$. These results must be interpreted considering scaling effects; in full-scale automotive applications where phase currents can exceed $1\ kA$, the influence of iron losses on terminal voltages would be considerably more significant.

Since both models employ the same LUTs for stator currents generation, the phase currents during acceleration and steady-state operation are nearly identical, with a maximum observed deviation of $0.15\ A$.

7.3.2 Torque and Speed Performance Evaluation

Figure 7.3.5 presents a comprehensive comparison of the torque output, rotational speed, and transmission ratio dynamics. The proposed model accurately captures the electromechanical behaviour of the motor, thereby providing a reliable prediction of the vehicle's speed response. As expected, both models yield identical torque profiles and consequently achieve the

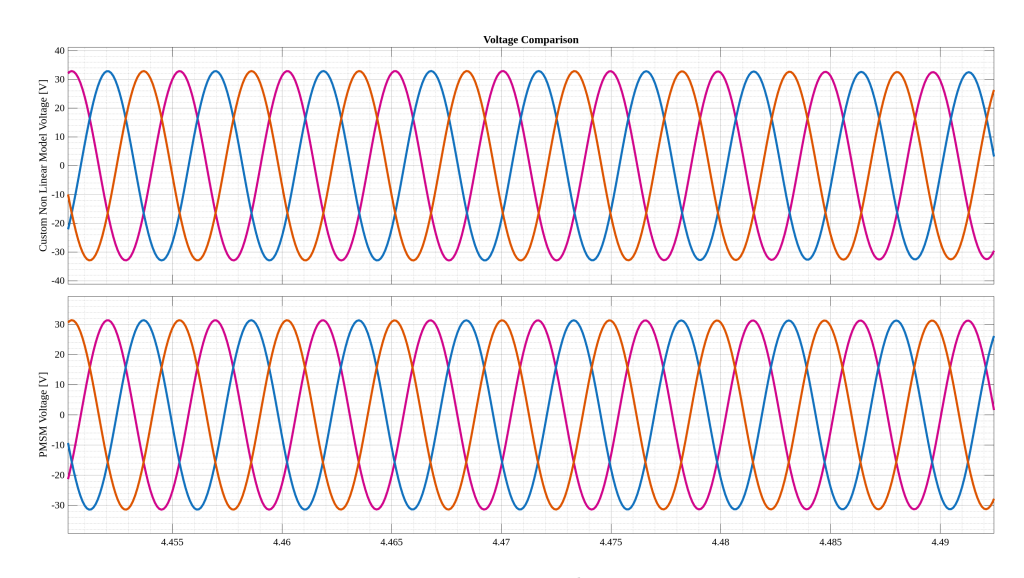


Figure 7.3.1: Maximum voltage comparison.

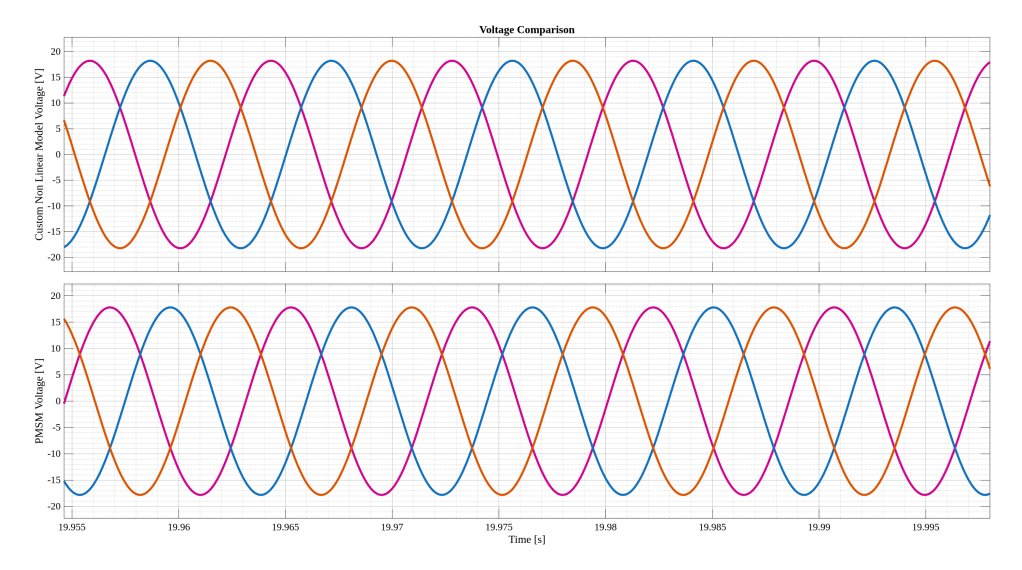


Figure 7.3.2: Steady-state voltage comparison at 50 km/h vehicle speed (2200 rpm motor speed). Top: custom nonlinear model phase voltages. Bottom: Non linear PMSM Simulink model phase voltages.

Parameter	Nonlinear PMSM	Custom Model
Spurt Current [A]	105.55	105.40
Regime Current [A]	74.03	74.10
Maximum Voltage [V]	31.43	32.90
Regime Voltage [V]	17.79	18.23

Table 7.3: Comparison between the results obtained with the nonlinear PMSM Simulink model and the custom model

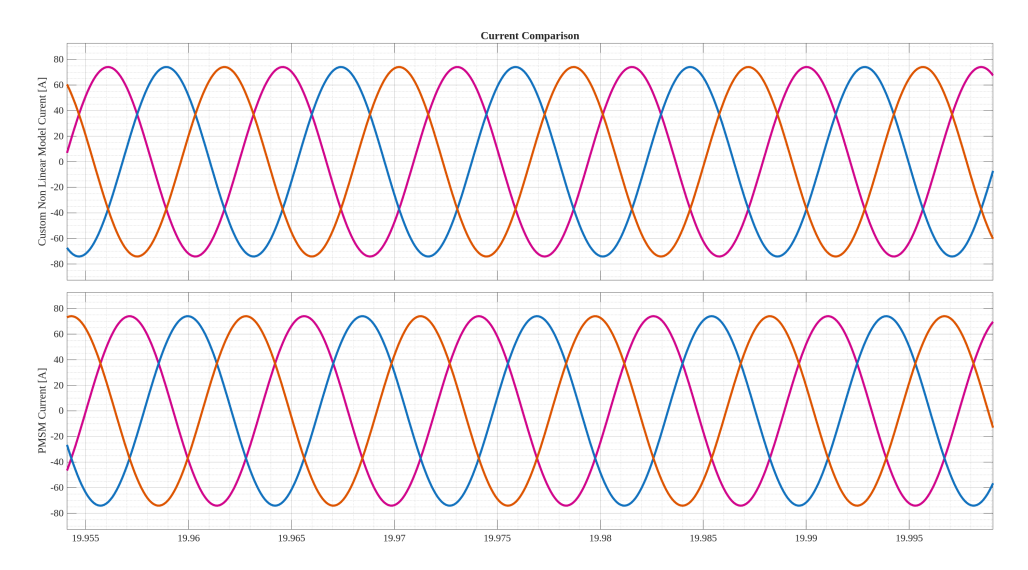


Figure 7.3.3: Steady-state current comparison at 50 km/h vehicle speed (2200 rpm motor speed). Top: custom nonlinear model phase currents. Bottom: Non linear PMSM Simulink model phase currents.

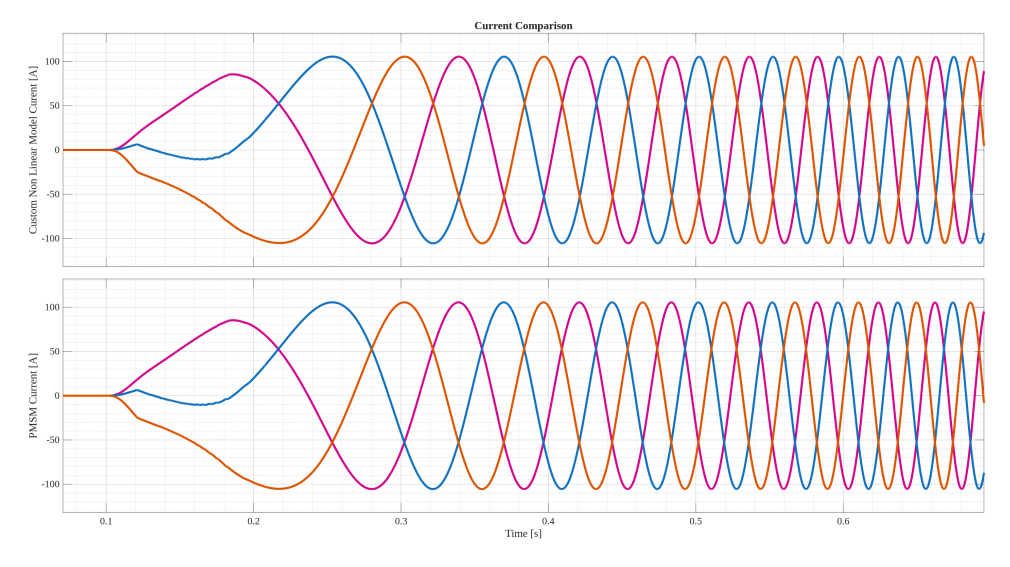


Figure 7.3.4: Transient current comparison during acceleration phase. Top: custom nonlinear model phase currents. Bottom: Non linear PMSM Simulink model phase currents.

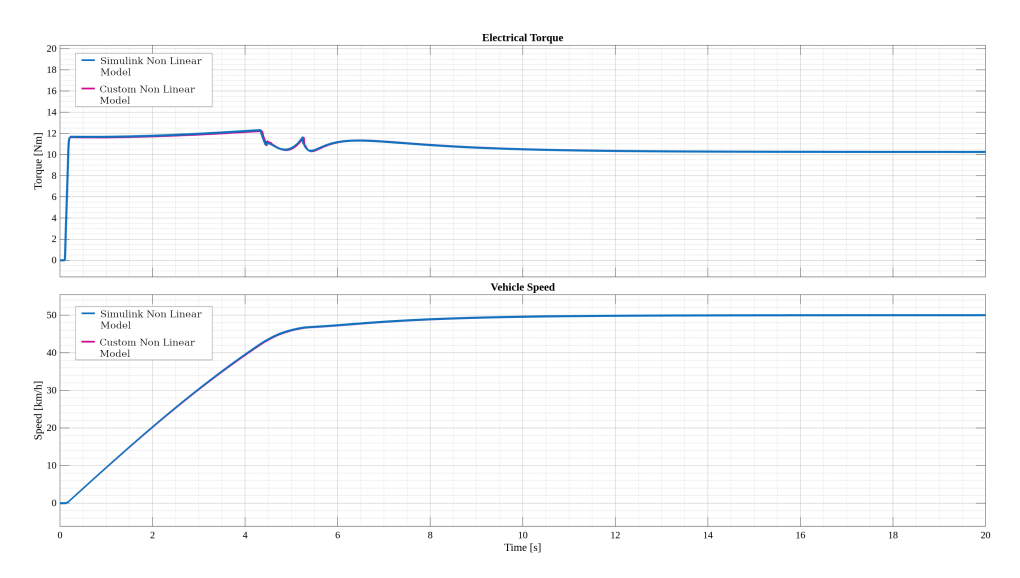


Figure 7.3.5: Comparison of torque produced by the electric motors and the obtained vehicle speed. Fuchsia: custom non linear model. Blue: Non linear PMSM Simulink model.

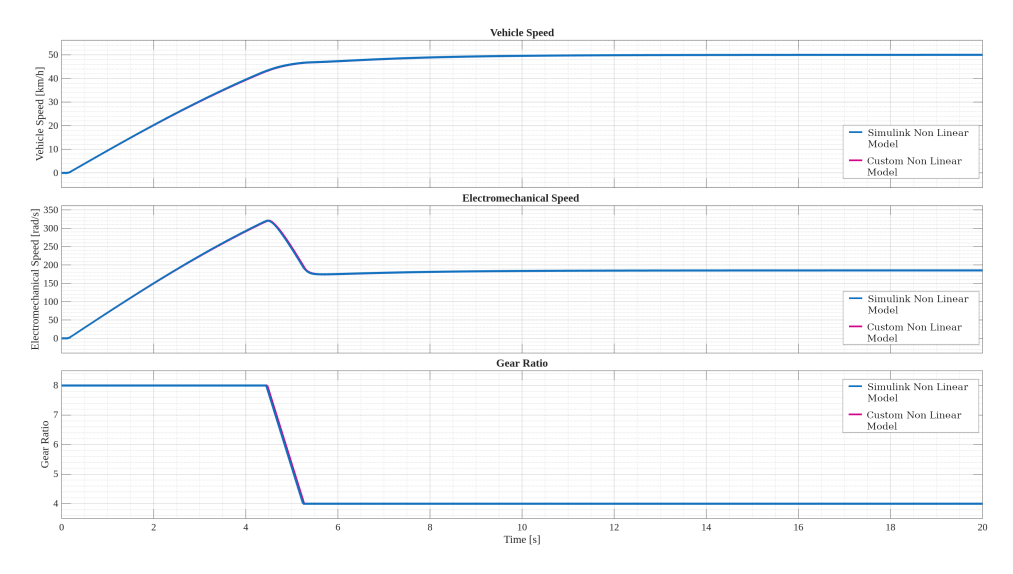


Figure 7.3.6: Comparison between the vehicle speed, the rotor speed and the gear ratio used. Fuchsia: custom non linear model. Blue: Non linear PMSM Simulink model.

7.3.3 Power and Efficiency Performance Evaluation

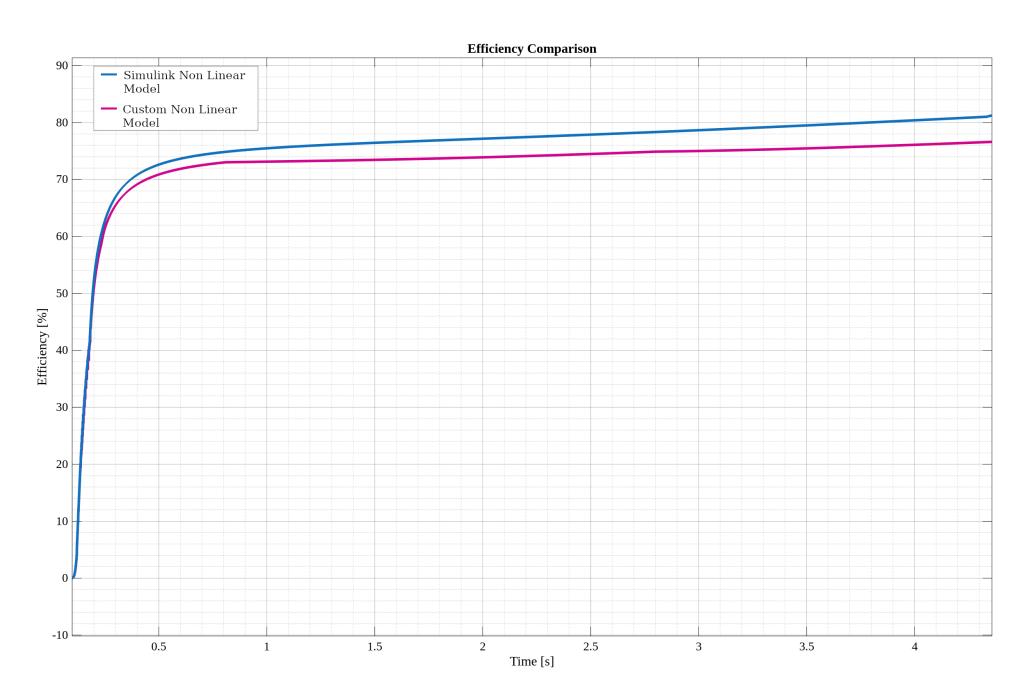


Figure 7.3.7: Efficiency comparison during initial transient. Fuchsia: custom non linear model. Blue: Non linear PMSM Simulink model.

The proposed model, which explicitly accounts for iron losses and variations in mutual inductance, exhibits a consistent reduction in operational efficiency compared to the standard Simulink PMSM implementation. This efficiency gap persists throughout the entire simulation, underscoring the significant influence of the additional physical phenomena on the overall electromechanical performance of the machine.

During the initial acceleration phase, the custom model displays the most pronounced deviation in efficiency relative to the ideal PMSM model, approximately 4 %. This behaviour is expected, as the motor operates under its highest current amplitudes and rotational speeds during this transient period. Consequently, the increased magnetic flux variation in the stator core leads to elevated hysteresis and eddy-current losses, which directly contribute to the observed reduction in efficiency.

In contrast, under steady-state operating conditions, the relative impact of iron losses becomes less significant despite the sustained high rotor speed. This is primarily because the stator current required to maintain constant torque and velocity is substantially lower than during acceleration. As a result, magnetic flux variations within the core are reduced, mitigating both

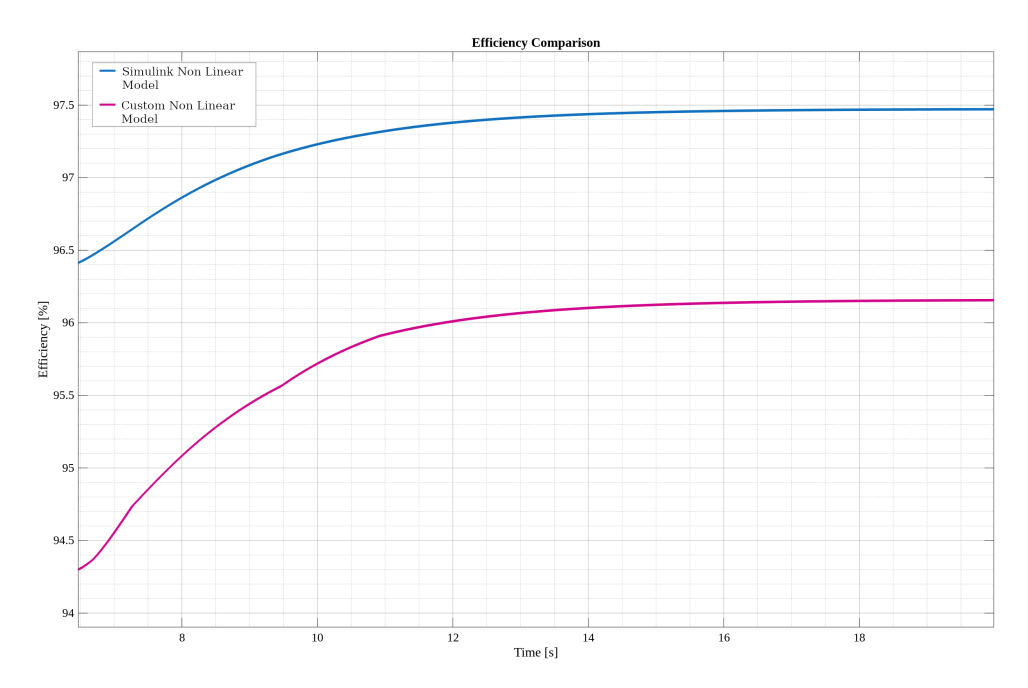


Figure 7.3.8: Efficiency comparison during steady state operation. Fuchsia: custom non linear model. Blue: Non linear PMSM Simulink model.

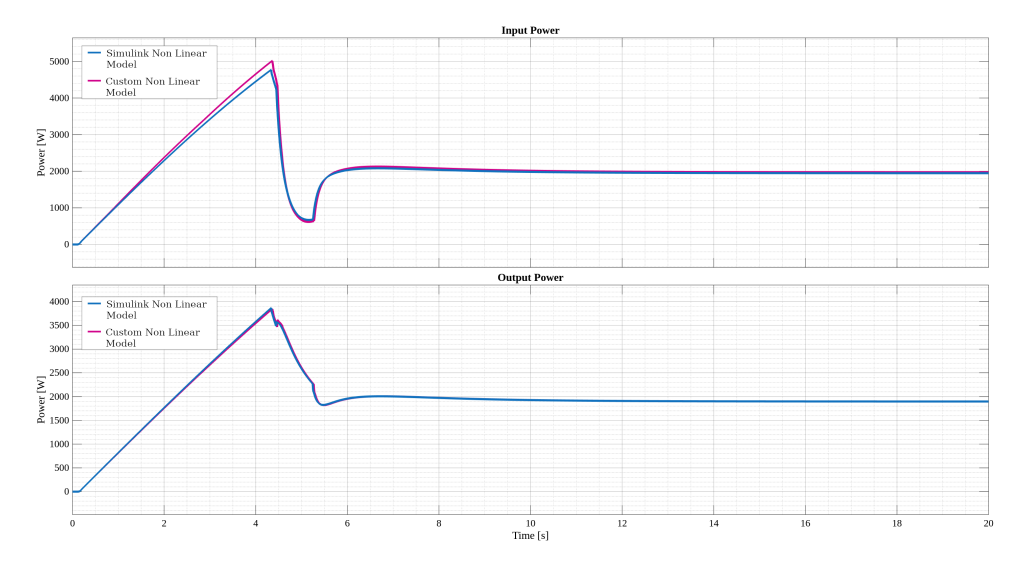


Figure 7.3.9: Input and output power comparison. Fuchsia: custom non linear model. Blue: Ideal PMSM model.

hysteresis and eddy-current effects. Accordingly, the steady-state efficiency improves compared to the transient phase, with the efficiency difference narrowing to approximately 1.3 %.

Chapter 8

Conclusions and Future Work

This thesis has demonstrated the development and validation of an advanced IPMSM model that effectively captures the complex non-linear behaviours and iron losses characteristic of this motor topology. The comprehensive modelling approach presented in this thesis provides significant improvements over traditional constant-parameter models, particularly in high-performance applications.

8.1 Summary of Contributions

The analysis reveals distinct application domains where different modelling approaches are most appropriate:

8.1.1 Low-Power Applications

For low-power applications, the conventional constant-parameter PMSM model remains a viable solution. The limited current demands in these applications result in minimal variations in inductances and magnetic flux linkage, making the simplified model sufficiently accurate for most design purposes while maintaining computational efficiency.

8.1.2 High-Performance Applications

In contrast, high-performance applications such as automotive propulsion systems necessitate the use of non-linear models to achieve satisfactory prediction accuracy. The proposed model addresses this need by incorporating:

- current-dependent variations in self and mutual inductances
- Magnetic flux linkage saturation and cross-coupling effects

• Comprehensive iron loss modelling across the operational range

8.2 Model Advantages and Implementation

The developed framework offers several distinct advantages over conventional approaches. By leveraging lookup table-based parametrization rather than relying exclusively on closed-form analytical expressions, the model maintains a favourable balance between computational efficiency and physical accuracy. However, successful implementation requires comprehensive characterization of motor parameters through either experimental analysis or numerical analysis, in this case through FE simulations complemented by FP analysis for accurate parameter extraction under saturated conditions.

8.3 Future Research Directions

Several promising directions for future research emerge from this work:

- Integration of thermal modelling to capture temperature-dependent effects on permanent magnet flux and winding resistance
- Extension to fault condition analysis, including short-circuit and openphase scenarios
- Development of reduced-order models maintaining accuracy while further improving computational efficiency

The modelling methodology presented in this thesis provides a solid foundation for accurate IPMSM simulation in demanding applications, bridging the gap between idealized analytical models and computationally intensive finite-element approaches.

Chapter 9

Acknowledgments

I am deeply grateful to my supervisors, Professors Alberto Bellini and Claudio Bianchini, for their fundamental guidance and for supporting me through the many challenges of this project.

My sincere thanks also go to Dr. Giada Sala, who always found the time to help me, even while working tirelessly to complete her Ph.D. program.

A very special thank you goes to my dream team, composed of Emanuele, also known as the best companion, and Klevis, the best tutor. Without you, my master's journey would not have been nearly as wonderful or as enjoyable.

I would also like to thank my dear friend Luca, who was always there for me, especially during difficult times when I needed someone to talk to. Thank you for being a trusted confidant even during the most demanding times.

Finally, I would like to thank my parents, whose constant support, encouragement, and love made all of this possible.

Bibliography

- [1] Zhi Cao et al. "An Overview of Electric Motors for Electric Vehicles". In: (2021), pp. 1–6. DOI: 10.1109/AUPEC52110.2021.9597739.
- [2] Stephen J Chapman. Electric Machinery Fundamentals. 2004.
- [3] Austin Hughes and Bill Drury. *Electric motors and drives: fundamentals, types and applications*. Newnes, 2019.
- [4] David J Griffiths. *Introduction to electrodynamics*. Cambridge University Press, 2023.
- [5] Siemens. Basics of AC Motors. Accessed: 18-08-2025. Kh.AquaEnergyExpo.com. 2011. URL: https://kh.aquaenergyexpo.com/wp-content/uploads/2025/02/Basics-of-AC-Motors-A-Quickstep-Online-Course.pdf.
- [6] Equipmake. Axial Flux Motor vs Radial Flux Motor. Accessed: 13-09-2025. 2025. URL: https://equipmake.co.uk/knowledge-base/axial-flux-motor-vs-radial-flux-motor/.
- [7] Pengky. Principle of Transverse Flux Permanent Magnet Generator. Accessed: 2025-09-13. URL: https://www.pengky.cn/zz-direct-drive-turbine/transverse-flux-generator/transverse-flux-generator.html.
- [8] University of Stuttgart Institute of Electrical Energy Conversion. Transverse Flux Machine as direct drive in electric mobility. Accessed: 13-09-2025. URL: https://www.iew.uni-stuttgart.de/en/research/electricalMachines/tfm_direct/.
- [9] Electrical Info. Parts of an Electric Motor: A Complete Guide. Accessed: 18-08-2025. 2023. URL: https://www.electrical-info.net/2023/02/parts-of-electric-motor.html.
- [10] Lam Motor. What is Stator Winding? Accessed: 08-09-2025. Lam Motor. URL: https://lammotor.com/what-is-stator-winding/.
- [11] Jürgen Hagedorn, Florian Sell-Le Blanc, and Jürgen Fleischer, eds. Handbook of Coil Winding: Technologies for efficient electrical wound products and their automated production. Springer-Verlag, 2018. ISBN: 978-3-662-54402-0. DOI: 10.1007/978-3-662-54402-0.

- [12] Motors and Karim Ul Hasan Pump. *AC Motor Winding Design*. Accessed: 08-09-2025. Motors and Pump. URL: https://motorsandpump.com/ac-motor-winding-design/.
- [13] Mustafa Karamuk. "A survey on electric vehicle powertrain systems". In: International Aegean Conference on Electrical Machines and Power Electronics and Electromotion, Joint Conference. 2011, pp. 315–324. DOI: 10.1109/ACEMP.2011.6490617.
- [14] Components of Powertrain. Accessed: 20-08-2025. International Electric Car. URL: https://internationalelectriccar.com/electriccars/working/components-of-powertrain/.
- [15] Thomas Finken, Matthias Felden, and Kay Hameyer. "Comparison and design of different electrical machine types regarding their applicability in hybrid electrical vehicles". In: 2008 18th International Conference on Electrical Machines. 2008, pp. 1–5. DOI: 10.1109/ICELMACH.2008.4800044.
- [16] Fred Flett. A Tutorial in AC Induction and Permanent Magnet Synchronous Motors: Vector Control with Digital Signal Processors. Analog Devices, 1994.
- [17] Nasser Hashemnia and Behzad Asaei. "Comparative study of using different electric motors in the electric vehicles". In: 2008 18th international conference on electrical machines. IEEE. 2008, pp. 1–5.
- [18] Dakshina M. Bellur and Marian K. Kazimierczuk. "DC-DC converters for electric vehicle applications". In: 2007 Electrical Insulation Conference and Electrical Manufacturing Expo. 2007, pp. 286–293. DOI: 10.1109/EEIC.2007.4562633.
- [19] Jie Deng et al. "Electric vehicles batteries: requirements and challenges". In: *Joule* 4.3 (2020), pp. 511–515.
- [20] Rejaul Islam, SM Sajjad Hossain Rafin, and Osama A Mohammed. "Comprehensive review of power electronic converters in electric vehicle applications". In: *Forecasting* 5.1 (2022), pp. 22–80.
- [21] M.A. Rahman and P. Zhou. "Analysis of brushless permanent magnet synchronous motors". In: *IEEE Transactions on Industrial Electronics* 43.2 (1996), pp. 256–267. DOI: 10.1109/41.491349.
- [22] Thomas M Jahns and Wen L Soong. "Pulsating torque minimization techniques for permanent magnet AC motor drives-a review". In: *IEEE transactions on industrial electronics* 43.2 (2002), pp. 321–330.
- [23] MS Merzoug, F Naceri, et al. "Comparison of field-oriented control and direct torque control for permanent magnet synchronous motor (PMSM)". In: World Academy of Science, Engineering and Technology 45 (2008), pp. 299–304.

- [24] Imperix. Field-Oriented Control of PMSM. Theory and implementation of Field-Oriented Control for Permanent Magnet Synchronous Motors. Accessed: 21-08-2025. URL: https://imperix.com/doc/ implementation/field-oriented-control-of-pmsm.
- [25] The MathWorks, Inc. *PMSM Permanent magnet synchronous motor with sinusoidal flux distribution*. Accessed: 25-09-2025. 2025. URL: https://it.mathworks.com/help/sps/ref/pmsm.html.
- [26] Capitolo 5: Motore Brushless Sinusoidale. Lecture Notes. Accessed: 21-08-2025. Department of Industrial Engineering, University of Padova. URL: https://elearning.unipd.it/dii/pluginfile.php/188933/mod_resource/content/4/Capitolo%205%20-%20Motore%20brushless%20sinusoidale%20-%2017%20maggio%202008.pdf.
- [27] Claudio Bianchini et al. "Effects of the magnetic model of interior permanent magnet machine on mtpa, flux weakening and mtpv evaluation". In: *Machines* 11.1 (2023), p. 77.
- [28] Vishal Jagota, Aman Preet Singh Sethi, and Khushmeet Kumar. "Finite element method: an overview". In: Walailak Journal of Science and Technology (WJST) 10.1 (2013), pp. 1–8.
- [29] Claudio Bianchini et al. "Inductance Based Lumped Parameter IPM Machine Model for Fast Simulation". In: 2024 IEEE Energy Conversion Congress and Exposition (ECCE). IEEE. 2024, pp. 5262–5268.
- [30] MathWorks, Inc. Rotational Damper viscous damper in mechanical rotational systems. Accessed: 06-11-2025. 2025.
- [31] The MathWorks, Inc. VehicleBody (Simulink) R2025b Documentation. Accessed: 30-10-2025. 2025. URL: https://www.mathworks.com/help/sdl/ref/simplegear.html#bsp71tc-1.
- [32] The MathWorks, Inc. VehicleBody (Simulink) R2025b Documentation. Accessed: 30-10-2025. 2025. URL: https://www.mathworks.com/help/releases/R2025b/sd1/ref/vehiclebody.html.